Øystein Dahl

Measurements and modelling of effect of interface on ferroelectricity in lead titanate thin films

Thesis for the degree of Philosophiae Doctor

Trondheim, February 2010

Norwegian University of Science and Technology
Faculty of Information Technology,
Mathematics and Electrical Engineering
Department of Electronics and Telecommunications

NTNU
Norwegian University of Science and Technology

Thesis for the degree of Philosophiae Doctor

Faculty of Information Technology,
Mathematics and Electrical Engineering
Department of Electronics and Telecommunications

ISBN 978-82-471-1989-1 (printed ver.)
ISBN 978-82-471-1990-7 (electronic ver.)
ISSN 1503-8181

Doctoral theses at NTNU, 2010:17

Printed by NTNU-trykk

Contents

1 Introduction **1**

2 Macroscopic description of ferroelectricity **9**
2.1 The thermodynamic foundation 9
2.1.1 The electrostatic energy 9
2.1.2 The elastic energy 10
2.1.3 The thermodynamic potentials 14
2.1.4 Equations of state 16
2.1.5 The dielectric function 18
2.2 Landau-Ginzburg-Devonshire theory 18
2.2.1 Bulk theory for second- and first-order transitions 19
2.2.2 The effect of strain 22
2.2.3 The pyroelectric effect 24

3 Experimental techniques **27**
3.1 Sputter deposition 27
3.2 X-ray diffraction 28
3.3 X-ray photoelectron spectroscopy 31
3.4 Atomic force microscopy 33
3.5 Polarization and capacitance measurements 34

4 Pyroelectric measurements **37**
4.1 Experimental setup 37
4.2 Induced temperature variation 37
4.3 Pyroelectric response 40

I Imaging of out-of-plane interfacial strain in epitaxial $PbTiO_3/SrTiO_3$ thin films **45**

II Crystalline and dielectric properties of sputter deposited $PbTiO_3$ thin films **51**

III Polarization direction and stability in ferroelectric lead titanate thin films **65**

5 Conclusions and outlook **75**

List of Figures

1.1 Hysteresis loop for a ferroelectric material 2
1.2 The ideal cubic perovskite structure 2
2.1 A dielectric volume with conductors 10
2.2 Deformation of a continuous body 11
2.3 The stress tensor 12
2.4 The free energy in a second order transition 20
2.5 The free energy in a first order transition 21
2.6 Hysteresis loop from LGD theory 21
3.1 Scattering of x-rays 28
3.2 Illustration of scattering in reciprocal space 30
3.3 Goniometer used for XRD measurements 30
3.4 Schematic of the XPS setup 32
3.5 Electron energy levels in a solid and the photoemission spectrum . . . 32
3.6 Illustration of an AFM tip 33
3.7 Pulses for polarization measurement 34
3.8 Equivalent circuit for thin dielectric films 35
4.1 The pyroelectric measurement setup 38
4.2 Illustration of capacitor structures 38
4.3 The thermal wavelength for Au and $SrTiO_3$ 39
4.4 The surface temperature of the capacitor structure 40

List of Tables

4.1 Thermal constants for the materials in the experimental study 39
4.2 Elastic constants for $PbTiO_3$ 41
4.3 Dielectric stiffness coefficients for $PbTiO_3$ 42
4.4 Thermal expansion coefficients for $PbTiO_3$ and $SrTiO_3$ 43

Acknowledgements and author's contribution

The manuscript was significantly improved through comments and corrections from my supervisors Prof. Thomas Tybell and Prof. Jostein Grepstad, which I also thank for support during the work and for giving me the oppurtunity to start this work. For the published results in Paper I, my contributions were synthesis,atomic force microscopy, and x-ray diffraction characterization of the films, and input to the analysis of the results. I thank Prof. R. Holmestad, Prof. A. T. J. van Helvoort, and B. G. Soleim, for their part in this publication. For Paper II and III, I was responsible for experimental work, model calculations and data analysis.

In addition, I have contributed to papers on growth and characterization of (Pb,La)(Zr,Ti)O_3 thin films,[1] study of domain structure in $PbTiO_3$ thin films,[2] and photochemical properties of $PbTiO_3$/$SrTiO_3$ structures.[3]

I also thank Prof. M. Lindgren, Dr J. Örtegren, Prof. T. Grande, E. Nilsen, Prof. F. Mo, L. Johnsen, and K. Midtbø for help with experiments, and Research Director Dr R. Spooren and Research Manager Dr R. Fagerberg at Sintef Materials and Chemistry for giving me the opportunity and time to finish this work.

Financial support from the Department of Electronics and Telecommunications at the Norwegian University of Science and Technology is gratefully acknowledged.

[1] A. K. Sarin Kumar, Ø. Dahl, S. V. Pettersen, J. K. Grepstad, and T. Tybell, *Characterization of crystalline $Pb_{0.92}La_{0.08}Zr_{0.4}Ti_{0.6}O_3$ thin films grown by off-axis radio frequency magnetron sputtering*, Thin Solid Films **492**, 71 (2005).

[2] R. Takahashi, Ø. Dahl, E. Eberg, J. K. Grepstad, and T. Tybell, *Ferroelectric stripe domains in $PbTiO_3$ thin films: Depolarization field and domain randomness*, J. Appl. Phys. **104**, 064109 (2008).

[3] R. Takahashi, M. Katayama, Ø. Dahl, J. K. Grepstad, Y. Matsumoto, and T. Tybell, *Epilayer control of photodeposited materials during UV photocatalysis*, Appl. Phys. Lett. **94**, 232901 (2009).

Chapter 1
Introduction

A certain class of materials exhibits the property of a spontaneous polarization;[1] these materials are called pyroelectrics. If the spontaneous polarization direction can be changed by the application of an electric field, the materials are called ferroelectric, in analogy with the ferromagnetic materials. Figure 1.1 illustrates the observed relationship between electric field $\mathbf{E}$ and electric displacement $\mathbf{D}$ in a ferroelectric material. Around zero electric field the displacement field is dependent on the past field history, and there is a hysteretic effect. Two important parameters are defined from the hysteresis loop: the coercive field, or half the width of the hysteresis curve at zero displacement field, and the remanent polarization, or the net displacement field at zero electric field. Typically, the materials have a high-temperature, high-symmetry state with zero spontaneous polarization,[2] and at a certain temperature there is a phase transition to a state with non-zero spontaneous polarization.

Pyroelectrics have been known for a long time, dating back to the ancient Greeks [2]. Ferroelectrics were comparatively recently discovered, it was not until 1920 that ferroelectricity was demonstrated in Rochelle salt by Valasek [3, 4]. According to Lines and Glass, the ferroelectric phenomena was for a time considered an accident of Nature [5, p. 2]. In most instances the polarization is screened or neutralized, either by charge near the surface, or by domains of opposite polarization, making a direct detection of the polarization difficult. When the screening is due to charge near the surface, a change in the spontaneous polarization by a temperature variation can be detected; this is the pyroelectric phenomenon.

After the discovery of ferroelectricity in $BaTiO_3$ [6, 7], progress was made in the understanding of ferroelectricity on a microscopic level. The relatively simple perovskite structure was more amenable to theoretical considerations than the complex structure of the hydrogen bonded salts hitherto known to exhibit ferroelectricity. The cubic perovskite structure is illustrated in Fig. 1.2. This structure is found in several oxides of general formula ABO_3. The A cation is shown as a large circle, and the B cation as a smaller black circle. The oxygen anions are positioned at the vertices of the octahedra. Some of the most studied ferroelectrics, $BaTiO_3$, $PbTiO_3$, and solid solutions of $PbTiO_3$ and $PbZrO_3$,[3] are found in distorted perovskite structures. They share the high-temperature cubic phase, and have transitions to ferroelectric

[1] That is, the displacement field is non-zero even in zero electric field, $\mathbf{D}(\mathbf{E} = 0) = \mathbf{P}_s$.

[2] This high-temperature, high-symmetry phase is not a prerequisite, and there are materials that decompose before this phase is reached [1, p. 355]. In chapter 2.2, the high-symmetry phase is assumed to exist.

[3] In the following, solid solutions of $PbTiO_3$ and $PbZrO_3$ are abbreviated as $Pb(Zr,Ti)O_3$, without specifying the composition.

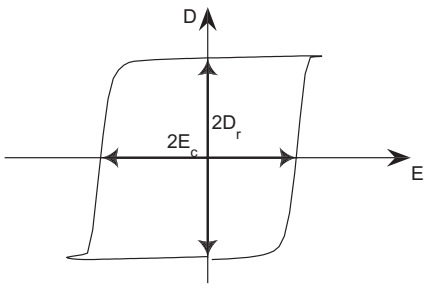

Figure 1.1: Hysteresis loop for a ferroelectric material. The coercive field and remanent polarization are indicated on the figure.

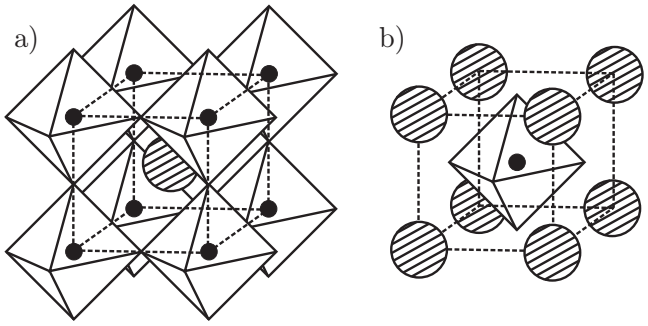

Figure 1.2: The ideal cubic perovskite structure found in oxides of general formula ABO_3. The A cation is shown as a large shaded circle and the B cation as a small black circle. The oxygen anions are located at the vertices of the octahedra. After Náray-Szabó [8] and von Hippel [9].

tetragonal structures. $BaTiO_3$ has further transitions with decreasing temperature, while the transition sequence for $Pb(Zr,Ti)O_3$ depends on the composition. This general introduction gives some references to the observed properties of ferroelectric materials, whereas only $PbTiO_3$ is considered in the experimental study.

As mentioned, the simple perovskite structure made a theoretical analysis more approachable. For instance, it was now possible to exactly calculate the electrostatic interaction between the atoms in the unit cell [10]. Cochran calculated the phonon dispersion relation for the perovskite structure, using a shell model, where the ions are approximated as cores, consisting of the nucleus and the inner electrons, and a shell of the valence electrons [11]. It was shown that the ferroelectric transition is associated with a transverse optical mode of low frequency. In the harmonic approximation for the inter-atomic potential, the crystal becomes unstable with respect to a transverse optical vibration mode when the electrostatic force becomes equal to the inter-atomic restoring force. Anharmonic terms in the inter-atomic potential creates a new equilibrium position for the atoms, and the material has a phase transition to the new structure.

Promising progress on the theoretical side has been made in numerical approximations based on density functional theory (DFT). The Berry phase approach has proved successful for calculating the bulk polarization [12–15]. Bulk polarization can not be defined in terms of the delocalized charge density [16], and the bulk polarization is instead found by considering the charge current, or the difference in geometric phase of the valence electron wave function, between a reference structure of zero polarization and the actual structure. Calculations within DFT have been used to study the properties of bulk ferroelectric materials [17–19], and surface and interface properties [20–26], relevant for thin films. Thin film geometries with various degrees of constraints and relaxations have been considered. In particular, the effect of electrodes [27–30], and asymmetries giving rise to interface dipoles [31–33], are topics of current interest.

Even if such microscopic theories are needed in order to understand and predict if a material displays ferroelectric behaviour, a pure phenomenological theory is often sufficient to describe the ferroelectric phenomenon. A thermodynamic description of ferroelectric phenomena in terms of Landau's theory of phase transitions was given by Ginzburg [34] and Devonshire [35–37]. In this theory, the free energy is expanded as a power series in the order parameter, usually the polarization, and the stable configuration is found by minimizing the free energy. The theory can successfully describe the phase transition, and the temperature dependence of the dielectric constant and related properties near the transition point. For thin films it is important to consider the depolarization field due to incomplete polarization screening, even with metallic electrodes [38], and the mechanical boundary conditions imposed on the thin film [39]. The Landau-Ginzburg-Devonshire theory is discussed further in Chapter 2.2, and in Paper III the Landau-Ginzburg-Devonshire theory, along with

electrostatics and semiconductor statistics, is used to calculate the polarization profile and stability in thin films with asymmetric boundary conditions.

The symmetric and stable polarization states in ferroelectrics, as described above, are potentially useful. However, it turns out that for physically realised devices, the states are often not symmetric nor stable. Hysteresis loops that are shifted along the electric field axis are well known [40]. The shift can be interpreted as a bias field, which can be related to effects external to the volume of the ferroelectric material, such as different electrode materials, or it can be due to effects internal to the volume of the ferroelectric material, such as impurities. An extensive body of literature exists on the subject, both for bulk and thin film samples. Experimentally it is found that the bias field depends on the oxygen pressure during processing, with an increasing bias field for decreasing oxygen pressure, suggesting that oxygen vacancies are involved [41–43]. Intentionally acceptor or donor doped materials have acted as model systems to study the influence of charged point defects on the bias field. $Pb(Zr,Ti)O_3$ doped with acceptor impurities have shown an increased bias field [44–46], while donor impurities decreased the bias field [46–49]. However, there are also reports of no influence of acceptor and donor impurities on the room temperature bias field [50]. It has been suggested that the bias field is caused by oriented defect dipole pairs [45, 51]. In this model, defect dipoles from positively charged oxygen vacancies and negatively charged acceptor impurities, align in the direction of the polarization. The slow re-orientation of the defect dipoles, compared to the fast switching of the polarization, gives an energy difference between the states with polarization parallel and anti-parallel with the defect dipoles. Increasing the acceptor density increases the formal bias field, while decreasing the density of oxygen vacancies, by equilibrating the material at high oxygen pressure, or adding donor impurities, decreases the formal bias field. Illumination with ultraviolet light has been found to either increase or decrease the bias field, interpreted as an effect of trapped charge carriers [52–55]. The trapped charge carriers could eliminate the formal bias field from the defect dipoles, or they can set up an additional bias field. The electric field in a space charge layer can also account for the bias field [56, 57]. The space charge layer can be the result of surface state charges, charge transfer from the electrodes, or a non-stoichiometric surface layer [58, 59]. The electrodes can also give an additional contribution to the bias field, apart from space charge layers, through a difference in the work function for the electrodes [60]. Indications of this effect on the ferroelectric properties have been found in several studies [61–63]. Large shifts of the hysteresis loops can result when one of the electrodes is semiconducting, due to the voltage drop over the depletion layer in the semiconductor when the screening is by minority charge. This has been observed with Si electrodes [64] and with Nb doped $SrTiO_3$ electrodes [65]. In practice all of these effects may occur. To be able to control the polarization properties, it is necessary to control both defects and interface properties.

Another non-ideality found in ferroelectrics is a decay of the remanent polarization with time. The time-dependence can be divided into a relatively rapid polarization decay for short times (up to a few seconds) followed by a slower decay [66–71]. Several factors have been shown to affect the decay, including the electrodes [68, 72], the electrode interface quality [73], the film thickness [71, 74], the temperature [75, 76], the polarization time [67], and the number of previous switching cycles [77]. The decay is presumably not caused by a decrease in the spontaneous polarization, but by a local reversal of the polarization, decreasing the macroscopic net polarization, as has been demonstrated in scanning probe measurements [78]. The decay is often attributed to the depolarization field existing in ferroelectric thin films [38, 66, 79]. This implies a continuously decreasing net polarization, gradually approaching zero, as the depolarization field is eliminated by domain formation. Other effects can contribute, such as the internal bias field mentioned above, and the final net polarization need not be zero. This raises the particular question of the stability of the switched net polarization in very thin ferroelectric films. The polarization decay is more pronounced in very thin films, due to the increased depolarization field and a stronger influence from asymmetries at the interfaces with the electrodes. These effects may lead to a total suppression of the spontaneous polarization, or a preference for one polarization direction. A non-zero final net polarization has been observed in fatigued $Pb(Zr,Ti)O_3$ thin films and ultra-thin polymer films, where only one polarization direction was found to be stable [80–83]. Contrary to this, the net polarization was found to decay with time in thin $BaTiO_3$ films, approaching a zero value [71]. The reasons for a stable or unstable polarization are at the moment unresolved. Paper III gives results of the polarization stability in $PbTiO_3$ thin films of different thickness.

Polar surfaces and interfaces are currently attracting much experimental and theoretical interest [84], and the interface quality can have a significant influence on ferroelectric properties. For fundamental reasons it is of interest to study the effect of size on ferroelectric properties, both on the ideal intrinsic properties, and on external effects such as asymmetries caused by interfaces and defects. From a practical point of view it also important to know how materials will behave in a certain configuration. For instance it is often observed that the thickness dependence of the capacitance of thin ferroelectric films deviates from the geometrically expected parallel plate behaviour. Whether this is an effect of the electrodes [85, 86], or an effect of the material properties changing with film size can vary in different material systems. A behaviour consistent with a description in terms of a series connection of the film capacitance and a constant interface/electrode capacitance, in the region of 0.1 to 0.7 F/m^2,[4]has been reported [87–90], however, more complicated thickness behaviour, related to structural changes in the material, are also observed [91, 92].

[4]We will often give quantities as per area, reflecting the one-dimensional nature of capacitor structures, where only the film thickness, and not the capacitor area, is of interest.

Paper II presents dielectric measurements of thin $PbTiO_3$ films, pseudomorphically grown on $SrTiO_3$ substrates, which allows for an evaluation of the film thickness influence on the dielectric properties without interference from varying mechanical conditions.

The size dependence of the ferroelectric properties has been studied in $PbTiO_3$ particles. The polarization in tetragonal perovskites can be related to the tetragonal distortion of the unit cell [93, 94], hence structural data are often used to monitor ferroelectric properties. A reduction of the tetragonality was observed for particle size less than about 60 nm [95–98], with a concomitant reduction of the transition temperature [99]. Of more relevance to this study is the behaviour in thin films. Both $BaTiO_3$ and $PbTiO_3$, epitaxially grown on $SrTiO_3$, have shown a decreasing tetragonality for film thickness below 10 to 20 nm [100, 101], however, there are also reports of thickness independent tetragonality for $PbTiO_3$ films in the 1 to 10 nm thickness range [102]. The tetragonal distortion is not necessarily uniform throughout the film thickness. A decreasing lattice constant in the direction of the polarization have been found near the interface with a $SrRuO_3$ electrode for $Pb(Zr,Ti)O_3$ thin films [103, 104]. Paper I is a study of the strain normal to the interface between $PbTiO_3$ and $SrTiO_3$. Paper II presents data of the out-of-plane lattice constant with film thickness, and Paper III relates these measurements to the polarization.

One important difference between particles and epitaxial thin films is the mechanical constraints. The strain conditions imposed on the thin film from epitaxial growth on a thick substrate have been used to engineer the ferroelectric properties such as transition temperature and polarization direction [105, 106]. This also implies a difference in pseudomorphically, and relaxed epitaxial thin films, an important consideration when comparing results in different material systems. For instance the larger misfit strain in $BaTiO_3$ and $Pb(Zr,Ti)O_3$ epitaxially grown on a $SrTiO_3$ substrate as compared to $PbTiO_3$ films on the same substrate, leads to relaxation for a smaller critical film thickness. The enhanced polarization in strained $BaTiO_3$ and $Pb(Zr,Ti)O_3$ films decreases with increasing film thickness as the strain is relaxed [91, 107–109].

For fully strained films, the polarization in $BaTiO_3$ has been found to be nearly constant at room temperature for film thickness down to 15 nm [108], and decrease for thinner films [100, 110]. The polarization in $Pb(Zr,Ti)O_3$ thin films shows a similar dependence [103, 109, 111–114]. Exact measurements of the polarization becomes challenging in thinner films due to an increase of the leakage current. Nonetheless, hysteretic polarization loops have been found in 5 nm thin $BaTiO_3$ films [100] and in 15 nm thin $Pb(Zr,Ti)O_3$ films [114], further corroborated with pulse switching experiments in 5 nm thin films [103, 114]. Scanning probe measurements have shown that the sign of the piezoelectric response can be switched, implying a switchable polarization, in perovskite films down to a thickness of a few nm [101, 115, 116].

X-ray diffraction measurements on thin $PbTiO_3$ films have shown the appearance of an in-plane superstructure, thought to stem from a periodic polarization domain pattern [117]. When the bottom electrode was metallic $SrRuO_3$, the $PbTiO_3$ thin film was found to be in a monodomain state [102]. This indicates that there is no total local suppression of the spontaneous polarization, though a large scale cancellation of the net polarization through domain formation can occur, depending on the interface nature.

Despite the continued interest in ferroelectric materials over the last half-century, there are still unresolved questions pertaining to the behaviour of physical realizations of ferroelectric devices. For instance, there is an incomplete understanding of the interaction between interfaces and the polarization. How to control the factors that determines the switchability, and subsequent stability, of the polarization? Can the interface properties be controlled to give predictive behaviour of the polarization? Are there ways to control the interaction between naturally occurring defects and the polarization?

This thesis addresses the measurement of ferroelectric properties in thin films with a pyroelectric method [118]. The pyroelectric method is a non-destructive way of measuring the initial polarization state, and to monitor the decay of the net polarization. Of particular interest is the interface between the ferroelectric and the substrate or electrodes, and its influence is studied by a combination of structural and dielectric characterization.

Chapter 2 gives an overview of the macroscopic thermodynamic treatment of ferroelectrics, in order to give the reader unfamiliar with the subject some background to interpret the data. Chapter 3 gives details of film growth and standard film analysis techniques. Chapter 4 describes the pyroelectric measurement technique. Results are given in the three papers. Paper one is an investigation of the interface between $PbTiO_3$ films and $SrTiO_3$ substrates. The second paper describes the thickness dependence of the dielectric constant and the effect of film growth temperature on dielectric properties and surface stoichiometry, while the third paper contains pyroelectric measurements and addresses the stability of the polarization with decreasing film thickness. The results are discussed in terms of a Landau-Ginzburg-Devonshire model of an asymmetrically electroded ferroelectric thin film. As a whole, these papers shows the importance of the interfaces on the ferroelectric properties in thin films.

Chapter 2
Macroscopic description of ferroelectricity

In this chapter the macroscopic theory for ferroelectrics needed to establish the relationship between the external parameters, i.e., the temperature, electric field and mechanical stress, and the response of the material is outlined. The purpose is to show, within the macroscopic quasi-linear elastic dielectric theory, the relation between electric field and displacement field that is needed to describe a semiconducting ferroelectric, as in Paper III. Furthermore, the pyroelectric coefficient and the relation between strain and polarization in an epitaxial thin film is shown.

2.1 The thermodynamic foundation

The various thermodynamic potentials shows the criteria for equilibrium under different experimental configurations. It is instructive to first consider the internal energy, and find the expressions for electrical and mechanical work for an elastic dielectric.

The first law of thermodynamics states that the change in internal energy, $d\mathfrak{U}$, is equal to the sum of the heat absorbed, dQ, and the work done on the same volume, dW [119, p. 11],

$$d\mathfrak{U} = dQ + dW, \tag{2.1}$$

i.e., the energy is conserved. The law of increasing entropy states that, for any transformation, the exchange of heat is related to the absolute temperature T and the entropy change dS as [119],

$$dQ \leq T dS,$$

where the equality sign holds for reversible transformations. In the following sections, the work done by electrical and mechanical forces is considered.

2.1.1 The electrostatic energy

Discussions of electrostatic energy in dielectric media are found in textbooks on electrostatics, see for instance Stratton [120, ch. 2].

Consider a volume with dielectric matter and charged conductors as in Fig. 2.1 where $S_1 \dots S_n$ are the surfaces of the conductors and S_0 some bounding surface. The conductors have a surface charge density σ and within the dielectric the charge is distributed with a density ρ. The work needed for a variation of the charge density

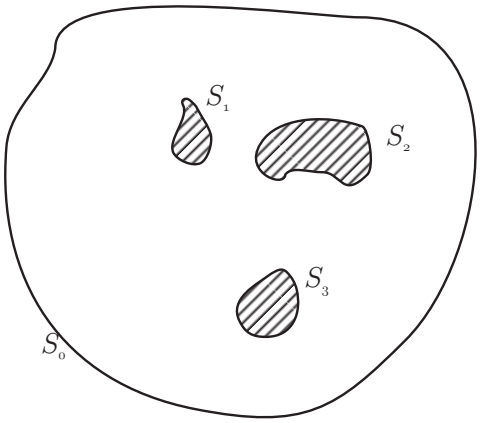

Figure 2.1: A dielectric volume with conductors. The conductors are shown as shaded structures bounded by the surfaces S_i, and the dielectric volume is bounded by the surface S_0. After Stratton [120].

$\delta\rho$ and $\delta\sigma$ is

$$\delta W_E = \int_V \phi\delta\rho dv + \sum_{k=1}^{n} \int_{S_k} \phi\delta\sigma da,$$

where ϕ is the electrostatic potential, V the volume of the dielectric, and the sum is over the surfaces of the conductors. It will be more convenient to express this in terms of the electric field $\mathbf{E}$ and the displacement field $\mathbf{D}$, which in a dielectric material with polarization $\mathbf{P}$ is $\mathbf{D} = \epsilon_0\mathbf{E} + \mathbf{P}$, where ϵ_0 is the vacuum permittivity. Using Maxwell's equation for the relationship between the charge density and the gradient of the displacement field, and the divergence theorem, the variation of the work is[1]

$$\delta W_E = \int_V E_i\delta D_i dv + \int_{S_0} \phi\delta D_i n_i da.$$

If the volume and outer bounding surface are increased to infinity, where $\phi = 0$,

$$\delta W_E = \int_{V'} E_i\delta D_i dv,$$

where the integral is to be taken over all space, excluding the conductors.

2.1.2 The elastic energy

The energy stored in a body by small deformations can be expressed by the strain and stress tensors. An introduction to the theory can be found in Nye [121, ch. V

[1]The Einstein notation with implicit sums over repeated indices is used, and $\mathbf{E} = E_i\hat{x}_i$, &c., where $\hat{x}_1$, $\hat{x}_2$, and $\hat{x}_3$ are unit vectors.

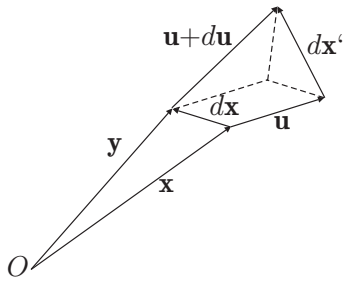

Figure 2.2: Deformation of a continuous body. A point at $\mathbf{x}$ is displaced an amount $\mathbf{u}$. The nearby point at $\mathbf{y}$ is displaced an amount $\mathbf{u} + d\mathbf{u}$. After Stratton [120] and Nye [121].

& VI], upon which most of this section is based.

The strain tensor

Figure 2.2 illustrates the deformation of a continuous body. To find an expression for the elastic deformation, consider the line element $d\mathbf{x}$ between the positions $\mathbf{x}$ and $\mathbf{y}$. After the deformation the point $\mathbf{x}$ is at $\mathbf{x}' = \mathbf{x} + \mathbf{u}$, where $\mathbf{u}$ is the displacement vector describing the deformation. The nearby point initially at $\mathbf{y} = \mathbf{x} + d\mathbf{x}$ is after the deformation at $\mathbf{y}' = \mathbf{y} + \mathbf{u} + d\mathbf{u}$. The components of the line element $d\mathbf{x}$ is after the deformation

$$dx_i' = dx_i + \frac{\partial u_i}{\partial x_j} dx_j.$$

The square of the length of the line element is

$$|dx_i'|^2 = \left| dx_i + \frac{\partial u_i}{\partial x_j} dx_j \right|^2 = dx_i^2 + 2\frac{\partial u_i}{\partial x_j} dx_j dx_i + \frac{\partial u_i}{\partial x_j}\frac{\partial u_i}{\partial x_k} dx_j dx_k,$$

which can be written in the symmetric form [122, p. 2]

$$dx_i'^2 = dx_i^2 + 2\left[\frac{1}{2}\left(\frac{\partial u_i}{\partial x_j} + \frac{\partial u_j}{\partial x_i} + \frac{\partial u_k}{\partial x_j}\frac{\partial u_k}{\partial x_i}\right)\right] dx_j dx_i.$$

For infinitesimal displacements the last term in the brackets can be neglected [122, p. 3], and

$$dx_i'^2 = dx_i^2 + 2u_{ij} dx_i dx_j$$

where u_{ij} is the strain tensor defined as the symmetric tensor

$$u_{ij} = \frac{1}{2}\left(\frac{\partial u_i}{\partial x_j} + \frac{\partial u_j}{\partial x_i}\right).$$

This symmetric strain tensor is of considerable use in the linear elastic theory.

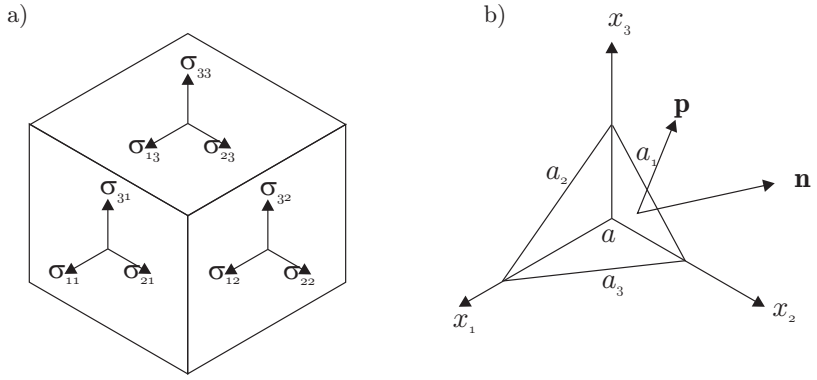

Figure 2.3: The stress tensor. a) Illustration of the stress components σ_{ij}. b) Illustration of the relation between the force per area p_i acting on a surface element and the stress. After Nye [121].

The stress tensor

For homogenous stress the components of stress can be defined with reference to Fig. 2.3 a). The stress component σ_{ij} is the force per surface area acting in the x_i direction on the face perpendicular to the x_j direction. More generally, the force acting on a surface element can be found by considering a small tetrahedron as in Fig. 2.3 b). The faces perpendicular to the axes x_i have areas a_i, while the fourth face has an area a. This face is considered as the tangential plane at the surface point. The surface normal vector has components $n_i = a_i/a$. The force per area acting on this face is $\mathbf{p}$. For a body at rest, the forces in each direction cancel, so that

$$p_i a = \sigma_{ij} a_j,$$

or, since $n_j = a_j/a$,

$$p_i = \sigma_{ij} n_j.$$

In the absence of body-torques, the stress tensor can be shown to be symmetric,

$$\sigma_{ij} = \sigma_{ji},$$

see for instance Nye [121, p. 86]. This symmetry is used when finding the elastic energy.[2]

[2]In the presence of body-torques, one can use the symmetric part of the stress tensor $\sigma_{ij} = 1/2(\sigma_{ij} + \sigma_{ji})$ [121, p. 87].

Elastic materials and the Voigt notation

For small stresses the strain is linearly dependent on the stress components [121, p. 131]. This is expressed by Hooke's law

$$u_{ij} = s_{ijkl}\sigma_{kl}.$$

The 81 components of the elastic compliance tensor s_{ijkl} are not all independent. Since the stress and strain tensors are symmetrical, it follows that $s_{ijkl} = s_{jikl}$ and $s_{ijkl} = s_{ijlk}$. Thus the elastic compliance tensor has only 36 independent components [121, p. 133].

In the reduced Voigt notation, the stress and strain components are written with one suffix [121, p. 134]

$$\begin{bmatrix} \sigma_{11} & \sigma_{12} & \sigma_{13} \\ \sigma_{21} & \sigma_{22} & \sigma_{23} \\ \sigma_{31} & \sigma_{32} & \sigma_{33} \end{bmatrix} \rightarrow \begin{bmatrix} \sigma_1 & \sigma_6 & \sigma_5 \\ \sigma_6 & \sigma_2 & \sigma_4 \\ \sigma_5 & \sigma_4 & \sigma_3 \end{bmatrix}$$

and

$$\begin{bmatrix} u_{11} & u_{12} & u_{13} \\ u_{21} & u_{22} & u_{23} \\ u_{31} & u_{32} & u_{33} \end{bmatrix} \rightarrow \begin{bmatrix} u_1 & \frac{1}{2}u_6 & \frac{1}{2}u_5 \\ \frac{1}{2}u_6 & u_2 & \frac{1}{2}u_4 \\ \frac{1}{2}u_5 & \frac{1}{2}u_4 & u_3 \end{bmatrix}.$$

The notation for the elastic compliance tensor is similarly simplified by expressing the first and second pair of suffixes of s_{ijkl}

$$\begin{array}{cccccccc} \{ij,kl\} & 11 & 22 & 33 & 23,32 & 31,13 & 12,21 \\ \{\alpha,\beta\} & 1 & 2 & 3 & 4 & 5 & 6 \end{array},$$

and inserting factors of 2 and 4 according to

$$\begin{array}{rl} s_{ijkl} = s_{\alpha\beta} & \text{when both } \alpha \text{ and } \beta \text{ are 1, 2, or 3} \\ 2s_{ijkl} = s_{\alpha\beta} & \text{when one of } \alpha \text{ and } \beta \text{ is 4, 5, or 6} \\ 4s_{ijkl} = s_{\alpha\beta} & \text{when both } \alpha \text{ and } \beta \text{ are 4, 5, or 6.} \end{array}$$

In this reduced notation, Hooke's law is

$$u_\alpha = s_{\alpha\beta}\sigma_\beta.$$

Greek suffixes indicates that the indices run over six terms, and latin suffixes indicates three terms.

The energy

Since the mechanical forces are of short range, the work done on a body element can be represented by a surface integral [122, p. 4]. For an infinitesimal displacement δu_i, the work is equal to the force times the displacement

$$\delta W_M = \int_S p_i \delta u_i da.$$

With $p_i = \sigma_{ij} n_j$ this is converted to a volume integral by the divergence theorem

$$\int_S \delta u_i \sigma_{ij} n_j da = \int_V \frac{\partial}{\partial x_j} (\delta u_i \sigma_{ij}) dv$$

so that

$$\delta W_M = \int_V \frac{\partial}{\partial x_j} \left(\sigma_{ij} \delta u_i \right) dv = \int_V \frac{\partial \sigma_{ij}}{\partial x_j} \delta u_i dv + \int_V \sigma_{ij} \frac{\partial \delta u_i}{\partial x_j} dv,$$

where V is the volume enclosed by the surface S. Since the stress tensor is symmetric, $\sigma_{ij} = \sigma_{ji}$, the last integral can be written

$$\int_V \sigma_{ij} \frac{1}{2} \left(\frac{\partial \delta u_i}{\partial x_j} + \frac{\partial \delta u_j}{\partial x_i} \right) dv.$$

Furthermore, if the stress is homogenous the first integral is zero, and, in the reduced Voigt notation,

$$\delta W_M = \int_V \sigma_\alpha \delta u_\alpha dv.$$

The integral is to be taken over the volume of the material.

2.1.3 The thermodynamic potentials

It has been found that the work performed by mechanical and electrical work is

$$\delta W = \delta W_M + \delta W_E = \int_V \sigma_\alpha \delta u_\alpha dv + \int_{V'} E_i \delta D_i dv,$$

where V is the volume of the dielectric, and V' is the entire space. From the first law of thermodynamics (2.1), the variation of the internal energy is

$$\delta \mathfrak{U} = dQ + \int_V \sigma_\alpha \delta u_\alpha dv + \int_{V'} E_i \delta D_i dv,$$

which for reversible processes with $dQ = TdS$ is

$$\delta \mathfrak{U} = TdS + \int_V \sigma_\alpha \delta u_\alpha dv + \int_{V'} E_i \delta D_i dv.$$

It is more convenient to consider thermodynamic potentials where the temperature T is an independent variable, since this is experimentally accessible and possible to control.

The free energy

If the ferroelectric crystal is in thermal contact with the surroundings, but constrained in a way as to not allow any work to be done, the free energy

$$\mathfrak{F} = \mathfrak{U} - TS$$

determines the stability of the system [123, ch. II]. The variation of the free energy is

$$\delta\mathfrak{F} = \delta\mathfrak{U} - SdT - TdS = dQ + \int_V \sigma_\alpha \delta u_\alpha dv + \int_{V'} E_i \delta D_i dv - SdT - TdS.$$

For reversible processes $dQ = TdS$ and

$$\delta\mathfrak{F} = -SdT + \int_V \sigma_\alpha \delta u_\alpha dv + \int_{V'} E_i \delta D_i dv,$$

so that for an isothermal, reversible process, the work done on the system is equal to the change in free energy. On the other hand, when the system is constrained in a way such that no work is done ($\delta\mathbf{u} = 0$, $\delta\mathbf{D} = 0$) $\delta\mathfrak{U} = dQ$, and at constant temperature

$$\delta\mathfrak{F} = dQ - TdS \leq 0,$$

so that any spontaneous process will decrease the free energy. If the system is in a state corresponding to a minimum of the free energy, then no further reduction can occur, and the system is in a stable equilibrium.

The thermodynamic potential at constant stress

If the crystal is allowed to expand or contract freely, so that the stress not the strain is constant, the elastic Gibbs free energy,

$$\mathfrak{G}_1 = \mathfrak{U} - TS - \int_V \sigma_\alpha u_\alpha dv,$$

is the appropriate thermodynamic potential. The variation of this thermodynamic potential is

$$\delta\mathfrak{G}_1 = dQ + \int_{V'} E_i \delta D_i dv - SdT - TdS - \int_V u_\alpha \delta\sigma_\alpha dv.$$

For reversible processes $dQ = TdS$ and

$$\delta\mathfrak{G}_1 = -SdT - \int_V u_\alpha \delta\sigma_\alpha dv + \int_{V'} E_i \delta D_i dv. \tag{2.2}$$

While if T, σ and $\mathbf{D}$ are held constant, as by the constraints of the system, any irreversible processes for which $dQ \leq TdS$ gives

$$\delta\mathfrak{G}_1 = dQ - TdS \leq 0,$$

so that the state which minimizes the elastic Gibbs free energy is thermodynamically stable.

The Gibbs free energy

If the electric field and the mechanical stress are controlled in the experiment, then the Gibbs free energy

$$\mathfrak{G} = \mathfrak{U} - TS - \int_{V'} E_i D_i dv - \int_V u_\alpha \sigma_\alpha dv$$

can be used to find the thermodynamically stable configuration. The variation is

$$\delta\mathfrak{G} = dQ - \int_{V'} D_i \delta E_i dv - \int_V u_\alpha \delta\sigma_\alpha dv - SdT - TdS,$$

which for reversible processes reduces to

$$\delta\mathfrak{G} = -SdT - \int_{V'} D_i \delta E_i dv - \int_V u_\alpha \delta\sigma_\alpha dv.$$

Here the electric field and the mechanical stress are the independent variables.

2.1.4 Equations of state

The equation of state can be found from the thermodynamic potentials. Choosing for instance the temperature T, stress σ and displacement field $\mathbf{D}$ as independent variables, the strain $\mathbf{u}$ and electric field $\mathbf{E}$ can be found from the functional derivative of the elastic Gibbs free energy.

As for ordinary functions of a finite number of variables, $f(a_1, a_2, \ldots, a_n)$, where the differential change is

$$df = \frac{\partial f}{\partial a_i} da_i,$$

the variation of the elastic Gibbs free energy can be written [124, p. 22]

$$\begin{aligned} \delta\mathfrak{G}_1 &= -SdT - \int_V \left(\frac{\delta\mathfrak{G}_1}{\delta\sigma_\alpha}\right)[\sigma_\alpha(\mathbf{x}'); \mathbf{x}]\, \delta\sigma_\alpha(\mathbf{x}) dv \\ &\quad + \int_{V'} \left(\frac{\delta\mathfrak{G}_1}{\delta D_i}\right)[D_i(\mathbf{x}'); \mathbf{x}]\, \delta D_i(\mathbf{x}) dv. \end{aligned}$$

where $(\delta\mathfrak{G}_1/\delta\sigma_\alpha)\,[\sigma_\alpha(\mathbf{x}'); \mathbf{x}]$ is the functional derivative of the energy functional with respect to σ_α at the point $\mathbf{x}$ with the temperature and displacement field held constant, and $(\delta\mathfrak{G}_1/\delta D_i)$ is similarly defined. The electric field under constant temperature and stress is seen by comparison with (2.2) to be

$$E_i\,[D_i(\mathbf{x}'); \mathbf{x}] = \left(\frac{\delta\mathfrak{G}_1}{\delta D_i}\right)[D_i(\mathbf{x}'); \mathbf{x}]\,, \tag{2.3}$$

and a similar expression is found for the strain under constant temperature and displacement field. The other thermodynamic potentials gives similar relations between the dependent variables and the functional derivatives of the thermodynamic potential.

The variational derivative

In the following chapters, the thermodynamic potentials will be expanded in the form of a power series in the components of the displacement field D_i and the gradients $D_{i,j} = \partial D_i / \partial x_j$,

$$\mathfrak{G}_1 = \int_{V'} G_1(D_i, D_{i,j}) dv,$$

where G_1 is the elastic Gibbs free energy density. In this approximation, the functional derivative takes a particularly simple form. Infinitesimal variations in the energy functional is [124, p. 30]

$$\delta\mathfrak{G}_1 = \int_{V'} \left(\frac{\partial G_1}{\partial D_i} \delta D_i + \frac{\partial G_1}{\partial D_{i,j}} \delta D_{i,j} \right) dv.$$

If the integration region is kept constant under the variation, $\delta D_{i,j} = \frac{\partial \delta D_i}{\partial x_j}$ [125], so that

$$\delta\mathfrak{G}_1 = \int_{V'} \left(\frac{\partial G_1}{\partial D_i} \delta D_i + \frac{\partial G_1}{\partial D_{i,j}} \frac{\partial \delta D_i}{\partial x_j} \right) dv.$$

The second term in the integral is

$$\int_{V'} \frac{\partial G_1}{\partial D_{i,j}} \frac{\partial \delta D_i}{\partial x_j} dv = \int_{V'} \left[\frac{\partial}{\partial x_j} \left(\frac{\partial G_1}{\partial D_{i,j}} \delta D_i \right) - \frac{\partial}{\partial x_j} \left(\frac{\partial G_1}{\partial D_{i,j}} \right) \delta D_i \right] dv.$$

By the divergence theorem this is

$$\int_{S'} \frac{\partial G_1}{\partial D_{i,j}} \delta D_i n_i da - \int_{V'} \frac{\partial}{\partial x_j} \left(\frac{\partial G_1}{\partial D_{i,j}} \right) \delta D_i dv,$$

where S' is the bounding surface of V'. Now if the boundary conditions implies $\delta D_i = 0$ at the bounding surface, the first integral is zero. Then

$$\delta\mathfrak{G}_1 = \int_{V'} \left(\frac{\partial G_1}{\partial D_i} - \frac{\partial}{\partial x_j} \frac{\partial G_1}{\partial D_{i,j}} \right) \delta D_i dv,$$

and the functional derivative is

$$\left(\frac{\delta \mathfrak{G}_1}{\delta D_i} \right) = \frac{\partial G_1}{\partial D_i} - \frac{\partial}{\partial x_j} \left(\frac{\partial G_1}{\partial D_{i,j}} \right),$$

an ordinary function of D_i and $D_{i,j}$.

2.1.5 The dielectric function

For linear dielectrics the polarization and electric field are related by the susceptibility tensor χ_{ij} as $P_i = \epsilon_0 \chi_{ij} E_j$, and the displacement field and electric field are related by the permittivity tensor ϵ_{ij} as $D_i = \epsilon_{ij} E_j$. Corresponding relations holds for non-linear dielectrics for small variations of the field

$$dD_i = \epsilon_{ij} dE_j.$$

The generalized permittivity is then defined as $\epsilon_{ij} = \frac{\partial D_i}{\partial E_j}$, and the inverse permittivity tensor as

$$\kappa_{ij} = \frac{\partial E_i}{\partial D_j},$$

see for instance Ref. [121, ch. X]. From the equation of state (2.3), the inverse permittivity tensor under constant stress is

$$\kappa_{ij} = \frac{\partial}{\partial D_j} \frac{\delta \mathfrak{G}_1}{\delta D_i}.$$

Similarly, the inverse permittivity tensor under constant strain can be found from the corresponding thermodynamic potential. The inverse permittivity tensor is just one of the compliance tensors for the material. In general these compliances depends on the constraints under which they are observed.[3]

2.2 Landau-Ginzburg-Devonshire theory

A phenomenological description of ferroelectrics can be based on the general Landau theory for phase transitions between states of different symmetry [123, ch. XIV]. An order parameter η is defined which takes the value zero in the symmetric phase and a non zero value in the less symmetric phase. The thermodynamic potential is expanded as a power series in the order parameter

$$\Phi = \Phi_0 + \alpha\eta + A\eta^2 + \beta\eta^3 + B\eta^4 + \dots.$$

For ferroelectrics the order parameter is usually taken as the polarization [34, 35], the displacement field [126, 127], or the displacement of the ions from their high symmetry positions [123]. The description is referred to as Landau-Ginzburg-Devonshire theory [34–37]. Here, the displacement field $\mathbf{D}$ is used as the order parameter due to it's natural involvement in the energy functionals and the boundary conditions for parallel plate capacitors.

[3] Frequently this is accentuated by using superscripts on the compliance tensor, indicating which variable is held constant. We will to a large extent suppress this, and only note when necessary the constraints.

2.2.1 Bulk theory for second- and first-order transitions

For a concise discussion, consider a material which at high temperature exist in a high symmetry paraelectric state. As the temperature is lowered, a spontaneous polarization develops at a critical temperature T_c. This is the situation for $PbTiO_3$. If it is assumed that the same expansion of the thermodynamic potential is valid for both states, and the symmetric state is cubic with a center of symmetry, it follows that the coefficients for the odd terms in the expansion is zero [126, p. 85]. Under zero stress conditions, the elastic Gibbs free energy density can be expanded as [35]:

$$G_1 = \frac{A}{2}D^2 + \frac{B}{4}D^4 + \frac{C}{6}D^6, \tag{2.4}$$

where the expansion is arbitrarily ended at the sixth order, and for simplicity, the polarization is assumed to develop only along one direction (so the suffix on the variables is dropped). For $D = 0$ to represent a minimum of the free energy in the symmetric state, A must be positive in this state. If there is a continuous change in the displacement field, from zero in the non-polar state to a non-zero D in the polar state, the transition is said to be of second order. For a continuous change, it follows that A must be negative in the polar state, and at the transition point $A(T_c) = 0$. Near the transition A can be expanded as $A(T) = \alpha(T - T_c)$, where α is a positive constant. This is in accordance with the observed Curie-Weiss behaviour of the inverse permittivity, $\kappa = \alpha(T - T_c)$ above the transition temperature, where α is the inverse Curie constant [128]. Furthermore, if $D = 0$ is to be a stable equilibrium value at the transition point, B must be positive (or zero). Assuming a non-zero value for B the higher order terms can be neglected, and the electric field is found from (2.4) and (2.3) as

$$E = \frac{\partial G_1}{\partial D} = AD + BD^3.$$

The spontaneous displacement field for temperatures below the transition point under zero electric field is thus

$$D_s^2(T) = \frac{\alpha(T_c - T)}{B}.$$

Figure 2.4 illustrates the free energy as a function of the displacement field for temperatures just above, at, and just below the transition temperature for a second order transition.

If there is a discontinuous jump in D from zero in the non-polar state to a finite value D_s at the transition temperature, the transition is said to be of first order. This can happen if B is negative, and then for stability C must be positive. The finite equilibrium value under zero electric field corresponds to

$$A + BD_s^2 + CD_s^4 = 0.$$

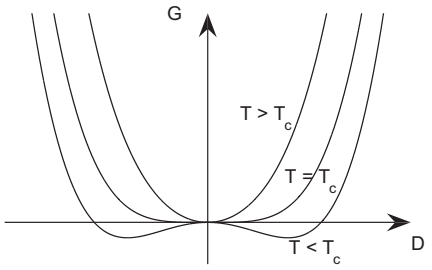

Figure 2.4: The free energy in a second order transition. The transition temperature is T_c, and the three curves shows the free energy just above, at, and just below the transition temperature.

At the transition point the free energy of the two states is equal, so that

$$\frac{A}{2}D_s^2 + \frac{B}{4}D_s^4 + \frac{C}{6}D_s^6 = 0.$$

Combining these two equations gives

$$D_s^2(T_c) = -\tfrac{3}{4}\tfrac{B}{C}, \text{ and } \quad A(T_c) = \tfrac{3}{16}\tfrac{B^2}{C},$$

which shows that A is positive at the transition temperature. The temperature dependence of A is assumed to follow a Curie-Weiss behaviour as for a continuous transition,

$$A(T) = \alpha(T - T_0),$$

with $T_0 < T_c$. The spontaneous displacement field under zero electric field is

$$D_s^2(T) = \frac{2}{3}D_s^2(T_c)\left(1 + \sqrt{1 - \frac{3}{4}\frac{T - T_0}{T_c - T_0}}\right)$$

Figure 2.5 illustrates the free energy as a function of the displacement field at temperatures just above, at, and just below the transition temperature.

The underlying equation of state, as found from (2.4) and (2.3) is illustrated in Fig. 2.6. A **D**-**E** hysteresis loop is measured by contacting the material with metal electrodes, and varying the electrostatic potential difference between those electrodes. Hence it is the electric field that is controlled in the experiment, and the thermodynamic stable state is determined by the minimum property of the Gibbs free energy. It can be shown that only the solid part of the curve in fig. 2.6

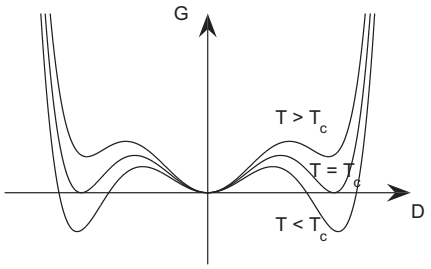

Figure 2.5: The free energy in a first order transition. The transition temperature is T_c, and the three curves shows the free energy just above, at, and just below the transition temperature.

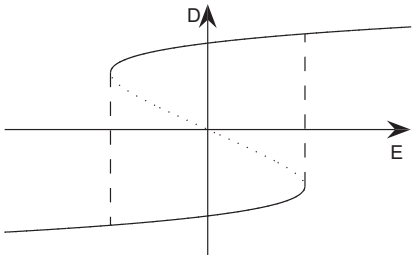

Figure 2.6: Schematic hysteresis loop from the equation of state. The solid curve represents the stable states. At the dashed lines, one of the states becomes unstable, and there would be a switching of the polarization direction.

represents a minimum of the Gibbs free energy, and that the broken part of the curve around zero electric field represents unstable states.[4] Furthermore, at zero electric field both $\pm D_s$ are absolutely stable, whereas at a finite electric field, one polarization direction represents a global minimum and is absolutely stable and the other polarization direction a local minimum that is only metastable. At the dashed lines, the metastable state becomes unstable, and the corresponding electric field is the thermodynamic coercive field.

2.2.2 The effect of strain

The effect of the elastic energy have so far been neglected (the stress was assumed to be zero). For a thin film grown epitaxially on a thick substrate this is not justifiable. The appropriate mechanical boundary conditions for a film epitaxially grown on a much thicker substrate are: [39] at the free surface the stress components $\sigma_3 = \sigma_4 = \sigma_5 = 0$, whereas at the interface with the substrate the strain components u_1, u_2, and u_6 are determined by the substrate.[5] The thermodynamic potential for the variables D_i, and u_1, u_2, u_6, σ_3, σ_4, σ_5, can be obtained from the elastic Gibbs free energy density by the transformation [39]

$$\tilde{G}_1 = G_1 + u_1\sigma_1 + u_2\sigma_2 + u_6\sigma_6, \tag{2.5}$$

where the elastic Gibbs free energy density for a cubic ferroelectric is [35, 129, 130]

$$\begin{aligned}
G_1 = {} & \alpha_1(D_1^2 + D_2^2 + D_3^2) + \alpha_{11}(D_1^4 + D_2^4 + D_3^4) \\
& + \alpha_{12}(D_1^2D_2^2 + D_2^2D_3^2 + D_3^2D_1^2) + \alpha_{111}(D_1^6 + D_2^6 + D_3^6) \\
& + \alpha_{112}[D_1^4(D_2^2 + D_3^2) + D_2^4(D_3^2 + D_1^2) + D_3^4(D_1^2 + D_2^2)] + \alpha_{123}D_1^2D_2^2D_3^2 \\
& - \frac{1}{2}s_{11}(\sigma_1^2 + \sigma_2^2 + \sigma_3^2) - s_{12}(\sigma_1\sigma_2 + \sigma_2\sigma_3 + \sigma_3\sigma_1) - \frac{1}{2}s_{44}(\sigma_4^2 + \sigma_5^2 + \sigma_6^2) \\
& - Q_{11}(\sigma_1D_1^2 + \sigma_2D_2^2 + \sigma_3D_3^2) \\
& - Q_{12}[\sigma_1(D_2^2 + D_3^2) + \sigma_2(D_3^2 + D_1^2) + \sigma_3(D_2^2 + D_1^2)] \\
& - Q_{44}(\sigma_4D_2D_3 + \sigma_5D_1D_3 + \sigma_6D_1D_2) \\
& + \frac{1}{2}g_{11}\left(D_{1,1}^2 + D_{2,2}^2 + D_{3,3}^2\right) + g_{12}\left(D_{1,1}D_{2,2} + D_{1,1}D_{3,3} + D_{2,2}D_{3,3}\right) \\
& + \frac{1}{2}g_{44}\left[\left(D_{1,2} + D_{2,1}\right)^2 + \left(D_{1,3} + D_{3,1}\right)^2 + \left(D_{2,3} + D_{3,2}\right)^2\right].
\end{aligned} \tag{2.6}$$

The α_i's are the components of the linear dielectric stiffness tensor, α_{ij}, and α_{ijk} components of the higher order dielectric stiffness tensors, $s_{\alpha\beta}$ the elastic compliance

[4] For a first order transition, near the transition temperature, the state with $\mathbf{E} = 0$ and $\mathbf{D} = 0$ is also a stable equilibrium.

[5] The directions are chosen so that x_1, x_2 are in the plane of the substrate, and x_3 is normal to the substrate.

coefficients, and $Q_{\alpha\beta}$ the electrostrictive constants. The modified thermodynamic potential has the property of being in a minimum for thermal equilibrium.

For the equations of state, it is still possible to use the elastic Gibbs free energy, or another thermodynamic potential. Finding the strain from (2.6) and solving for the stress gives

$$\begin{aligned}
\sigma_1 &= \frac{s_{11}}{s_{11}^2 - s_{12}^2}\left[u_1 - Q_{11}D_1^2 - Q_{12}(D_2^2 + D_3^2) - s_{12}\sigma_3\right] \\
&\quad - \frac{s_{12}}{s_{11}^2 - s_{12}^2}\left[u_2 - Q_{11}D_2^2 - Q_{12}(D_1^2 + D_3^2) - s_{12}\sigma_3\right], \\
\sigma_2 &= \frac{s_{11}}{s_{11}^2 - s_{12}^2}\left[u_2 - Q_{11}D_2^2 - Q_{12}(D_1^2 + D_3^2) - s_{12}\sigma_3\right] \\
&\quad - \frac{s_{12}}{s_{11}^2 - s_{12}^2}\left[u_1 - Q_{11}D_1^2 - Q_{12}(D_2^2 + D_3^2) - s_{12}\sigma_3\right], \\
\sigma_6 &= \frac{1}{s_{44}}\left(u_6 - Q_{44}D_1D_2\right).
\end{aligned}$$

Under the assumption of a tetragonal state with $D_1 = D_2 = 0$, (2.3) and (2.6), together with the stress conditions, gives

$$\begin{aligned}
E_3 &= 2\alpha_1 D_3 + 4\alpha_{11}D_3^3 + 6\alpha_{111}D_3^5 \\
&\quad - 2Q_{11}\sigma_3 D_3 - 2Q_{12}\frac{1}{s_{11} + s_{12}}\left(u_1 + u_2 - 2Q_{12}D_3^2 - 2s_{12}\sigma_3\right)D_3 \\
&\quad - g_{11}D_{3,3,3} - g_{44}(D_{3,1,1} + D_{3,2,2}).
\end{aligned}$$

In addition to the dielectric coupling terms found in the zero stress configuration, there is electrostrictive coupling of the displacement field to the in-plane strain. For a thin film with a free surface

$$\sigma_3 = 0,$$

and the mechanical boundary conditions for epitaxial growth on a cubic substrate gives

$$u_1 = u_2 = \tfrac{a_s - a_0}{a_0} = u_0, \text{ and } \quad u_6 = 0,$$

where a_s is the lattice constant of the substrate,[6] and a_0 is the extrapolated lattice constant of the reference state. Thus

$$\begin{aligned}
E_3 &= 2\alpha_1 D_3 + 4\alpha_{11}D_3^3 + 6\alpha_{111}D_3^5 \\
&\quad - 4Q_{12}\frac{1}{s_{11} + s_{12}}\left(u_0 - Q_{12}D_3^2\right)D_3 \\
&\quad - g_{11}D_{3,3,3},
\end{aligned}$$

[6]In cases where the thin film relaxes through misfit dislocations, an effective substrate lattice constant can be used [131].

where it is further assumed that the state is monodomain with $D_{3,1} = D_{3,2} = 0$. This can be written as

$$E_3 = AD_3 + BD_3^3 + CD_3^5 - g_{11}D_{3,3,3}, \tag{2.7}$$

where

$$\tfrac{A}{2} = \alpha_1 - 2\tfrac{u_0 Q_{12}}{s_{11}+s_{12}}, \quad \tfrac{B}{4} = \alpha_{11} + \tfrac{Q_{12}^2}{s_{11}+s_{12}}, \quad \tfrac{C}{6} = \alpha_{111}.$$

This is the relation used when calculating the displacement field profile in a thin ferroelectric film in Paper III. The effect of strain has not been independently checked in this work. All experiments were conducted with one type of substrate, so that identical strain conditions were imposed on all samples. However, the transition temperature, as inferred from x-ray diffraction measurements of the temperature dependence of the out-of-plane lattice constant (unpublished results), did show an increased transition temperature, as predicted from the modified thermodynamic potential [39], and also observed by others [117].

Relationship between strain and polarization

From the elastic Gibbs free energy with $D_1 = D_2 = 0$, $D_3 \neq 0$, and $\sigma_3 = 0$

$$u_3 = -\frac{\partial G_1}{\partial \sigma_3} = s_{12}(\sigma_1 + \sigma_2) + Q_{11}D_3^2.$$

With

$$\sigma_1 + \sigma_2 = 2\frac{u_0 - Q_{12}D_3^2}{s_{11} + s_{12}},$$

the strain is

$$u_3 = \frac{2s_{12}}{s_{11} + s_{12}}u_0 + \left(Q_{11} - \frac{2s_{12}}{s_{11} + s_{12}}Q_{12}\right) D_3^2. \tag{2.8}$$

This relation is used for calculating the displacement field based on measurements of the lattice constant in Paper III.

2.2.3 The pyroelectric effect

The temperature dependent polarization can give rise to an external current when the ferroelectric material is subject to a temperature variation. If the ferroelectric is connected to a low-impedance external electric circuit, the time variation of the temperature gives rise to the pyroelectric current density

$$\mathbf{j} = \frac{d\mathbf{D}}{dt} = \frac{d\mathbf{D}}{dT}\frac{dT}{dt}.$$

It is therefore of interest to calculate the temperature dependence of the polarization. In the following, it is assumed that the ferroelectric is in a monodomain tetragonal state.

Bulk theory

For bulk ferroelectrics in zero electric field and zero stress, the pyroelectric response has been found from the expansion of the free energy density. Assuming temperature independent coefficients for terms of higher order than quadratic in the free energy density, the pyroelectric coefficient was found as [132]

$$p = \frac{dD_3}{dT} = -\frac{\alpha}{\kappa_{33}} D_3,$$

where α is the inverse Curie constant and κ_{33} the inverse permittivity. In the next sections, the situation for a thin epitaxial film is considered.

The effect of strain

The strain in an epitaxial thin film changes the expansion coefficients of the first and third order terms in the equation of state as in (2.7)

$$\tfrac{A}{2} = \alpha_1 - 2\tfrac{u_0 Q_{12}}{s_{11}+s_{12}}, \quad \tfrac{B}{4} = \alpha_{11} + \tfrac{Q_{12}^2}{s_{11}+s_{12}},$$

where $\alpha_1 = \alpha(T - T_0)$. Assuming the electrostrictive constant Q_{12} and the stiffness coefficients s_{11} and s_{12} to be temperature independent [129, 133–135], there is no additional temperature dependence in the terms of higher than first order in the equation of state.

Under short-circuit conditions for a bulk ferroelectric

$$dE_3 = \frac{\partial E_3}{\partial T} dT + \frac{\partial E_3}{\partial D_3} dD_3 = 0$$

so that

$$\frac{dD_3}{dT} = -\frac{\frac{\partial E_3}{\partial T}}{\frac{\partial E_3}{\partial D_3}}.$$

The strain term in A gives an additional temperature dependence compared to the stress free bulk scenario, so that

$$\frac{\partial E_3}{\partial T} = \left(\alpha - 2\frac{Q_{12}}{s_{11}+s_{12}} \frac{\partial u_0}{\partial T} \right) D_3.$$

From the expression for the in-plane strain

$$u_0 = \frac{a_s - a_0}{a_0},$$

the temperature dependence of the strain is found as

$$\frac{\partial u_0}{\partial T} = \frac{a_s}{a_0} (\gamma_s - \gamma_0),$$

where γ_s and γ_0 are the linear thermal expansion coefficients for the substrate and ferroelectric film respectively. The pyroelectric coefficient is then

$$p = -\frac{\alpha - 2\frac{Q_{12}}{s_{11}+s_{12}}\frac{a_s}{a_0}(\gamma_s - \gamma_0)}{\tilde{\kappa}_{33}} D_3,$$

where the inverse permittivity is also different from the constant stress value, as indicated by the tilde.

The effect of the depolarization field

The influence of the electric field in a thin film configuration can be accounted for by considering the equation of state in the form $f(T, D, E) = 0$,

$$f(T, D_3, E_3) = A(T)D_3 + BD_3^3 + CD_3^5 - K\frac{\partial^2 D_3}{\partial x_3^2} - E_3 = 0.$$

With the simplifying assumption that the film is insulating $\partial D_3/\partial x_3 = 0$. Under short circuit condition with two metal electrodes, the electric field in the film is

$$E_3 = -\frac{2\lambda}{\epsilon d} D_3,$$

where λ and ϵ are the screening length and the lattice contribution to the dielectric constant in the metal electrodes [136, ch. 26], and d is the ferroelectric film thickness. Substituting this into the equation of state gives a relation in terms of the temperature and displacement field alone. The total differential

$$df = \frac{\partial f}{\partial T} dT + \frac{\partial f}{\partial D_3} dD_3 = 0,$$

gives

$$\frac{dD_3}{dT} = -\frac{\partial f/\partial T}{\partial f/\partial D_3}.$$

The numerator gives α as before (corrected for in-plane strain), while the denominator now is corrected for the capacitance associated with the electrodes

$$\frac{\partial f}{\partial D_3} = \tilde{\kappa}_{33} + \frac{2\lambda}{\epsilon d}.$$

The pyroelectric coefficient is thus

$$p = -\frac{\alpha - 2\frac{Q_{12}}{s_{11}-s_{12}}\frac{a_s}{a_0}(\gamma_s - \gamma_0)}{\tilde{\kappa}_{33} + \frac{2\lambda}{\epsilon d}} D_3. \tag{2.9}$$

Equation (2.9) can be used to compare the theoretical pyroelectric response to the measured one. For polydomain samples, assuming that the domain wall contribution to the total area is negligible, the pyroelectric response is determined by the average polarization over the total electroded area.

Chapter 3

Experimental techniques

This chapter describes the techniques used for growing and characterizing the thin films, i.e. sputter deposition, x-ray diffraction, photoelectron spectroscopy, atomic force microscopy and dielectric characterization. The pyroelectric measurements are described in chapter 4.

3.1 Sputter deposition

All samples in this study were grown by sputter deposition. In sputter deposition, ions are accelerated towards a target composed of the material to be deposited. The ions collide with the target, and sets off a series of cascade collisions, leading to transferal of energy to atoms that are subsequently emitted from the target surface. A detailed description of the sputtering process can be found in Ref. [137]. Some of the sputtered atoms are adsorbed and forms a thin film on a substrate placed in the vicinity of the target.

A radio-frequency power source is connected to the sputtering gun when sputtering dielectrics. At frequencies above a few MHz the mobility of the ions in the plasma is too low to follow the instantaneous field variation, leading to a higher electron current toward the target in the positive half-cycle than ion current in the negative half-cycle [138]. A dc-bias develops on the target, until steady-state conditions are reached, with equal ion and electron currents.

A particular challenge with sputter deposition of oxide thin-films is selective re-sputtering of the growing film by negative oxygen ions. One way of mitigating this is to use an off-axis geometry. This geometry positions the sample outside of the plasma and outside of the direct path of oxygen ions accelerated by the sheath voltage at the sputtering target [139, 140]. A general overview of control of film properties in sputter deposition can be found in Ref. [141].

An off-axis rf-magnetron sputtering tool was used in this study. Typical deposition parameters were total pressures from 100 to 170 mTorr, flow rates of 10 sccm Ar and 4 sccm O_2, and forward deposition power of 90 W. The targets were commercial 3" ceramic targets of $Pb_{1.1}TiO_3$ and $SrRuO_3$. A 10% Pb excess was used to compensate for Pb evaporation at high growth temperatures [142].

Films were grown on $SrTiO_3$ substrates that were etched with buffered HF acid and annealed, to achieve a single terminated TiO_2 surface prior to growth [143, 144].

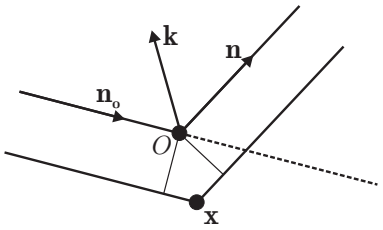

Figure 3.1: Scattering of x-rays on two scattering centres. The phase difference between radiation scattered at the two centres is determined by the distance vector **x** and scattering vector **k**, see text. After Guinier [145].

3.2 X-ray diffraction

X-ray diffraction was used to determine the lattice constants of the films, and to measure the epitaxial relationship between the film and the substrate. The coherent scattering of x-rays by electrons in crystalline solids gives rise to diffraction peaks, or directions in space where the electro-magnetic radiation interferes constructively, yielding a high intensity. These diffraction lines are used to determine the structure of the solid.

For two or more scattering centres, as in Fig. 3.1, the amplitude of the coherently scattered radiation is the sum

$$A = A_0 \sum_i f_i \exp(i\phi_i),$$

where f_i are the scattering factors of the centres, and ϕ_i the phase differences from radiation scattered at an arbitrary origin. For the two centres shown in Fig. 3.1, the phase difference is

$$\phi = -2\pi \mathbf{x} \cdot \frac{\mathbf{n} - \mathbf{n}_0}{\lambda},$$

where $\mathbf{x}$ is the distance vector between the centres, λ is the wavelength of the radiation, and $\mathbf{n}_0$ and $\mathbf{n}$ are unit vectors in the direction of the incident radiation and the direction of interest for the scattered radiation, respectively. The wavelength and direction dependencies are contained in the scattering vector

$$\mathbf{k} = 2\pi \frac{\mathbf{n} - \mathbf{n}_0}{\lambda}.$$

For a given wavelength, the range of accessible scattering vectors is given by the Ewald sphere of radius $2\pi/\lambda$.

For atoms, the scattering power is represented by the scattering factor f

$$I_{\text{coh}} = f^2 I_e,$$

where I_{coh} is the intensity of the coherently scattered radiation and I_e the Thompson scattering intensity for electrons [145, p. 11]. As a generalization of the scattering from discrete centres, the scattering factor is determined by an integral over the electron density [145, p. 15]

$$f(\mathbf{k}) = \int \rho(\mathbf{x}) \exp(-i\mathbf{k} \cdot \mathbf{x}) dv.$$

For an entire solid, the scattered amplitude is expressed as

$$A(\mathbf{k}) \propto \int \rho(\mathbf{x}) \exp(-i\mathbf{k} \cdot \mathbf{x}) dv,$$

which is the Fourier transform of the electron density.

For crystalline solids it is convenient to utilize the translation symmetry, and describe the crystal in terms of the lattice and the unit cell. The lattice is defined by the set of lattice vectors $\mathbf{R} = p\mathbf{a}+q\mathbf{b}+r\mathbf{c}$, where $\mathbf{a}$, $\mathbf{b}$, and $\mathbf{c}$ are three vectors, not all in the same plane, connecting the lattice points, and p,q, and r run through all integers. The electron density of the whole crystal is then written as the convolution of the electron density of the unit cell and the lattice multiplied by the form factor of the object [145, p. 84]. The form factor of the object is given by the shape of the crystal, and is unity inside the object, and zero outside.

The amplitude of the coherently scattered radiation is found by calculating the Fourier transform of the electron density. By the convolution theorem, the Fourier transform of the electron density is the product of the Fourier transform of the electron density in the unit cell, called the structure factor, and the convolution of the Fourier transforms of the lattice, which gives the reciprocal lattice, and of the form factor of the object.

For a perfect, but finite crystal, the transform of the form factor for the object determines the width of the diffraction lines. For an infinite crystal, the Fourier transform of the form factor of the object is a delta function in reciprocal space, and the diffraction lines are sharp. As the dimensions of the crystal are reduced, the diffraction lines broadens. For a thin film, the transform of the form factor for the object is a product of delta functions of the in-plane coordinates and a sinc function in the out-of-plane coordinate, with characteristic oscillations that are determined by the film thickness.

Figure 3.2 illustrates a plane in the reciprocal lattice. For a fixed relation between the incident radiation and the crystal, the diffraction lines corresponds to intersections of the reciprocal lattice points, broadened by the form factor of the crystal, and the Ewald sphere, given as a circle in the figure. In general, there will be no such intersection, and no diffraction lines. One way of forcing an intersection is to rotate the crystal with respect to the incident radiation direction. This is illustrated in Fig. 3.2b).

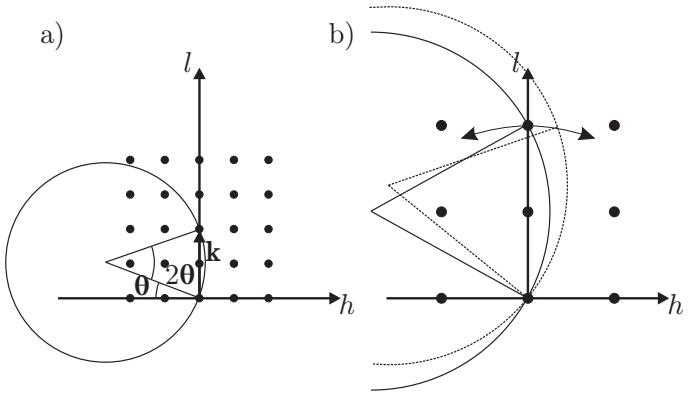

Figure 3.2: a) A plane in reciprocal space. The circle indicate a section of the Ewald sphere. Simultaneously changing the angles θ and 2θ yields a scan along the l axis, a $\theta/2\theta$ scan. b) Illustration of a rocking curve measurement. Changing the angle θ gives a measure of the width of the diffraction peak, or of the amount of crystallites with slightly different orientation, the mosaic spread.

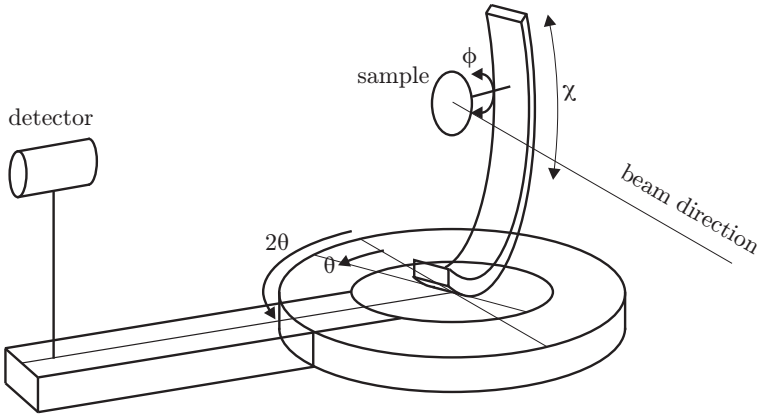

Figure 3.3: Illustration of a 4-circle goniometer. The sample can be rotated through the angles θ, ϕ, and χ with respect to the incident radiation. The point detector can be rotated through the angle 2θ.

In practice the crystal is mounted on a goniometer, as in Fig. 3.3. For a four-circle goniometer, the crystal can be rotated with respect to the incident radiation through the angles θ, ϕ, and χ, as indicated on the figure. In addition, the detector for the scattered radiation can be moved along the angle 2θ. In this study we have used $\theta/2\theta$ scans, where the crystal is rotated an angle θ and the detector an angle 2θ, to determine the out-of-plane lattice constant and the film thickness. Such a scan, illustrated in Fig. 3.2 a), gives a straight scan along the l axis in reciprocal space when the crystal has been properly aligned. Rocking curves, where the detector angle is fixed and the crystal rotated an angle $\Delta\theta$, have been used to determine the width of the $(00l)$ peaks to give a measure of the mosaic spread in the films. The intensities have also measured in an area of the reciprocal space, a reciprocal space map (RSM), to determine the relation between the in-plane lattice of the substrate and the thin film. Several instruments were used in the study. The typical measurement configuration was incident monochromatic CuKα_1 radiation, with a wavelength of 1.5406 Å. The scattered radiation was detected with a scintillating point detector. For high resolution measurements the acceptance angle of the detector was set to 0.04°, and the incident radiation had a divergence of $< 0.02°$ in the scattering plane.[1]

3.3 X-ray photoelectron spectroscopy

X-ray photoelectron spectroscopy was used to investigate the surface composition of the films. In this technique, x-ray photons are used to excite atoms in the film, leading to electron emission. The escape depth of the electrons is of the order of a few nm, so the technique is surface sensitive [146, p. 9]

The experimental setup is illustrated in Fig. 3.4. An x-ray source illuminates the sample and the emitted electrons are analysed and detected. The kinetic energy of the emitted electron is [146, p. 4]

$$E_k = h\nu - \Phi - |E_B|,$$

where $h\nu$ is the photon energy, Φ the work function of the solid, and E_B the binding energy of the electron. Figure 3.5 illustrates the relation between the measured spectrum and the energy levels in the solid. The binding energy is in a first approximation equal to the negative orbital energy (Koopmans' binding energy) [146, p. 42], and serves as an identification of the atoms present in the sample and their chemical bonding.

For a hemispherical sector analyser, consisting of two concentric hemispheres, the emitted electrons are analysed by applying a potential difference between the

[1]The acceptance angle was defined using slits, while the divergence angle is an upper limit estimate from the width of the x-ray beam at the detector plane.

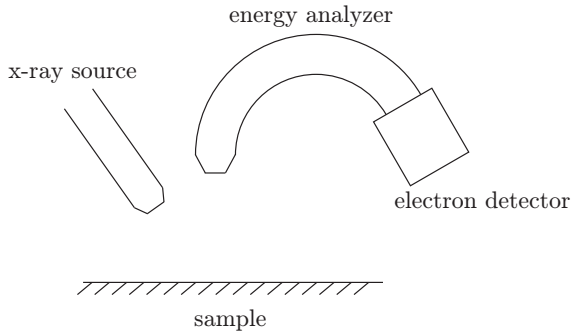

Figure 3.4: Schematic of the XPS setup. An x-ray source illuminates the sample, and the photoemitted electrons are analysed and detected. After Hüfner [146].

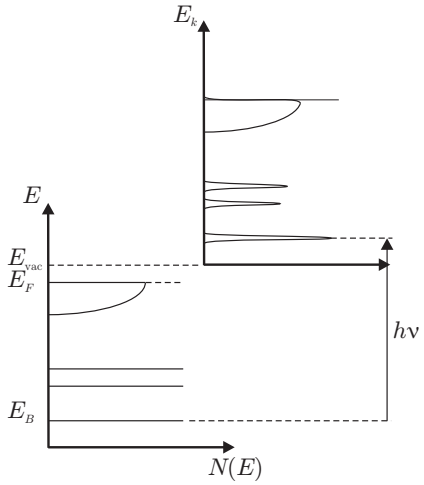

Figure 3.5: Illustration of the relation between the electron energy levels in the solid and the photoemission spectrum. The diagram on the left represents the binding energy of the electrons in the solid, and the diagram on the right the kinetic energy of the emitted electrons. After Hüfner [146].

outer and inner hemispheres, with the inner hemisphere at a higher potential. The electrons will follow curved trajectories in the analyser, and only electrons of a certain kinetic energy will have a path with the same curvature as the hemispheres, and be detected.

Here, unmonochromatized MgKα radiation of energy 1253.6 eV was used to excite the electrons. The spectrums were recorded in the constant analyser energy mode, with a bandpass energy of 20 eV. The raw data was smoothed with Savitzky-Golay filtering [147]. The line profiles was found by fitting Voigt functions and a Shirley background from inelastically scattered electrons [148] to the filtered data, using a least-squares method. Relative integrated peak intensities were estimated from the fitted profiles to give information on the composition with growth temperature.

3.4 Atomic force microscopy

Atomic force microscopy (AFM) is a versatile scanning probe technique for surface studies. The basis for the method is a small tip, mounted on a cantilever as in Fig. 3.6, that is scanned over the sample surface. The force between the tip and sample surface is measured by the deflection of the cantilever. In this work we have used the tapping-mode for topography studies. In tapping-mode the cantilever is vibrated at a frequency close to the resonance frequency of the cantilever, and the tip-surface separation decreased until a fixed vibration amplitude is achieved. The sample is raster scanned and the feedback mechanism adjusts the sample height to maintain the fixed cantilever vibration amplitude. We used AFM tips with length ~ 15 μm, nominal tip radius of 8 nm, and resonance frequency for the cantilever of ~ 300 kHz.

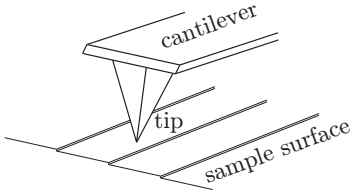

Figure 3.6: Illustration of an AFM tip on a cantilever. The tip is scanned across the sample surface, and the force between the tip and sample measured through the deflection of the cantilever.

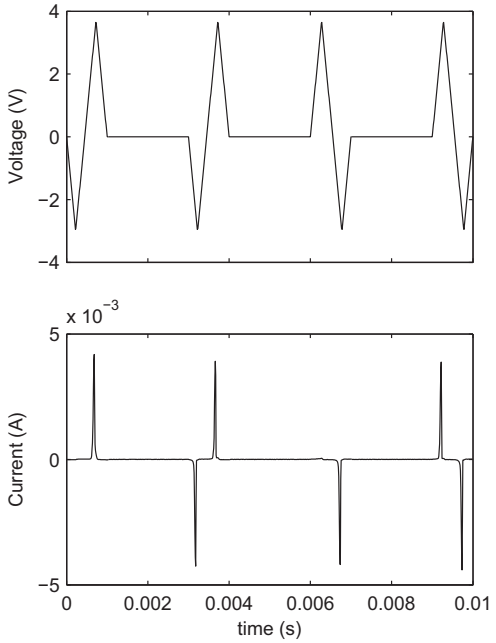

Figure 3.7: Asymmetric voltage pulses used for the polarization measurements. The first and third pulse sets the polarization state. The polarization is calculated from the measured current in the positive half-cycle of the second pulse and the negative half-cycle of the fourth pulse.

3.5 Polarization and capacitance measurements

The polarization hysteresis loops and capacitance was measured with an Aixacct TF 2000 thin film analyser.

The polarization is measured as the time integral of the current flowing during the application of triangular voltage pulses, similar to the Sawyer-Tower principle [149], except that the current is integrated numerically by a computer instead of by a capacitor. Asymmetric voltage pulses as in Fig. 3.7 was used to avoid high leakage currents, while simultaneously approaching full saturation of the polarization. The positive and negative maximum voltages was set independently, while the pulse length was fixed at 1 ms. Four pulses were used to measure the complete hysteresis loop. The first and third pulses set the polarization in the relaxed positive and negative state, respectively. The positive half-cycle of the second pulse and negative half-cycle of the fourth pulse was used to calculate the polarization. The relaxation

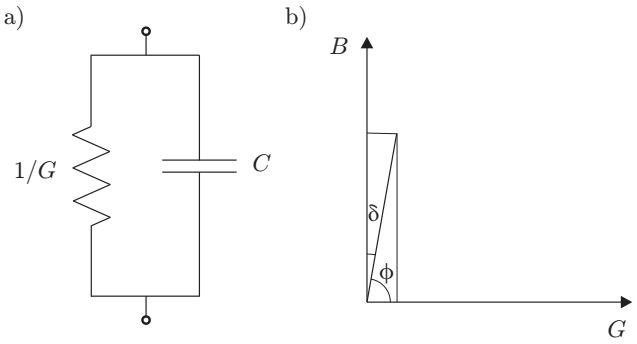

Figure 3.8: a) An electrical equivalent circuit for a thin film. A parallel connection of an ideal resistor and capacitor. b) The admittance in terms of the conductance and the susceptance. The phase angle ϕ and the loss angle δ are indicated.

time between each pulse was 2 ms.

The capacitance is determined through the relation between induced current and applied voltage for low-level sinusoidal voltage signals. For a linear response, with complex notation $\tilde{V} = V_0 e^{i\omega t}$,

$$\tilde{I} = Y\tilde{V},$$

where Y is the admittance. The actual voltage and current are the real part of their complex representation, $V = \Re\{\tilde{V}\} = V_0 \cos(\omega t)$ and $I = \Re\{\tilde{I}\} = I_0 \cos(\omega t + \phi)$. For an ideal capacitive element

$$I = C\frac{dV}{dt},$$

and the admittance is

$$Y = i\omega C.$$

For a general linear response, $Y = G + iB$, where G is the conductance and B the susceptance. The conductance and susceptance are determined by measuring the amplitude and the phase of the current

$$\frac{I_0}{V_0} = \sqrt{G^2 + B^2},$$

$$\tan(\phi) = \frac{B}{G}.$$

A simple model of a dielectric thin film at low frequencies ($\sim$ kHz) in terms of electrical components is a parallel connection of an ideal capacitor and an ideal resistor, as in Fig. 3.8. From this equivalent circuit, the capacitance is determined as

$$C = \frac{B}{\omega}.$$

The loss tangent

$$\tan(\delta) = \frac{G}{B}$$

gives a measure of the lossyness of the film.

The capacitance was measured with an AC amplitude of 50 mV, at a frequency of 2 kHz. The loss tangent was less than 0.1 for all reported data, showing considerable leakage for very thin films, and adding an uncertainty to the data for very thin films of the same order as the observed variation.

Electrical contact to the thin films was made through circular contact pads with diameter 400 μm, deposited *ex situ* (200 nm Au/50 nm Pt) on the surface, and a continuous bottom electrode of $SrRuO_3$ or Nb doped $SrTiO_3$.

Chapter 4
Pyroelectric measurements

The dynamic pyroelectric method was originally used by Chynoweth to characterize $BaTiO_3$ single crystals, and shown to be a useful complementary method to standard dielectric hysteresis loops [118]. The pyroelectric response can be measured independently of applied external electric fields, and is an attractive way of measuring the initial polarization state, as well as monitoring the variation of the polarization with time. The initial polarization state gives information on asymmetries existing in the thin film structure, and the variation of the polarization with time gives information on the stability of the polarization.

4.1 Experimental setup

The experimental setup is illustrated in Fig. 4.1. The pyroelectric current from the ferroelectric capacitor is generated by illuminating the top electrode with a modulated laser beam, thereby causing a temperature modulation. The resulting current is detected with a lock-in amplifier. A current to voltage converter, based on a Burr Brown OPA627AP operational amplifier, is used to ensure short-circuit conditions during the measurement of the pyroelectric current. The polarization is manipulated by isolating the ferroelectric capacitor under test from the detection circuit, and applying a voltage between the top- and bottom-electrode.

In order to estimate the theoretical pyroelectric response and the dependence on the modulation frequency, the temperature variation induced in the ferroelectric film must be found.

4.2 Induced temperature variation

The geometry of the system is as shown in Fig. 4.2: the top electrode of thickness 250 nm and radius 200 μm, the ferroelectric film of thickness <200 nm, the bottom electrode of thickness $\sim$ 100 nm, and the substrate of thickness $\sim$ 500 μm. The top surface is illuminated in the center with a laser spot of radius less than the electrode radius.

One-dimensional approximation

In one dimension the equation of conduction of heat for a homogenous material is [150, p. 9]

$$\frac{\partial T}{\partial t} = \frac{\lambda}{\rho c}\frac{\partial^2 T}{\partial z^2},$$

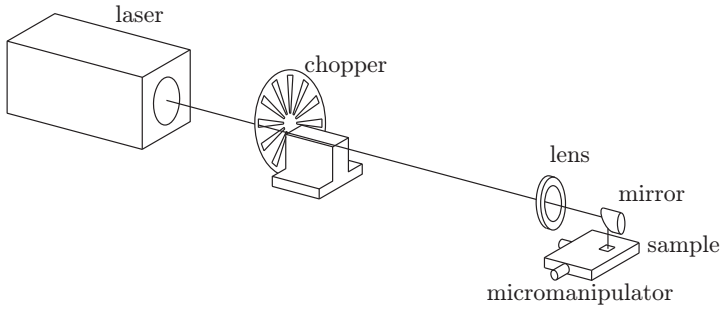

Figure 4.1: Schematic pyroelectric measurement setup. The laser beam is modulated by a mechanical chopper. The light is focused on the top electrode, and the resulting current detected with a lock-in amplifier.

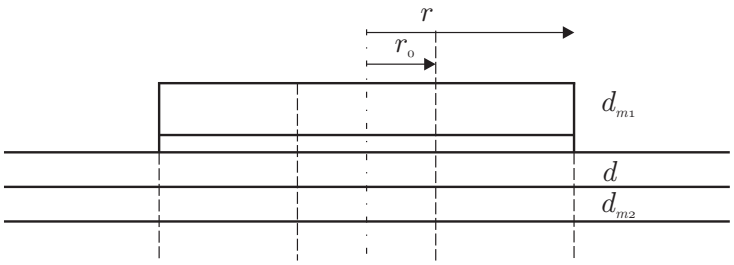

Figure 4.2: Illustration of capacitor structures. The capacitor consists of a circular top electrode of radius r and thickness d_{m1}, a continuous ferroelectric film of thickness d, a continuous bottom electrode of thickness d_{m2}, and a thick substrate.

Table 4.1: Thermal constants for the materials in the experimental study.

Material	λ [W m^{-1} K^{-1}]	c [J mol^{-1} K^{-1}]	ρ_{mol} mol/m^3	Ref.
Au	317	25.42	9.81×10^4	[151, p. 65]
Pt	71.6	25.85	10.99×10^4	[151, p. 139]
$PbTiO_3$	3	130	2.62×10^4	[152, p. 362]
$SrRuO_3$	6	108	2.75×10^4	[153]
$SrTiO_3$	10	150	2.79×10^4	[152, p. 313]

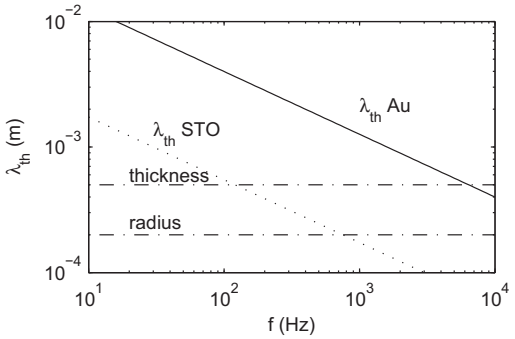

Figure 4.3: The thermal wavelength for Au and $SrTiO_3$ in a one-dimensional solution of the equation of conduction of heat. For frequencies below ~ 10 kHz the thermal wavelength is much larger than the contact radius.

where T is the temperature, λ the thermal conductivity, ρ the density, and c the specific heat of the material. The general steady-state solution for a sinusoidal time varying temperature is

$$T(z,t) = \Re\left\{\left(ae^{\kappa z} + be^{-\kappa z}\right) e^{-i\omega t}\right\},$$

where $\kappa = \sqrt{i\omega\rho c/\lambda}$, and $\Re\{\}$ indicates the real part of the argument. This represents a thermal wave with wavelength $\lambda_{th} = 2\pi/\Im\{\kappa\}$, where $\Im\{\}$ indicates the imaginary part of the argument. The thermal constants for the materials used in the experimental study are shown in table 4.1, and Fig. 4.3 shows the thermal wavelength in Au and $SrTiO_3$ for modulation frequencies from 10^1 to 10^4 Hz. The contact radius and the substrate thickness are also indicated in the figure. It is seen that for frequencies below ~ 10 kHz the thermal wavelength in Au is much larger than the contact radius. Assuming no heat transfer along the perimeter of the contact

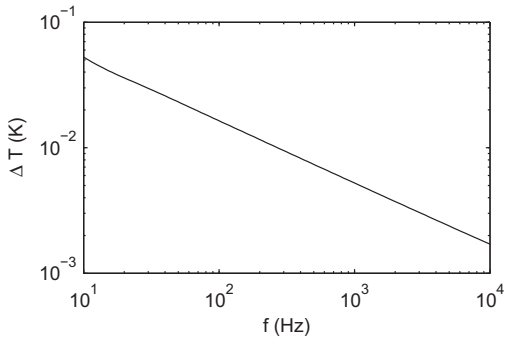

Figure 4.4: The surface temperature calculated for a capacitor with a Au/Pt (200 nm/50m) top electrode, 100 nm $PbTiO_3$ film, 100 nm $SrRuO_3$ bottom electrode, on a 500 μm $SrTiO_3$ substrate.

this means that the temperature in the top electrode along the radial direction can be assumed practically constant, and a one-dimensional approximation is meaningful. Ideally, for a one-dimensional approximation, the thermal wavelength in the substrate should be short compared to the radius of the top electrode. This is only fulfilled at high frequencies.

The temperature in the capacitor structure was found with a matrix method [150, ch. 3.7], and Fig. 4.4 shows the calculated surface temperature response for a typical capacitor. The heat flux at the surface was estimated at

$$j_1 = (1 - R)P/A = 0.7480 \text{ W/cm}^2,$$

assuming a reflectivity constant R of 0.9765 for Au [154], and an input power P of 40 mW on the electrode area A. The amplitude of the temperature variation is seen to follow a $\sim \omega^{-1/2}$ dependence. Bearing in mind that the one-dimensional approximation is valid only for a limited frequency window, the temperature variation should deviate from the inverse square root dependence at low frequencies, where the effective heat capacitance is larger than what assumed in the one-dimensional model. This deviation will be slight for the surface temperature, however, and it is the surface temperature that determines the pyroelectric response.

4.3 Pyroelectric response

From chapter 2.2.3, for a sinusoidal temperature variation of frequency ω, the magnitude of the pyroelectric current density is

$$|j| = \left|\frac{dD}{dT}\right| \omega \Delta T(\omega),$$

Table 4.2: Elastic constants for $PbTiO_3$.

Q_{11} $\times 10^{-2}$ m^4/C^2	Q_{12} $\times 10^{-2}$ m^4/C^2	s_{11}^E $\times 10^{-12}$ m^2/N	s_{12}^E $\times 10^{-12}$ m^2/N	Ref.
8.1 – 8.9	-2.6 – -3.9	-	-	[155]
6.6	-3.2	-	-	[156]
8.9	-2.6	-	-	[129]
-	-	7.5	-1.5	[157]
-	-	7.2	-2.1	[158]

and should follow a $\omega^{1/2}$ behaviour. The experimental data gave an ω^n behaviour in the frequency range from 100 Hz to 3 kHz, with n varying from 0.43 to 0.48 in different samples. Values of the electromechanical, elastic, and dielectric constants in (2.9) are needed for a numerical estimate of the pyroelectric coefficient. The electrostrictive coefficient is known from literature. The elastic compliance coefficients in the literature are usually measured under constant electric field, and the corresponding coefficients under constant displacement field must be found.

Elastic compliance coefficients

General procedures for finding the relationship between compliance tensors observed under various constraints are given by Grindlay [127, p. 56, p. 98]. The elastic compliance coefficients under constant displacement can be found as

$$s_{\alpha\beta}^D = s_{\alpha\beta}^E + \left(\frac{\partial u_\alpha}{\partial D_j}\right)_{\sigma,T} \left(\frac{\partial D_j}{\partial E_i}\right)_{\sigma,T} \left(\frac{\partial E_i}{\partial \sigma_\beta}\right)_{D,T},$$

so that in a tetragonal state with $D_1 = D_2 = 0$,

$$s_{11}^D = s_{11}^E - 4(Q_{12}D_3)^2\epsilon_{33},$$

and

$$s_{12}^D = s_{12}^E - 4(Q_{12}D_3)^2\epsilon_{33}.$$

From the literature values of the elastic compliance coefficients in table 4.2, and zero stress spontaneous polarization and dielectric constant as calculated from the elastic Gibbs free energy (2.6), with parameters from table 4.3, $s_{11}^D = 6.3 \times 10^{-12}$ m^2/N and $s_{12}^D = -3.0 \times 10^{-12}$ m^2/N.

The dielectric constant with in-plane strain

The inverse permittivity is

$$\tilde{\kappa}_{33} = \frac{\partial}{\partial D_3} \frac{\delta \tilde{\mathfrak{G}}_1}{\delta D_3}.$$

Table 4.3: Dielectric stiffness coefficients for $PbTiO_3$. From [129].

α_1	-1.708×10^8 m/F
α_{11}	-7.252×10^7 m^5/C^{2}F
α_{111}	2.606×10^8 m^9/C^{4}F

From (2.5), with coefficients derived from table 4.3, and a strain of $u_0 = -0.014$, the inverse permittivity is estimated at

$$\tilde{\kappa}_{33} = 2.53 \times 10^9 \text{ m/F}.$$

In the tetragonal state the inverse permittivity tensor is diagonal, so that the relative dielectric constant is

$$\tilde{\epsilon}_{33} = \epsilon_0^{-1}\tilde{\kappa}_{33}^{-1} = 44.68,$$

which is less than the measured dielectric constant $\epsilon_{33} = 69$ (Paper II). Conversely, the measured dielectric constant gives an inverse permittivity of $\tilde{\kappa}_{33} = 1.64 \times 10^9$ m/F. The Landau-Ginzburg-Devonshire theory also underestimates the room-temperature bulk dielectric constant [129]. The discrepancy between measured and calculated values can result from contributions from domain-wall motion and defects to the measured dielectric constant. The range of validity for the Landau-Ginzburg-Devonshire, where room-temperature data are predicted from measured quantities near the phase-transition temperature with only one temperature dependent parameter, can also be questioned. For the theoretical estimate of the pyroelectric coefficient we use the theoretical value of the inverse permittivity.

The pyroelectric coefficient

The numerical estimate of the pyroelectric coefficient from (2.9) and thermal expansion coefficients from table 4.4 is

$$p = \frac{dD}{dT} = -\frac{\alpha - 2\frac{Q_{12}}{s_{11}^D + s_{12}^D}\frac{\partial u_0}{\partial T}}{\tilde{\kappa}_{33} + \frac{2\lambda}{\epsilon d}} D = -1.02 \times 10^{-4} \text{ C/m}^2\text{K}.$$

However, at high measuring frequencies, only the surface layer experiences a temperature variation, making the effective thermal expansion of the substrate zero. This gives an estimated pyroelectric coefficient of

$$p = \frac{dD}{dT} = -5.29 \times 10^{-5} \text{ C/m}^2\text{K}.$$

Table 4.4: Thermal expansion coefficients for $PbTiO_3$ and $SrTiO_3$.

$PbTiO_3$ K^{-1}	$SrTiO_3$ K^{-1}	Ref.
12.6×10^{-6}	-	[129]
-	10.7×10^{-6}	[159]

With an estimated temperature variation at 2 kHz of 3.6×10^{-3} K (fig. 4.4), the expected current density is 2.4 mA/m^2, compared to the measured current density

$$j \approx \frac{0.4}{0.12} \frac{\text{nA}}{\text{mm}^2} = 3.3 \text{ mA/m}^2.$$

The theoretical estimate of the pyroelectric response is seen to be in reasonable agreement with the measured value.

Paper I
Imaging of out-of-plane interfacial strain in epitaxial $PbTiO_3/SrTiO_3$ thin films

Published in Applied Physics Letters **86**, 092907 (2005).

Imaging of out-of-plane interfacial strain in epitaxial $PbTiO_3/SrTiO_3$ thin films

A. T. J. van Helvoort
Department of Physics, Norwegian University of Science and Technology, 7491 Trondheim, Norway
Ø. Dahl
Department of Electronics and Telecommunications, Norwegian University of Science and Technology, 7491, Trondheim, Norway
B. G. Soleim and R. Holmestad
Department of Physics, Norwegian University of Science and Technology, 7491 Trondheim, Norway
T. Tybell[a)]
Department of Electronics and Telecommunications, Norwegian University of Science and Technology, 7491, Trondheim, Norway

In this study, we rely on low-angle annular dark-field scanning transmission electron microscopy to probe the interface strain profile in epitaxial $PbTiO_3/SrTiO_3$ thin-films. All samples displayed a compressively strained layer at the $PbTiO_3/SrTiO_3$ interface, with the strain vector parallel to the polarization direction. The width of the strained layer was found to be $\sim 15-30$ Å, dependent on the electrode environment. Our findings open a perspective to use interface strain engineering in combination with control of electrostatic boundary conditions as a tool to monitor the effective interface polarization. These findings have implications for future use of ferroelectrics in electronic and mechanical devices.

Ferroelectric materials are interesting for use in a variety of applications ranging from nonvolatile memories to micro/ nanoelectromechanical devices.[1] In most electronic devices, understanding and control of the interface between the ferroelectric material and the electrode is important. Several ferroelectric field effect devices have been proposed and realized.[2–4] A large polarization is often desired, leading to substantial carrier modulation in the active channel. For the successful implementation of such approaches, a detailed knowledge of the interface polarization is central. It is worth noting that ferroelectric properties are sensitive to strain. Moreover, ferroelectrics are subject to size effects as the dimensions of the sample are reduced,[5–8] and there has been reported ferroelectricity with inferior polarization in ultrathin films when the thickness is reduced.[9] Thus, the understanding and control of the interface polarization pose significant challenges for using ferroelectrics in future nanoelectronics.

In this letter, we use low-angle annular dark-field (ADF) scanning transmission electron microscopy (STEM)[10] to show that epitaxial $PbTiO_3/SrTiO_3$ (PTO/STO) films display a strained interface. The direction of the strain is colinear with the polarization direction, corresponding to a reduced c-axis lattice parameter of the PTO thin film in the first few unit cells. This observation is crucial for further downscaling and to the design of future device applications of ferroelectric thin films.

High-quality (001)-oriented PTO films with a thickness between 50 and 200 Å were epitaxially grown on (001) oriented STO substrates using off-axis radio-frequency magnetron sputtering. Both insulating STO and conducting Nb doped STO substrates were used. Atomic force microscopy topographic measurement revealed smooth surfaces with a root-mean-square roughness of $\sim 3-5$ Å over 1×1 μm. Rocking curve measurements on the (001) reflection typically displayed a full width at half maximum $< 0.1°$. $\theta - 2\theta$ x-ray diffraction (XRD) analysis revealed distinct size effects around the (001) and (002) reflections, which were used to carefully estimate the film thickness. The XRD analysis revealed

[a)]Also at: NTNU Nanolab, Realfagbygget, Norwegian University of Science and Technology, 7491 Trondheim, Norway; author to whom correspondence should be addressed; electronic mail: thomas.tybell@iet.ntnu.no

a gradual decrease in the measured c-axis lattice parameter from the bulk value of 4.16 Å, for films thinner than $\sim$ 200 Å. A similar decrease in c-axis lattice parameter as a function of film thickness was recently reported by Lichtensteiger et al.[9]

In the present study, a JEOL 2010F transmission electron microscopy (TEM)/STEM (200 kV field emission gun, C_s = 1.0 mm) instrument was used to study mechanically thinned and argon-ion milled PTO thin-film cross-sections. The scanning electron probe was smaller than 0.2 nm in diameter, and the scattered electrons were collected by a JEOL ADF detector with a collecting angle ranging from 9 to 174 mrad.

Figure 1(a) shows a high-resolution image of a cross-section TEM sample for a 51 Å thick PTO film on STO. As can be seen, the interface is congruent without any misfit dislocations in this region. This finding was confirmed by high-resolution, high-angle ADF STEM, sensitive to the atomic number Z,[11] as displayed in Fig. 1(b). Such high-quality interfaces were seen consequently for all samples studied. Electron diffraction patterns taken at the interface, as seen in the inset of Fig. 1(a), confirmed the in-plane coherency, with no splitting of the (0k0) PTO and STO reflections up to the fourth order. Subsequently, we have measured the low-angle ADF response, which is sensitive to strain contrast.[10] Figure 2(a) depicts the low-angle (9-24 mrad) ADF response for the interface of a 191 Å PTO/STO sample. A band with an increased intensity was present at the film substrate interface. Such bright bands were found in all samples, irrespectively of whether they were grown on insulating or conducting substrates. The increased low-angle ADF intensity of the PTO/STO interface was independent of the TEM sample thickness for samples thicker than $\sim$ 20 nm. Moreover, the width and relative intensity of this bright band were the same for samples studied at room temperature and at -150 °C. Based on the findings above, the observed effect is attributed to strain contrast and not to additional phonon scattering,[12] nor thickness variations, compositional variations,[13] or local interfacial defects.[14] However, the increased intensity at the upper film surface, as seen in Fig. 2(a), is related to an extrinsic effect related to charging of the TEM sample.

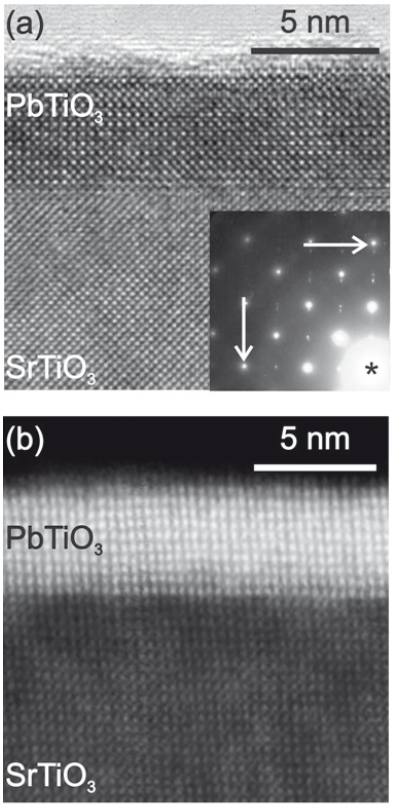

FIG. 1. (a) High-resolution cross-section TEM image of a high-quality 51 Å thick film of PTO grown on STO. Inset: [100] Electron diffraction pattern with coherent (040) PTO/STO (vertical arrow) and splitting in the (004) (horizontal arrow) reflections. The * marks where (000) is located. (b) High- angle (26-69 mrad) ADF image showing Z contrast.

The electron diffraction data of the PTO/STO interfaces revealed good epitaxy, thus discarding a reduced lattice mismatch due to misfit dislocations as the cause of the bright bands observed in low-angle ADF STEM. Tilting the samples relative to the electron beam in the [010] direction and thereby keeping the interface "edge on," resulted in similar intensity variations, as seen in Fig. 2(b). These findings suggest that the observed contrast is due to lattice strain parallel to the PTO

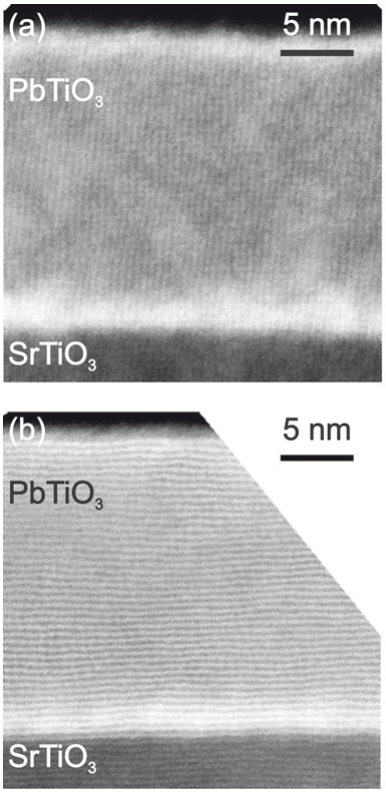

FIG. 2. (a) Low-angle (9-24 mrad) ADF image of 191 Å PTO film grown on STO showing strain contrast at the interface and the top surface. (b) The same film tilted by 6° along [010] revealing a c-axis compressive strained layer. White right top corner is end of imaging area.

[001] direction, hence the strain is parallel to the polarization vector. Careful comparison between the lattice parameters in the bright band relative to the one of the volume of the thin films unveiled a reduced *c*-axis lattice parameter near the film/substrate interface. We note that the observed layer with a reduced *c*-axis lattice parameter gives a contribution to the film thickness dependent decrease in the effective c-axis value for the thinnest samples, as observed by XRD analysis.

From the intensity profile in Fig. 3, we measured the size of the bright interfacial layer to be 27-30 Å i.e., about 7 unit cells of PTO

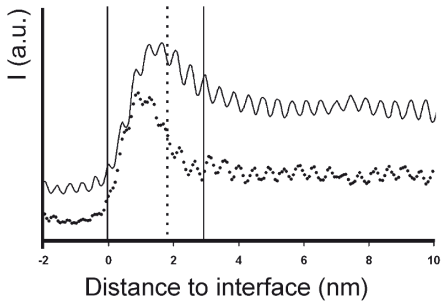

FIG. 3. Intensity profile, averaged over 7 nm parallel to the interface, for a 191 Å PTO film on STO (upper full line) and a 201 Å PTO film on Nb-doped STO (lower dotted line) with indicated bandwidth (vertical lines). The bandwidth is defined as the distance from the interface, as determined by the first Pb column, to the position where the intensity is one-half of the maximum mean intensity in the band relative to the mean intensity in the bulk of film.

grown on insulating STO (full line). The same layer thickness was obtained for all film thicknesses studied. In real applications, the electrostatic boundary conditions are important.[7,8] Therefore, we also studied the strain contrast in thin PTO films grown on metallic Nb-doped STO. These films all display a smaller interface strained layer, typically 18-20 Å wide, as illustrated in Fig. 3 (dotted line) for a 201 Å thick film. Hence, by changing the electrostatic boundary conditions, the width of the strained layer is altered. Films grown on insulating STO with a Pt/Au electrode deposited at room temperature showed strained layers of similar thickness as films deposited on metallic substrates, 16-20 Å.[15]

PTO is known to exhibit a strong polarization-strain coupling,[16] which implies that the effective polarization is reduced in the compressively strained layer as compared to the bulk of the film. This has implications for applications reliant on the polarization at the interface, since the figure of merit for such devices will depend on interfacial strain. Based on the polarization-strain coupling, we note that the strained layer implies the presence of a gradient in polarization, going from a thin-film saturation polarization in the volume

of the film to a smaller finite value at the interface. The observed compressively strained layer is possibly a measure of the intrinsic evolution of the ferroelectric order parameter at an interface.

In conclusion, we have used low-angle ADF STEM to probe the strain profile in epitaxial PTO/STO thin films. All samples displayed a layer of *c*-axis strain at the interface, related to a decrease in the *c*-axis lattice parameter for the first few unit cells of the PTO films. This finding opens the possibility for using interface strain engineering, possibly in combination with the electrostatic boundary conditions, to tailor the effective interface polarization for future ferroelectric electronic and mechanical devices.

J.-M. Triscone and M. Dawber are greatly acknowledged for constructive discussions, and J. K. Grepstad for careful reading of the manuscript. The authors would like to thank the Research Council of Norway for funding of the project "Micro- and Nano-based Materials Development," Contract No. 140553/420, and the NANOMAT nationally coordinated project "Oxides for Future Information and Communication Technology," Contract No. 158518/431.

[1] D. L. Polla and L. F. Fiancis, MRS Bull. **21**, 59 (1996).

[2] Y. Watanabe, Appl. Phys. Lett. **66**, 1770 (1995).

[3] C. H. Ahn, J.-M. Triscone, N. Archibald, M. Decroux, R. H. Hammond, T. H. Geballe, Ø. Fischer, and M. R. Beasley, Science **269**, 373 (1995).

[4] C. H. Ahn, T. Tybell, L. Antognazza, K. Char, R. H. Hammond, M. R. Beasley, Ø. Fischer, and J.-M. Triscone, Science **276**, 1100 (1997).

[5] S. Li, J. A. Eastman, J. M. Vetrone, C. M. Foster, R. E. Newnham, and L. E. Cross, Jpn. J. Appl. Phys., Part 1 **36**, 5169 (1997).

[6] T. Tybell, C. H. Ahn, and J.-M. Triscone, Appl. Phys. Lett. **75**, 856 (1999).

[7] P. Ghosez and K. M. Rabe, Appl. Phys. Lett. **76** (2000).

[8] J. Junquera and P. Ghosez, Nature (London) **422**, 506 (2003).

[9] C. Lichtensteiger, J.-M. Triscone, J. Junquera, and P. Ghosez, Phys. Rev. Lett. **94**, 047603 (2005).

[10] Z. Yu, D. A. Muller, and J. Silcox, J. Appl. Phys. **95**, 3362 (2004).

[11] P. D. Nellist and S. J. Pennycook, Ultramicroscopy **78**, 111 (1999).

[12] E. Abe, S. J. Pennycook, and A. P. Tsai, Nature (London) **421**, 347 (2003).

[13] P. M. Voyles, D. A. Muller, J. L. Grazul, P. H. Citrin, and H. J. L. Gossmann, Nature (London) **416**, 826 (2002).

[14] P. E. Batson, Phys. Rev. B **61**, 16633 (2000).

[15] Due to preferential ion milling during TEM sample preparation, this external electrode was not in direct contact with the films for the thinnest TEM sample.

[16] R. Cohen, Nature (London) **358**, 136 (1992).

Paper II

Crystalline and dielectric properties of sputter deposited $PbTiO_3$ thin films

Published in Journal of Applied Physics **103**, 114112 (2008).

Crystalline and dielectric properties of sputter deposited $PbTiO_3$ thin films

Ø. Dahl, J. K. Grepstad, and T. Tybell[a)]
Department of Electronics and Telecommunications, Norwegian University of Science and Technology, O.S. Bragstads plass 2a, NO-7491 Trondheim, Norway

The crystalline and dielectric properties of sputter deposited $PbTiO_3$ thin films were investigated as a function of the film thickness and growth temperature. The crystalline quality was found to be independent of film thickness from 2.4 to 200 nm. The capacitance of 0.12 mm^2 $Pt/PbTiO_3/SrRuO_3$ and $Pt/PbTiO_3/Nb{:}SrTiO_3$ capacitors was found to deviate from the ideal parallel plate capacitance for $PbTiO_3$ films thinner than 10 nm. The decrease in capacitance was consistent with field penetration into the electrodes. The surface Pb content, as determined from x-ray photoelectron spectroscopy, was found to decrease with increasing growth temperature from 700-760 °C. However, no change could be observed in the crystalline quality.

I. INTRODUCTION

When ferroelectric and related high dielectric constant materials are processed in thin film form, the dielectric constant generally decreases with decreasing film thickness.[1] The low frequency dielectric constant is commonly measured via the capacitance of parallel plate type capacitors, and the observed reduction in the dielectric constant is often rationalized in terms of an interfacial layer with low dielectric constant in series with the bulk dielectric. Such an interfacial layer is found in theoretical models of the polarization, where the loss of dipole-dipole interactions at the film surface results in a reduced dielectric constant.[2,3] In addition, the series capacitance associated with electric field penetration into the metal electrodes will also reduce the measured capacitance from the ideal parallel-plate capacitor value.[4,5] However, the microstructure of the thin film will affect the dielectric properties, and it is hard to separate the influence of thickness dependent variations in the microstructure on the dielectric constant from intrinsic thickness variations of the dielectric constant.

In particular, several studies on the dielectric properties of $PbZr_xTi_{1-x}O_3$ (PZT) films have reproduced the general thickness dependence.[6–9] Most of the data reported in literature, however, derives from polycrystalline films. Fujisawa et al.[10] found less thickness variation of the dielectric constant for epitaxial compared with polycrystalline PZT films. Recently, Pintilie et al.[11] reported dielectric measurements on epitaxial PZT films. They concluded that the decrease in the dielectric constant with decreasing film thickness was an artifact of the traditional analysis in terms of a parallel plate capacitor. Moreover, in their analysis, the intrinsic dielectric constant was close to the measured value in fully depleted thin films, and the increase in the dielectric constant with increasing film thickness was attributed to a leaky bulk region of the film.

Furthermore, the ferroelectric properties of PZT are known to vary with cation stoichiometry. For instance, the Curie temperature[12] and remanent polarization[13,14] have both been found to decrease with decreasing Pb content. With the use of Pb-enriched sources, however, it is possible to grow near stoichiometric PZT thin films.[15–20]

In this paper we investigate the influence of film thickness on the crystalline and dielectric properties of rf-magnetron sputter deposited $PbTiO_3$ (PTO) thin films. The growth temperature dependence of the cation stoichiometry and the consequences for the crystalline quality and dielectric properties are also assessed.

a)Electronic mail: thomas.tybell@iet.ntnu.no

II. EXPERIMENTAL DETAILS

A. Sample growth

The samples investigated in this study were grown on (i) insulating $SrTiO_3$ (STO) substrates, (ii) conductive Nb-doped (0.5 wt.%) $SrTiO_3$ (Nb:STO) substrates, and (iii) $SrRuO_3$ (SRO) films deposited in-situ on STO substrates. All substrates were (001) oriented, with a miscut angle of less than 0.1°. Commercially available annealed (Nb:STO), or HF-etched and annealed (STO) substrates were used.

The PTO films were grown by off-axis rf-magnetron sputtering from a non-stoichiometric target with 10% excess Pb. All samples were grown with an $Ar:O_2$ ratio of 10:4 and a total pressure of 165 mTorr. The sputtering power was 90 W, which gave a growth rate of $\sim$ 0.2 nm/min. The samples were allowed to cool to room temperature in the growth ambient.

In order to study the impact of film thickness on the structural and dielectric properties, films with thicknesses ranging from 2.4 to 200 nm were grown. Two sets of PTO films were grown at substrate heater temperatures of 725 and 735 °C, respectively. To study the effect of growth temperature on the crystalline and dielectric properties, films with a thickness of 20 nm, sufficiently thick to display bulk-like crystalline properties, were grown at substrate heater temperatures from 700–760 °C.[21]

The SRO layer was grown with an $Ar:O_2$ ratio of 10:4, a total pressure of 100 mTorr, and a sputtering power of 100 W. The layer thickness was 65 nm with a resistivity of $\sim$ 500 $\mu\Omega$ cm. For measurements of the dielectric properties, circular Au/Pt contact pads with a diameter of 0.4 mm were deposited by e-beam evaporation through a stencil mask. The Nb:STO substrates and SRO films were used as bottom electrodes for the electrical characterization.

B. Structural characterization

The crystalline structure of the thin films was investigated with x-ray diffraction (XRD) using Cu Kα (λ = 0.15406 nm) radiation. The out-of-plane lattice constant and the film thickness were estimated from graphical comparisons of experimental and calculated diffraction patterns of the (001) and (002) diffraction peaks. The diffraction patterns were calculated from an idealized structure of N_{PTO} unit cells of PTO and N_{SRO} unit cells of SRO on a semi-infinite STO substrate.[22] The structure factor for PTO was calculated from the bulk structure,[23] but with the in-plane a-axis lattice constant set equal to the STO substrate value[23] (0.3905 nm) and the out-of-plane c-axis lattice constant used as a fitting parameter. The Ti and O displacements were scaled with the c-axis lattice constant. It has been shown that thin films of SRO grown on STO are compressively strained.[24] Taking into account the resulting expansion of the bulk orthorhombic unit cell in the out-of-plane (110) direction, a simplified tetragonal structure with one f.u./unit cell was used in the structure factor calculations for SRO. The in-plane lattice constant was set equal to the substrate value and the out-of-plane lattice constant used as a fitting parameter, as was done for the PTO structure factor.

To evaluate the crystalline quality of the PTO films, rocking curves were measured around the (001) and (002) diffraction peaks. In-plane coherence with the substrate was assessed from reciprocal space maps (RSM) of the (103) diffraction peak and pole figures of the (103) STO and (113) PTO diffraction peaks. The pole figures were measured with a 2θ angle corresponding to the (113) PTO peak ($\sim$ 77.0°), which is close to the (103) STO peak (2θ = 77.2°). The sample was rotated around the surface normal (the ϕ angle) and about an axis perpendicular to the surface normal (the θ angle).

The relative Pb:Ti ratio was measured with x-ray photoelectron spectroscopy (XPS). The recorded spectra were smoothed with a Sawitzky-Golay filter (11 points, fourth order) and fitted to Voigt functions and a Shirley background using a least squares algorithm. The relative integrated intensities of the XPS peaks were estimated from the fitted curves.

C. Dielectric characterization

Dielectric properties were measured with an Aixacct TF analyzer 2000. The capacitance was measured at 2 kHz with a bias voltage of ±0.1 V and small signal amplitude of 50 mV. The reported capacitances are average values over the bias range. The polarization was measured using a variant of the built-in dynamic hysteresis measurement procedure by the TF analyzer 2000.[25] Asymmetric triangular bipolar voltage pulses were used instead of the standard symmetric pulses to avoid large leakage currents at negative bias without decreasing the polarization field for positive bias. Four pulses were applied, the first two pulses starting with negative half-periods and the final two pulses starting with positive half-periods. The positive half-period of the second pulse and the negative half-period of the fourth pulse were used to calculate the polarization. The pulse length was 1 ms with a dwell time of 2 ms between pulses. The positive and negative amplitudes were set independently, keeping a constant slew rate for the pulse. The polarization was calculated by integrating the measured current, including possible contributions from the leakage current. The voltage was defined as positive when applied to the top electrode.

III. RESULTS AND DISCUSSION

A. Influence of film thickness

1. Crystalline properties

Figure 1 shows typical XRD scans measured around the (001) diffraction peak along with calculated scans for the idealized structure. The PTO film thicknesses were (from bottom to top) 7, 14, 24, and 41 nm, respectively. Thickness fringes around the (001) and (002) diffraction peaks could be readily observed in all but the thickest samples (> 100 nm).

The *c*-axis lattice constant is plotted versus film thickness in Fig. 2. Four different sample series are shown: films grown on insulating STO substrates, films grown on conductive Nb:STO substrates, films grown on SRO films at a nominal temperature of 725 °C, and films grown on SRO films at a nominal temperature of 735 °C. As can be seen, for films thicker than 20 nm the lattice constant is close to the bulk value of 0.4152 nm.[23] Thinner films show a gradual decrease in the lattice constant that is in agreement with the previous reports, wherein this decrease was attributed to a reduction of the spontaneous polarization in thin films.[26] Transmission electron microscopy (TEM) images have shown a strained layer with a decreased *c*-axis lattice constant near the film/substrate interface,[27] recently observed also in PZT films for which a similar decrease in lattice constant was found at the film/vacuum interface as well.[28] To a certain extent, the reduced *c*-axis lattice constant for very thin films, as measured with XRD, will be due to a growing contribution from the smaller *c*-axis lattice constant near the interfaces.

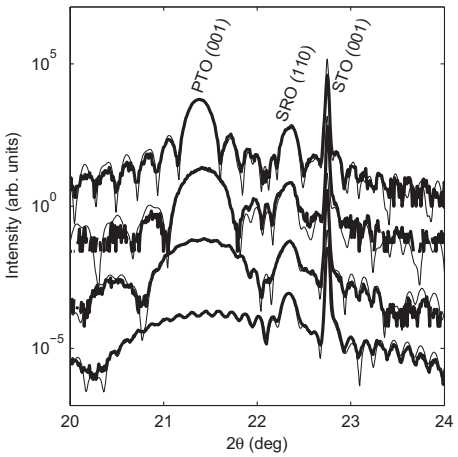

FIG. 1. $\theta/2\theta$ XRD scans of PTO grown on SRO/STO. The PTO film thickness was (from bottom to top) 7, 14, 24, and 41 nm, respectively. The diffractograms have been displaced along the intensity axis for clarity. Bold lines show measured data, while the fine lines are fits obtained from the idealized structure.

The full width at half maximum (FWHM) of rocking curves measured around the (001) PTO diffraction peak was typically twice that of the substrate, and less than 0.04°. In-plane epitaxy was maintained irrespective of thickness. The pole figure of the (113) PTO and (103) STO

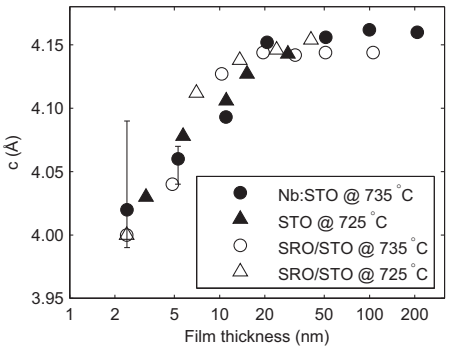

FIG. 2. The PTO c-axis lattice constant, as obtained from fits to the XRD data, plotted vs. film thickness. Films thicker than 20 nm show a fixed out-of-plane lattice constant, similar to the bulk value, while thinner films show a lattice constant which decreases monotonically with the film thickness. No significant difference is seen for films deposited on different substrates or grown at different substrate temperatures. The error bars, shown for films grown on Nb:STO substrates only, indicate the uncertainty in the fitted values. For films thicker than 10 nm the errorbars are smaller than the symbols.

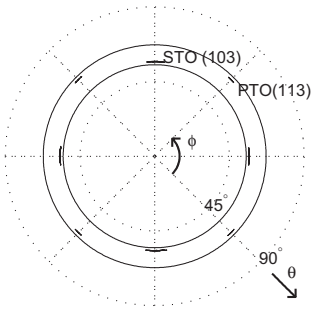

FIG. 3. Pole figure of the (113) PTO and (103) STO diffraction peaks for a 49 nm thick sample grown on SRO/STO. The solid circles identify the region of measurement. The (113) PTO peaks appear at 45° with respect to the (103) STO peaks, which testifies to the cube on cube epitaxy.

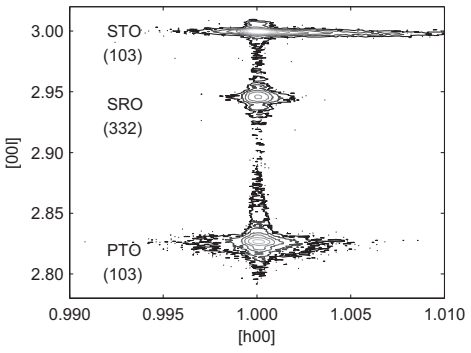

FIG. 4. Reciprocal space map of (103) diffraction peaks for a 100 nm thick PTO film grown on SRO/STO. The PTO, SRO, and STO peaks all have the same in-plane lattice constant.

diffraction peaks in Fig. 3, for a 49 nm thick film grown on SRO/STO, shows the alignment of the in-plane lattice vectors of PTO and STO. The (113) PTO diffraction peaks appear at 45° with respect to the (103) STO diffraction peaks, which testifies to the cube on cube epitaxy. The reciprocal space map of the (103) diffraction peak from a thick PTO film (100 nm) grown on SRO/STO, shown in Fig. 4, shows that the in-plane lattice constants of SRO and PTO are both constrained to the substrate value.

Atomic force microscopy (AFM) imaging showed surfaces with a step-and-terrace structure that gradually disappears with increasing film thickness. The root-mean-square (rms) roughness on 5×5 μm^2 scans was measured at 0.2–0.9 nm. The change from a step-and-terrace structure to a homogeneous flat surface is illustrated in Fig. 5. The step and terrace structure is clearly seen for the thinner films, i.e. for (a) 5 nm, (b) 19 nm, and (c) 32 nm thick films. It degrades in the thicker films, (d) 41 nm and (e) 51 nm, and disappears entirely in (f) a 106 nm thick film. This trend was seen for films grown on both STO, Nb:STO, and SRO.

2. Dielectric properties

The measured capacitance of the Pt/PTO/SRO and Pt/PTO/Nb:STO structures is shown as a function of PTO film

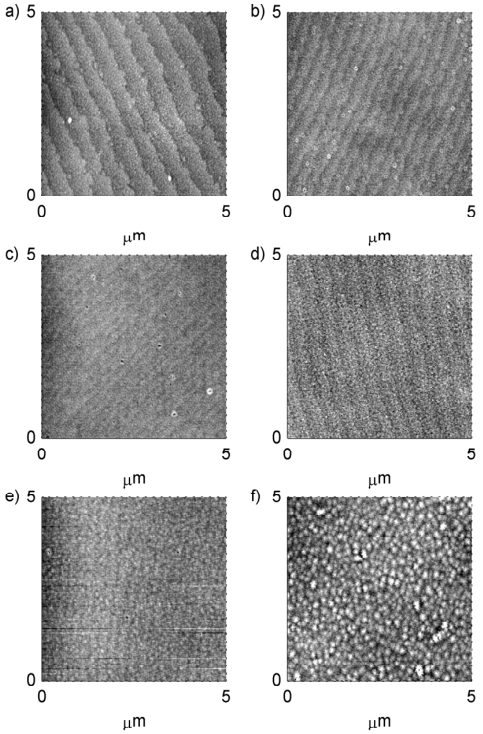

FIG. 5. AFM images of PTO films grown on SRO/STO. The film thickness was a) 5 nm, b) 19 nm, c) 32 nm, d) 41 nm, e) 51 nm, and f) 106 nm. The z-range of the linear gray-scale is ± 1 nm for all images. Clear step-and-terrace structures are observed for the thinnest films, gradually disappearing for thicker films.

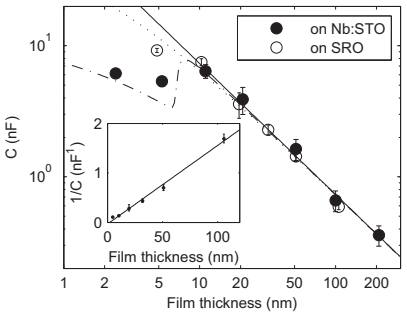

FIG. 6. Measured capacitance of Pt/PTO/Nb:STO capacitors (filled circles) and Pt/PTO/SRO capacitors (open circles) with 0.12 mm^2 area. The error bars are the standard deviations of measurements on different capacitors. The solid line is a fit to the data for films thicker than 10 nm, imposing an inverse thickness dependence. The dotted line is the capacitance calculated for an MIM model and the dash-dotted line is the capacitance calculated for an MIS model. The inset shows the inverse capacitance for films with an SRO bottom electrode vs. film thickness. The linear fit gives a negative intercept corresponding to -3.9 ± 8.1 m^2/F.

thickness in Fig. 6. For film thicknesses greater than 10 nm, the capacitance is proportional to the inverse thickness. In thinner films, a deviation from the inverse thickness dependence is seen for films grown with a SRO bottom electrode. Leakage currents prohibited measurements on films thinner than 4.5 nm. For films grown on a Nb:STO bottom electrode, the capacitance saturates at ~ 5 nF for thin films. A dielectric constant of $\epsilon_{\rm PTO}/\epsilon_0 = 69$ was found from a fit to a linear thickness dependence of the inverse capacitance. For films with a Nb:STO bottom electrode, the fit was limited to films thicker than 10 nm. The clamped and free dielectric constants for PTO are 51 and 126, respectively, in single crystals.[23]

It is known that field penetration into the electrodes will decrease the total capacitance of thin films.[4,5] With two metal electrodes, the total inverse capacitance per unit area for a film of thickness d, is

$$\frac{1}{C} = \left(\frac{\lambda_{\rm Pt}}{\epsilon_{\rm Pt}} + \frac{d}{\epsilon_{\rm PTO}} + \frac{\lambda_{\rm SRO}}{\epsilon_{\rm SRO}} \right), \qquad (1)$$

where $\lambda_{\rm Pt}$ and $\lambda_{\rm SRO}$ are free electron gas screening lengths for Pt and SRO in a linear dielectric background with dielectric constants $\epsilon_{\rm Pt}$ and $\epsilon_{\rm SRO}$, respectively.[5,29] The screening lengths were estimated at $\lambda_{\rm Pt} = 0.06$ nm and $\lambda_{\rm SRO} = 0.11$ nm.[30] With these values, the expected series capacitance from the metal electrodes is 0.47 F/m^2. A fit to a linear thickness dependence of the inverse capacitance for films on SRO, shown in the inset to fig. 6, actually gives a negative intercept of -3.90 ± 8.09 m^2/F. The negative intercept can be interpreted in terms of an electrically short-circuited region of thickness ~ 2 nm in the films. However, the

upper limit of 4.2 m^2/F gives a minimum experimental interface capacitance of 0.24 F/m^2, which can be interpreted in terms of an additional interface capacitance. Based on the estimated electrode capacitance, we find that any additional interface capacitance must be at least 0.48 F/m^2. The interface layers with strain normal to the interface, which were observed by TEM, could have a different dielectric constant from the bulk of the film, giving an additional interface capacitance. The capacitance from these strained layers can be expressed as

$$\frac{1}{C_{\text{inter}}} = d_{\text{inter}} \left(\frac{1}{\epsilon_{\text{inter}}} - \frac{1}{\epsilon_{\text{PTO}}} \right), \qquad (2)$$

where d_{inter} and ϵ_{inter} are the total width and dielectric constant of the strained layers respectively. Assuming that the strained layer width at both the SRO and Pt interface is ~ 1.8 nm, as was observed for an Nb:STO interface,[27] the dielectric constant in the strained layer do not decrease by more than 25% of the bulk value.

For films grown on Nb:STO, the total capacitance can be estimated from a metal-insulator-semiconductor (MIS) model,[31] including the field-dependent dielectric constant of STO.[32,33] The capacitance of the semiconductor surface is found following the analysis of Schottky diodes with field-dependent dielectric constants by Kahng and Wemple.[34] Treating the Nb:STO substrate as a non-degenerate semiconductor with bulk electron and hole densities n_0 and p_0, the surface capacitance is found in the Appendix to be

$$C_s = -qn_0 \frac{\frac{p_0}{n_0}\left(e^{-\beta\phi_s} - 1\right) - \left(e^{\beta\phi_s} - 1\right)}{E_s(\phi_s)}, \quad (3)$$

where q is the absolute value of the electron charge, $\beta = q/k_B T$ with k_B Boltzmann's constant and T the absolute temperature, and $E_s(\phi_s)$ and ϕ_s are the electric field and potential at the semiconductor/insulator interface, respectively. The potential is referenced to the bulk of the semiconductor. The interface potential will depend on the insulator thickness and the polarization, and is found numerically as described in the Appendix. With the small deviation of the dielectric constant in the strained interface layers, found for films with an SRO bottom electrode, the effect on the measured capacitance can be neglected. The total capacitance then is

$$\frac{1}{C} = \left(\frac{\lambda_{\text{Pt}}}{\epsilon_{\text{Pt}}} + \frac{d}{\epsilon_{\text{PTO}}} + \frac{1}{C_s} \right). \qquad (4)$$

The result from the numerical calculations is shown as the dot-dash line in Fig. 6. It was assumed that the work function for Pt is $q\Phi_m = 5.5$ eV,[35] the electron affinity for STO is $q\chi_s = 4.0$ eV,[36] the bandgap of STO is $E_g = 3.2$ eV,[37] and the electron effective mass in STO is $m^*/m_e = 10$.[38] The bulk electron density was assumed equal to the donor density $N_d = 2 \times 10^{20}$ cm^{-3} in the Nb:STO substrate, in accordance with carrier densities derived from transport measurements on similar substrates.[39] The polarization in the PTO film was assumed to be -65 $\mu C/cm^2$, the direction in agreement with our pyroelectric measurements, and the magnitude in reasonable agreement with the polarization measurements. As can be seen, the predicted capacitance is close to the ideal parallel plate value for thick films and significantly reduced for films thinner than ~ 10 nm. For thick films, the large negative polarization induces an inversion layer in the substrate surface, giving a large series capacitance. In thinner films, the potential difference of the electrodes opposes the formation of the inversion layer, and the small depletion layer capacitance dominates the total capacitance.

The film thickness at which this transition occurs can be estimated from a simplified model. Ignoring the free carrier density in depletion and weak inversion, the potential at the interface is[33]

$$\phi_s = -\frac{\sqrt{a}b\epsilon_0}{qN_d} \left[\cosh\left(\frac{qN_d}{b\epsilon_0} w \right) - 1 \right], \qquad (5)$$

where $a = 1.64 \times 10^{15}$ $(V/m)^2$, $b = 1.42 \times 10^{10}$ (V/m), and w is the depletion layer width. Furthermore, $\phi_s = -E_g/q$ at strong inversion, so the depletion width is

$$w_c = \frac{b\epsilon_0}{qN_d} \text{arcosh}\left(\frac{N_d E_g}{\sqrt{a}b\epsilon_0} + 1 \right). \qquad (6)$$

The transition occurs for the film thickness where the depletion layer just reaches this width, and this film thickness is found from the continuity of the displacement field at the interface as

$$d_c = \frac{\epsilon_i(\Phi_m - \chi_s - E_g/q - \frac{qN_d\lambda_{\text{Pt}}}{\epsilon_{\text{Pt}}} w_c)}{P_r + qN_d w_c}. \quad (7)$$

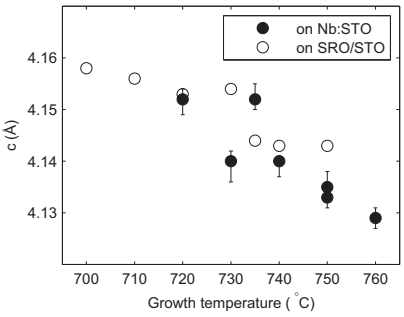

FIG. 7. The c-axis lattice constant for 20 nm thick films grown on Nb:STO (filled circles) and SRO (open circles) as a function of growth temperature. The error bars, shown for films grown on Nb:STO substrates only, indicate the uncertainty in the fitted values.

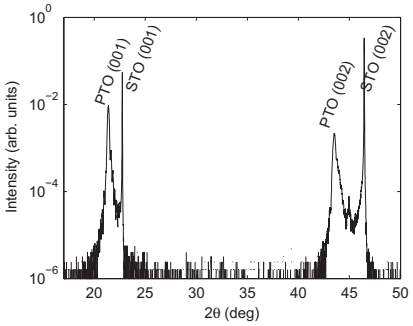

FIG. 8. $\theta/2\theta$ scan of a 53 nm thick PTO film grown on Nb:STO substrate at 735 °C. The $(00l)$ peaks from PTO and STO is seen along with an unidentified impurity phase at $2\theta \sim 45°$.

This thickness depends critically on the polarization. For a polarization between $-60\ \mu C/cm^2$ and $-70\ \mu C/cm^2$, which are plausible values for PTO, the critical thickness varies from 10 to 5 nm, in agreement with the experimental data.

B. Influence of growth temperature

1. Crystalline properties

The c-axis lattice constant was found to decrease with increasing growth temperature. Figure 7 shows a similar decrease for films grown on both Nb:STO and SRO. RSMs of the (103) diffraction peak showed no relaxation of the in-plane lattice constant, regardless of the growth temperature. Furthermore, the crystalline quality, as judged by the FWHM of the (001) rocking curve (less than 0.03°), was unaffected by the growth temperature. Figure 8 shows a $\theta/2\theta$-scan of a 53 nm thick film grown on Nb:STO at 735 °C. The predominant peaks in this diffractogram are the PTO and STO $(00l)$ diffraction peaks. In addition, a minor diffraction peak at $2\theta = 45°$ is attributed to an unidentified impurity phase. This peak was found in diffractograms recorded for 20 nm thick samples as well. The relative peak intensity of the impurity phase to the PTO (002) diffraction peak did not change with the growth temperature or with film thickness, suggesting that the volume fraction of the impurity phase is constant. The PTO film surfaces were flat, with a step and terrace structure. Rms values for the roughness, measured by AFM on $5\times5\ \mu m^2$ scans, varied from 0.2 to 0.7 nm.

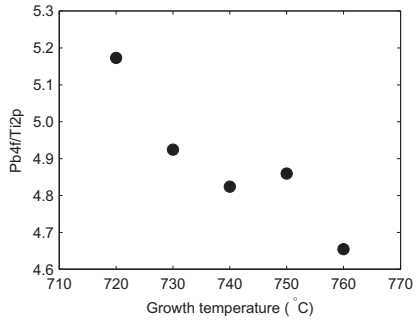

FIG. 9. Peak intensity ratio of the Pb 4f and Ti 2p emission from XPS measurements on PTO films on Nb:STO substrates, as a function of growth temperature. The relative Pb content is seen to decrease with increasing temperature.

Quantitative XPS measurements of the Pb *4f* and Ti *2p* emission showed that the growth temperature affects the material composition. Figure 9 shows the Pb:Ti intensity ratio from measurements made on films grown on Nb:STO. It appears that the Pb:Ti ratio de-

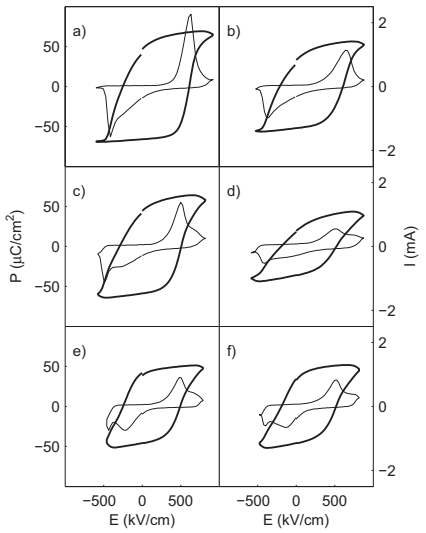

FIG. 10. Hysteresis loops (thick lines) and switching currents (thin lines) measured on PTO films with SRO bottom electrodes. The film growth temperature was a) 700 °C, b) 710 °C, c) 720 °C, d) 730 °C, e) 740 °C, and f) 750 °C.

creases with increasing growth temperature. The concomitant decrease of the lattice constant is consistent with earlier reports.[12,40]

2. Dielectric properties

Capacitance measurements on PTO films with SRO bottom electrodes gave a relative dielectric constant of 91 ± 13, independent of the growth temperature, and in agreement with the dielectric constant found for the thickness series. The films were ferroelectric irrespective of the growth temperature. Polarization hysteresis loops are shown in Fig. 10, together with the switching currents. All samples showed asymmetric hysteresis loops shifted towards a positive field. The maximum applied field was limited by an exponentially increasing leakage current with applied bias voltage. For a negative bias, this limiting field was 440–600 kV/cm, while positive bias permitted an applied field of 780–930 kV/cm. The negative field limit was found to decrease with increasing growth

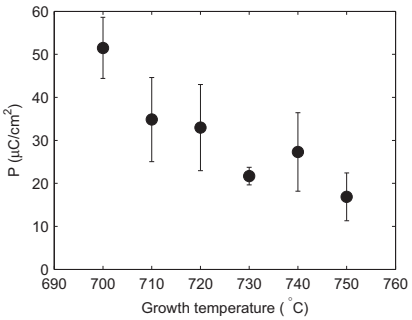

FIG. 11. Switchable polarization as a function of film growth temperature. A marked decrease of the polarization is seen with increasing growth temperature. The error bars are the standard deviations of measurements on different capacitors.

temperature. These upper and lower bounds on the bias voltage lead to unsaturated polarization loops. Samples grown at low temperatures, 700 °C (a) and 710 °C (b), showed a saturated polarization for negative fields and unsaturated polarization for positive fields. At higher growth temperatures the polarization is unsaturated for both positive and negative fields. Moreover, the switching currents decreased in amplitude for samples grown at high temperatures. It remains unclear whether this is due to unsaturated polarization or derives from a decrease in spontaneous polarization.

The switchable polarization, defined as half the sum of the negative and positive polarization at zero field, is shown as a function of growth temperature in Fig. 11. Averaged over 3–6 contacts on each sample, the polarization varied from 51 ± 7 μC/cm^2 for a sample grown at 700 °C to 17 ± 6 μC/cm^2 for a sample grown at 750 °C. These polarization values are smaller than that estimated from the capacitance measurements on films with Nb:STO electrodes. This is attributed to the difference between the remanent polarization and the switchable polarization. For these unsaturated hysteresis loops, the switchable polarization can be less than the actual remanent polarization in the initial negative polarization state. The coercive field, defined as half the sum of the applied field at the switching current peaks, also decreased with growth temperature, from 474 ± 35

to 366±55 kV/cm. The increase in leakage current with increasing growth temperature, which in PTO is often associated with Pb vacancies,[41] is in agreement with the decreasing Pb content found from the XPS data.

IV. CONCLUSIONS

Good quality PTO films were grown with thicknesses from 2 to 200 nm. The crystalline quality was unaffected by the growth temperature from 700 to 760 °C. Films grown at high temperature appeared to be Pb deficient, as seen from unsaturated hysteresis loops, a reduced *c*-axis lattice constant, and a reduced Pb *4f* to Ti *2p* intensity ratio in XPS measurements.

Capacitance measurements were consistent with a thickness independent dielectric constant. The dielectric constant in the strained layer at the film/substrate interface previously observed in TEM images, is not reduced by more than 25% compared with the bulk of the film.

ACKNOWLEDGMENTS

T. T. acknowledges support from the Research council of Norway under grant #162874/V00.

Appendix

The potential, ϕ_s, at the semiconductor/insulator interface in the MIS model is found numerically from the continuity of the displacement field,

$$\epsilon_i E_i(\phi_s) + P_r = D_s(\phi_s), \tag{A.1}$$

where ϵ_i is the linear dielectric constant of the insulator, $E_i(\phi_s)$ the electric field in the insulator (which, under the assumption of no free charge, is constant throughout the film), P_r the remanent polarization in the insulator, and $D_s(\phi_s)$ is the displacement field in the semiconductor at the interface. The electric field in the insulator is

$$E_i(\phi_s) = -\frac{1}{d}\left[\Phi_m - \chi_s - \phi_m(\phi_s) + \phi_s\right], \tag{A.2}$$

where d is the insulator thickness, $q\Phi_m$ the metal work function, $q\chi_s$ the semiconductor electron affinity, and $\phi_m(\phi_s)$ the potential at the metal-insulator interface referenced to the bulk of the semiconductor. It is assumed that the electron affinity is equal to the semiconductor work function. With an applied voltage V,

$$\phi_m(\phi_s) = -\frac{\lambda_m}{\epsilon_m} D_s(\phi_s) + V, \tag{A.3}$$

where λ_m is the screening length and ϵ_m the dielectric constant of the metal. With the field-dependent dielectric constant of Nb:STO as found by Yamamoto et al.[33]

$$\epsilon_{\mathrm{STO}}(E) = \frac{b\epsilon_0}{\sqrt{a + E^2}}, \tag{A.4}$$

where the constants a and b are 1.64×10^{15} $(\mathrm{V/m})^2$ and 1.42×10^{10} V/m, respectively, the displacement field at the interface is

$$\begin{aligned} D_s(\phi_s) &= \int_0^{E_s} \epsilon_{\mathrm{STO}} dE \\ &= b\epsilon_0 \ln\left(\frac{E_s + \sqrt{a + E_s^2}}{\sqrt{a}}\right), \end{aligned} \tag{A.5}$$

where $E_s = E_s(\phi_s)$ is the electric field in the semiconductor at the interface. The electric field is found using the standard textbook derivation,[31] assuming non-degenerate carrier statistics, but allowing for a field dependent dielectric constant. The electric field is found as

$$\begin{aligned} E_s(\phi) = \pm\Bigg[&\frac{1}{b^2}\left(\frac{k_B T}{qL_0}\right)^4 F^4(\phi) \\ &+ 2\frac{\sqrt{a}}{b}\left(\frac{k_B T}{qL_0}\right)^2 F^2(\phi)\Bigg]^{1/2} \end{aligned} \tag{A.6}$$

The field is positive for positive ϕ and negative when ϕ is negative. The Debye-type length L_0 and the function $F(\phi)$ are[31]

$$L_0 = \sqrt{\frac{\epsilon_0}{q n_0 \beta}}, \tag{A.7}$$

and

$$\begin{aligned} F^2(\phi) = \frac{p_0}{n_0}&\left(e^{-\beta\phi} + \beta\phi - 1\right) \\ &+ \left(e^{\beta\phi} - \beta\phi - 1\right). \end{aligned} \tag{A.8}$$

The assumption of non-degenerate carrier statistics for the 0.5 wt.% Nb doped STO substrates is generally not applicable. However, the major effect of the film thickness and polarization dependence of the surface capacitance is from the depletion region, where the carrier density is described by non-degenerate statistics.

The capacitance of the surface layer is $C_s = \partial D_s/\partial\phi_s$, and is found from the the displacement field expressed as a function of surface potential ϕ_s,

$$D_s(\phi_s) = -qn_0 \int_0^{\phi_s} \left[\frac{p_0}{n_0} \left(e^{-\beta\phi} - 1\right) - \left(e^{\beta\phi} - 1\right) \right] E^{-1}(\phi) d\phi. \quad \text{(A.9)}$$

Thus the capacitance is

$$C_s = \frac{\partial D_s}{\partial \phi_s} = -qn_0 \frac{\frac{p_0}{n_0}\left(e^{-\beta\phi_s} - 1\right) - \left(e^{\beta\phi_s} - 1\right)}{E_s(\phi_s)}. \quad \text{(A.10)}$$

The flat-band capacitance is found from an expansion of the charge density and electric field for small ϕ_s to be

$$\lim_{\phi_s \to 0} C_s = \frac{qn_0\sqrt{\frac{p_0}{n_0} + 1}}{\sqrt{\frac{\sqrt{a}}{b}}\left(\frac{k_B T}{qL_0}\right)}. \quad \text{(A.11)}$$

[1] T. M. Shaw, S. Trolier-McKinstry, and P. C. McIntyre, Annu. Rev. Mater. Sci. **30**, 263 (2000).
[2] C. Zhou and D. M. Newns, J. Appl. Phys. **82**, 3081 (1997).
[3] K. Natori, D. Otani, and N. Sano, Appl. Phys. Lett. **73**, 632 (1998).
[4] O. K. Rice, Phys. Rev. **31**, 1051 (1928).
[5] H. Y. Ku and F. G. Ullman, J. Appl. Phys. **35**, 265 (1964).
[6] T. Nakagawa, J. Yamaguchi, T. Usuki, Y. Matsui, M. Okuyama, and Y. Hamakawa, Jpn. J. Appl. Phys. **18**, 897 (1979).
[7] Y. Sakashita, H. Segawa, K. Tominaga, and M. Okada, J. Appl. Phys. **73**, 7857 (1993).
[8] K. Amanuma, T. Mori, T. Hase, T. Sakuma, A. Ochi, and Y. Miyasaka, Jpn. J. Appl. Phys., Part 1 **32**, 4150 (1993).
[9] P. K. Larsen, G. J. M. Dormans, D. J. Taylor, and P. J. van Veldhoven, J. Appl. Phys. **76**, 2405 (1994).
[10] H. Fujisawa, S. Nakashima, K. Kaibara, M. Shimizu, and H. Niu, Jpn. J. Appl. Phys., Part 1 **38**, 5392 (1999).
[11] L. Pintilie, I. Vrejoiu, D. Hesse, G. LeRhun, and M. Alexe, Phys. Rev. B **75**, 224113 (2007).
[12] S.-i. Shirasaki, Solid State Commun. **9**, 1217 (1971).
[13] T. Mihara and H. Watanabe, Jpn. J. Appl. Phys., Part 1 **34**, 5674 (1995).
[14] S. Aggarwal, S. Madhukar, B. Nagaraj, I. G. Jenkins, R. Ramesh, L. Boyer, and J. T. Evans, Jr., Appl. Phys. Lett. **75**, 716 (1999).
[15] K. Iijima, Y. Tomita, R. Takayama, and I. Ueda, J. Appl. Phys. **60**, 361 (1986).
[16] S. Ueno and H. Ishiwara, Jpn. J. Appl. Phys., Part 1 **31**, 2982 (1992).
[17] G. J. M. Dormans, P. J. van Veldhoven, and M. de Keijser, J. Cryst. Growth **123**, 537 (1992).
[18] J. F. M. Cillessen, M. W. J. Prins, and R. M. Wolf, J. Appl. Phys. **81**, 2777 (1997).
[19] G. Velu and D. Remiens, Vacuum **56**, 199 (2000).
[20] S. Aggarwal, K. R. Udayakumar, and J. A. Rodriguez, J. Appl. Phys. **100**, 064103 (2006).
[21] The substrate temperature, measured with an optical pyrometer at 1.55 μm, using an emissivity of 0.7, was 530–565 °C and 510–545 °C, as measured on Nb:STO and SRO substrates respectively.
[22] C. Thompson, C. M. Foster, J. A. Eastman, and G. B. Stephenson, Appl. Phys. Lett. **71**, 3516 (1997).
[23] M. Adachi, J. Harada, T. Ikeda, S. Nomura, E. Sawaguchi, and T. Yamada, in *Group III: Crystal and Solid State Physics*, Landolt-Börnstein, New Series, Vol. 16, edited by K.-H. Hellwege and A. M. Hellwege (Springer-Verlag, Berlin-Heidelberg, 1981).
[24] C. B. Eom, R. J. Cava, R. M. Fleming, J. M. Phillips, R. B. van Dover, J. H. Marshall, J. W. P. Hsu, J. J. Krajewski, and W. F. Peck, Jr., Science **258**, 1766 (1992).
[25] The standard procedure is described in the *TF analyzer 2000 FE-module user manual* (aixACCT Systems GmbH, Aachen, Germany). In the standard procedure the positive and negative amplitudes are equal, and the dwell time between pulses is 1 s.
[26] C. Lichtensteiger, J.-M. Triscone, J. Junquera, and P. Ghosez, Phys. Rev. Lett. **94**, 047603 (2005).
[27] A. T. J. van Helvoort, Ø. Dahl, B. G. Soleim, R. Holmestad, and T. Tybell, Appl. Phys. Lett. **86**, 092907 (2005).
[28] V. Nagarajan, J. Junquera, J. Q. He, C. L. Jia, R. Waser, K. Lee, Y. K. Kim, S. Baik, T. Zhao, R. Ramesh, P. Ghosez, and K. M. Rabe, J. Appl. Phys. **100**, 051609 (2006).
[29] R. R. Mehta, B. D. Silverman, and J. T. Jacobs, J. Appl. Phys. **44**, 3379 (1973).
[30] The sreening lengths were estimated from a carrier density for Pt of 6.6×10^{23} cm^{-3}, based on the lattice constant (Ref. 42) and assuming 10 conduction electrons per atom, and litterature values of the carrier density for SRO (Ref. 43) of 1.22×10^{22} cm^{-3}, electron effective masses $m^*/m_e = 5$ for Pt and $m^*/m_e = 4$ for SRO (Refs. 44 and 45), lattice dielectric constant $\epsilon_{\mathrm{SRO}}/\epsilon_0 = 8.45$ for SRO (Ref. 46), and an assumed lattice dielectric constant of $\epsilon_{\mathrm{Pt}}/\epsilon_0 = 10$ for Pt.

[31] S. M. Sze, *Physics of Semiconductor Devices*, 2nd ed. (Wiley, New York, 1981).
[32] R. A. van der Berg, P. W. M. Blom, J. F. M. Cillessen, and R. M. Wolf, Appl. Phys. Lett. **66**, 697 (1995).
[33] T. Yamamoto, S. Suzuki, H. Suzuki, K. Kawaguchi, K. Takahashi, and Y. Yoshisato, Jpn. J. Appl. Phys., Part 2 **36**, L390 (1997).
[34] D. Kahng and S. H. Wemple, J. Appl. Phys. **36**, 2925 (1965).
[35] A. Goldmann, in *Group III: Condensed Matter*, Landolt-Börnstein, New Series, Vol. 23, edited by W. Martienssen (Springer-Verlag, Berlin, 2003).
[36] R. A. Powell and W. E. Spicer, Phys. Rev. B **13**, 2601 (1976).
[37] J. A. Noland, Phys. Rev. **94**, 724 (1954).
[38] H. P. R. Frederikse, W. R. Thurber, and W. R. Hosler, Phys. Rev. **134**, A442 (1964).
[39] H. P. R. Frederikse and W. R. Hosler, Phys. Rev. **161**, 822 (1967).
[40] C. D. Theis and D. G. Schlom, J. Cryst. Growth **174**, 473 (1997).
[41] J. P. Remeika and A. M. Glass, Mater. Res. Bull. **5**, 37 (1970).
[42] W. G. Wyckoff, *Crystal Structures*, 2nd ed., Vol. 1 (Interscience Publishers, New York, 1963).
[43] M. Shepard, S. McCall, G. Cao, and J. E. Crow, J. Appl. Phys. **81**, 4978 (1997).
[44] D. L. Martin, Phys. Rev. B **17**, 1670 (1978).
[45] P. A. Cox, R. G. Egdell, J. B. Goodenough, A. Hamnett, and C. C. Naish, J. Phys. C **16**, 6221 (1983).
[46] D. J. Kim, J. Y. Jo, Y. S. Kim, Y. J. Chang, J. S. Lee, J.-G. Yoon, T. K. Song, and T. W. Noh, Phys. Rev. Lett. **95**, 237602 (2005).

Paper III

Polarization direction and stability in ferroelectric lead titanate thin films

Published in Journal of Applied Physics **106**, 084104 (2009).

Polarization direction and stability in ferroelectric lead titanate thin films

Ø. Dahl,[a] J. K. Grepstad, and T. Tybell[b]
Department of Electronics and Telecommunications, Norwegian University of Science and Technology, O.S. Bragstads plass 2a, NO-7491 Trondheim, Norway

In this article, we examine the initial polarization of $PbTiO_3$ thin films grown epitaxially on $SrRuO_3$ electrodes. It is found that the as-grown predominant polarization is directed towards the $SrRuO_3$ bottom electrode in films thinner than 20 nm, and directed towards the top surface in thicker films. The data is interpreted in terms of a Landau-Ginzburg-Devonshire model for a semiconducting ferroelectric with asymmetric boundary conditions. Based on the measured hysteresis loops and the stability of the two polarization directions with time, it is concluded that charged defects serve to impose a preferential downward polarization in very thin films.

I. INTRODUCTION

Ferroelectric thin films for device applications are often polarized perpendicular to the film surface. Ideally, the polarization is compensated by screening charges in short-circuited electrodes. When such boundary conditions are not satisfied, stable polarization can be explained by internal screening in a Landau-Ginzburg-Devonshire model.[1–3] As was shown by Guro *et al.*,[2] the contact potential of the ferroelectric-electrode interface affects the polarization in the ferroelectric. Hence ferroelectric thin film structures with only one electrode may exhibit a preferred direction of polarization, which is often observed experimentally. For example, ferroelectric $PbTiO_3$ thin films grown on Nb-doped $SrTiO_3$ electrodes were found to be monodomain with positive polarization (i.e., $\vec{P}$ directed towards the substrate),[4] while similar films grown on $SrRuO_3$ electrodes have shown negative polarization.[5] Monodomain films with positive polarization as well as polydomain films with periodically alternating positive and negative domains have been reported for $PbTiO_3$ grown on insulating $SrTiO_3$ substrate.[6–8] In addition to the substrate material, the size of the ferroelectric material has also been found to affect the initial polarization. Inversion of the net polarization upon increasing size was observed for $PbTiO_3$ particles deposited on Nb-doped $SrTiO_3$ substrate, from positive polarization in small particles to negative polarization for particles larger than $\sim 10^5$ nm^3.[9] A similar effect was observed for $PbTiO_3$ thin films grown on $La_{0.67}Sr_{0.33}MnO_3$ electrodes, which changed from a polydomain to a monodomain state with negative polarization when the film thickness exceeded 25 nm.[10] It has also been found that the oxygen pressure under high temperature processing can be used to reversibly switch the polarization in $PbTiO_3$ films with a $SrRuO_3$ bottom electrode.[11] At the moment, it is not established to what extent the polarization is screened by domain formation, external, or internal charges.

Here, we investigate the initial polarization and the stability of the switched polarization in $PbTiO_3$ thin films grown on $SrRuO_3$ electrodes. We use a Landau-Ginzburg-Devonshire model for an ideal semiconducting ferroelectric to theoretically assess the initial polarization, extending the symmetric models of Ivanchik,[1] Guro *et al.*,[2] Chenskii,[3] and Watanabe,[12] with boundary conditions appropriate for a thin film with a vacuum interface on one side and a metallic electrode on the other.

II. EXPERIMENTAL

$PbTiO_3$ films with a thickness ranging from 5 to 100 nm were grown on $SrRuO_3$ epilayers deposited on $SrTiO_3$ substrate. The films

[a] Present address: SINTEF Materials and Chemistry, NO-7465 Trondheim, Norway. Electronic mail: oystein.dahl@sintef.no
[b] Electronic mail: thomas.tybell@iet.ntnu.no

were grown by off-axis rf magnetron sputtering from a $Pb_{1.1}TiO_3$ target in an O_2:Ar (4:10) atmosphere with a total pressure of 165 mTorr at a growth temperature of 540 °C. The films were *c*-axis oriented, with a mosaic spread of < 0.03 deg, as measured by x-ray diffraction rocking curves around the (001) and (002) reflections. The step-and-terrace surface topography of the substrates was replicated for films thinner than 100 nm, while thicker films had a root-mean-square surface roughness of less than 0.4 nm. Further details on film deposition and crystalline structure characterization are reported elsewhere.[13] The $SrRuO_3$ layer was used as bottom electrode, and 0.12 mm^2 Au/Pt contacts (200/50 nm thick) deposited *ex situ* were used as top electrodes for electrical characterization.

Polarization hysteresis curves were measured with a conventional Sawyer-Tower type setup (Aixacct TF2000). Asymmetric triangular bipolar voltage pulses were used, as reported previously,[13] and the measurement frequency was 1 kHz. Pyroelectric hysteresis curves were measured as described by Chynoweth.[14] The samples were locally heated using a 40 mW laser of 830 nm wavelength focused on the top electrode. The laser beam was pulsed using a mechanical chopper, and the resulting pyroelectric current was detected with a phase-locked amplifier. A current-to-voltage converter was used to ensure short-circuit conditions during measurements. The samples were polarized by voltage pulses with a pulse length of 1 s. The dwell time between polarization and measurement of the pyroelectric response was 5 s. Hysteresis loops were mapped out by applying a sequence of pulses with increasing and decreasing voltage amplitude. The stability of the polarization was examined by monitoring the time response of the pyroelectric current after forced polarization. The samples remained short-circuited throughout these measurements.

III. RESULTS AND DISCUSSION

The initial pyroelectric hysteresis loops, measured during the first switching of polarization, are shown in Fig. 1. The 10 nm thick film, Fig. 1 (a), showed a positive initial pyroelectric response, while thicker films such as the 19 nm thick film, Fig. 1 (b), showed a negative initial response. Films thicker than $\sim$ 30 nm, Figs. 1 (c) and (d), showed a negative initial response close to saturation. The response of a 5 nm thick film was consistent with a positive polarization, however, this film could not be switched in the present experiment. The $PbTiO_3$ samples in this study showed a change in net polarization with film thickness, with a positive initial polarization for the thinnest films, thus differing from previous reports which found a negative polarization for all film thicknesses.[5] Polarization hysteresis loops are shown in Fig. 2. Leakage current in samples thinner than $\sim$ 20 nm made polarization measurements by the conventional technique unreliable. The polarization data show a similar trend as the pyroelectric loops, with a less sharp switching voltage for the thinnest samples. This is also evident from the current-voltage data shown by broken curves in Fig. 2.

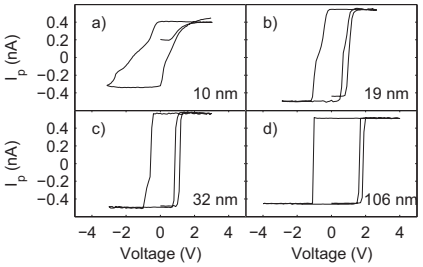

FIG. 1. Pyroelectric hysteresis loops measured on as-grown $PbTiO_3$ films. The initial response is positive in the 10 nm thick sample a), while it is negative in the thicker samples b-d).

The stability of the switched polarization with time is shown in Fig. 3 for a 10 nm and a 19 nm thick film, respectively. The pyroelectric response was found to decline nearly logarithmic with time after polarization. Thick films showed no measurable difference in stability between the two polarization states. Only for very thin films, initially polarized in the positive state, is an asymmetry of the polarization state clearly observed. After the film is negatively polarized, it reverts to a positive polar-

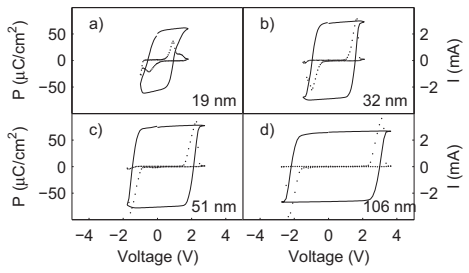

FIG. 2. Polarization hysteresis loops measured on $PbTiO_3$ films. The solid curves are the measured polarization (left ordinate axis), and the broken curves the measured current (right ordinate axis).

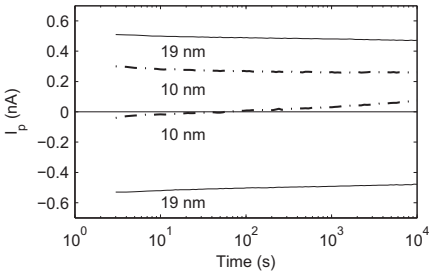

FIG. 3. The measured pyroelectric response vs. time after polarization for two film thicknesses, 19 nm (solid curves) and 10 nm (dashed curves). The 10 nm thick film reverts to a net positive polarization after being switched to a negative state. For thicker films the response is symmetric.

ization.

The predominantly negative initial polarization has been previously attributed to polarization screening by negative ions in the growth chamber.[5] Here, the influence of the electrode configuration on the polarization direction is examined. In a perfectly insulating ferroelectric, the electric field associated with the polarization gradient tends to destabilize the polarization. In a semiconducting ferroelectric, the surface band-bending can induce a screening charge to stabilize the polarization.[1–3]

Following Ivanchik[1] and Guro *et al.*[2], the Landau-Ginzburg-Devonshire expansion of the elastic Gibbs free energy density in the ferroelectric material in terms of the displacement field D,

$$G = G_0 + \frac{K}{2}\left(\frac{dD}{dz}\right)^2 + \frac{A(T)}{2}D^2 + \frac{B}{4}D^4 + \frac{C}{6}D^6, \quad (1)$$

is used to find the equation of state relating the electric field E and the displacement D. The elastic energy is incorporated by rescaling the thermodynamic constants A and B.[15,16] The effect of the the bottom electrode interface and the film surface is included through the boundary conditons and the energy associated with the gradient of the displacement field near the film surface. The thermodynamic constants A, B, and C are known experimentally for $PbTiO_3$,[17] and Zhirnov's estimate for the constant K,[15] assuming that the polarization varies over distances on the order of a lattice constant a_0, is adopted by setting $K = A(0)a_0^2$.[18] The displacement field profile and the charge density are found self-consistently from the equation of state, which gives the electric field as the variational derivative of the elastic Gibbs free energy density,

$$E = \frac{\partial G}{\partial D} - \frac{d}{dz}\left(\frac{\partial G}{\partial \frac{dD}{dz}}\right) = -K\frac{d^2D}{dz^2} + AD + BD^3 + CD^5. \quad (2)$$

The electric field is by definition equal to the negative of the gradient of the electrostatic potential ϕ. Thus,

$$AD + BD^3 + CD^5 = K\frac{d^2D}{dz^2} - \frac{d\phi}{dz}, \quad (3)$$

which by multiplication with the charge density $\rho = dD/dz$ gives

$$(AD + BD^3 + CD^5)dD = \left(K - \frac{d\phi}{d\rho}\right)\rho d\rho. \quad (4)$$

Integrating (4) over the $PbTiO_3$ layer gives

$$\left[\frac{A}{2}D^2 + \frac{B}{4}D^4 + \frac{C}{6}D^6\right]_{D(z_1)}^{D(z_2)} = \frac{K}{2}\left[\rho^2\right]_{\rho(z_1)}^{\rho(z_2)} - \left[\rho\phi\right]_{\rho(z_1)}^{\rho(z_2)} + \int_{\rho(z_1)}^{\rho(z_2)}\phi d\rho, \quad (5)$$

where the solution of the final integral depends on the relation between charge density and electrostatic potential. For a semiconductor, the charge density is

$$\rho = q\left[p - n + N_d^+ - N_a^-\right], \tag{6}$$

where q is the electron charge, n and p are the electron and hole densities, and $q(N_d^+ - N_a^-)$ the net charge density from the dopants. For an intrinsic semiconductor, the Boltzmann approximation gives $\rho(\phi) = 2qn_i \sinh(-\beta\phi)$,[19] where n_i is the intrinsic carrier density.[20] The potential ϕ is measured relative to the chemical potential of the neutral semiconductor and $\beta = q/kT$, where k is Boltzmann's constant and T the absolute temperature. The numerical calculations show that the induced charge density at the surface invalidates the Boltzmann approximation. Therefore, Joyce and Dixon's approximation for the relation between the reduced electrochemical potential $\eta_n = (\mu + q\phi - E_c)/kT$ and the electron density n,[21]

$$\eta_n = \ln\left(\frac{n}{N_c}\right) + \sum_{m=1} A_m \left(\frac{n}{N_c}\right)^m, \tag{7}$$

is used instead of the Boltzmann approximation. Here μ is the chemical potential, E_c is the conduction band edge, and N_c is the conduction band effective density of states. Joyce and Dixon derive the coefficients A_m from a reversion of the power series expansion of the Fermi integral in terms of $\exp(\eta)$.[21] The same approximation is used for the hole density p, with the reduced electrochemical potential replaced by $\eta_p = (E_v - \mu - q\phi)/kT$, where E_v is the valence band edge. N_c is replaced by the valence band effective density of states P_v. In the numerical calculations, the approximation is limited to the first four terms.[22] Setting $d\rho = q(dp - dn)$, the integral in Eq. (5) is written

$$\int_{\rho(z_1)}^{\rho(z_2)} \phi(\rho)d\rho = q\int_{p(z_1)}^{p(z_2)} \phi(\eta_p)dp - q\int_{n(z_1)}^{n(z_2)} \phi(\eta_n)dn. \tag{8}$$

From Eq. (7), relating ϕ and n,

$$\begin{aligned} -q\int \phi dn = & \\ & -\int\left\{kT\left[\ln\left(\frac{n}{N_c}\right) + \sum_m A_m\left(\frac{n}{N_c}\right)^m\right] + (\mu - E_c)\right\}dn \\ & = -n\left\{kT\left[\ln\left(\frac{n}{N_c}\right) - 1 + \sum_m \frac{A_m}{m+1}\left(\frac{n}{N_c}\right)^m\right] + (\mu - E_c)\right\}, \end{aligned} \tag{9}$$

with a corresponding expression for the integral over the hole density. For the numerical calculations, the minority carrier density was estimated from the law of mass action, $(n,p) = n_i^2/(p,n)$. The majority carrier density was found from Eq. (6).

The $PbTiO_3/SrRuO_3$ system is modelled as an ideal semiconducting monodomain ferroelectric with a free electron gas bottom electrode. For this asymmetric configuration, the boundary condition at the surface is

$$D = 0, \tag{10}$$

and the displacement field and potential at the ferroelectric-metal interface are related by

$$\phi = \frac{\lambda}{\epsilon_r \epsilon_0} D - \Delta\Phi, \tag{11}$$

where $\Delta\Phi$ is the contact potential, and λ and ϵ_r are the screening length and the relative dielectric constant of the metallic electrode, respectively.[23] The displacement field will increase from zero at the film surface to an extreme value D_0, either in the interior of the film or at the ferroelectric-metal interface. If the extreme is found in the interior of the film, it follows that the gradient of the displacement field is zero there. Hence, there is a neutral plane where $\rho = 0$ and $\phi = 0$. Equation (5) can then be solved numerically for D in terms of ϕ. If no neutral plane is found, Eq. (5) can be solved with $D = D_0$ at the ferroelectric-metal interface and ϕ given by Eq. (11). The displacement field profile and corresponding film thickness were found by numerical integration

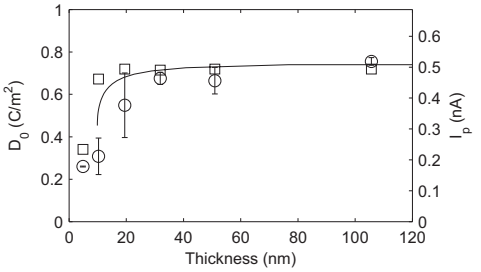

FIG. 4. The relationship between film thickness and displacement field, as obtained from a Landau-Ginzburg-Devonshire model at room temperature (solid line). The open circles mark the experimental initial pyroelectric response (right ordinate axis), and the open squares shows the displacement field calculated from the measured lattice constant (left ordinate axis).

of the inverse charge density over the displacement field, from the film surface to the film-bottom electrode interface.

In Fig. 4, the solid line shows the magnitude of D_0 versus the film thickness for an intrinsic semiconducting ferroelectric with contact potential $\Delta\Phi = -0.3$ V and negative polarization. The contact potential was set equal to $\Phi_m - (\chi_s + V_n)$, where $q\Phi_m$ is the work function of the metal electrode, and $q\chi_s$ and qV_n are the electron affinity and the difference between the conduction band minimum and the chemical potential, respectively.[24] The reported literature values are $\Phi_m = 4.9$ V for $SrRuO_3$ and $\chi_s = 3.5$ V for $PbTiO_3$.[25,26] While some uncertainty is involved in the assessment of the exact value of the chemical potential, equal effective density of states is assumed for the conduction and the valence band, and $V_n = E_g/2q$, with $E_g = 3.4$ eV for $PbTiO_3$.[26] As can be seen, for a film thickness of less than 10 nm, the model has no solution for the displacement field. For films thicker than 10 nm, there is a finite solution for the displacement field, which increases with thickness and saturates for films thicker than 40 nm. Considering only the asymmetry arising from the contact potential at the film-bottom electrode interface, the negative polarization state is about 0.1 J/m^2 lower in energy than the positive polarization state for any film thickness. The free energy density in the infinitely thick film limit is about 1×10^8 J/m^3 lower than the paraelectric reference structure. Thus for a 10 nm thick film, the energy difference between positive and negative polarization amounts to about 10% of the total change in free energy.

Figure 4 also shows experimental data for the magnitude of the initial pyroelectric response (open circles). The measured pyroelectric response is seen to increase less rapidly with increasing film thickness than predicted by the model. The measured pyroelectric response is a surface average over both positive and negative domains. Hence, for thin films where the depolarization field is stronger, resulting in a more even distribution of positive and negative domains, the net response is less than predicted for a monodomain thin film.

It is also possible to relate the polarization to the unit cell tetragonality. From the elastic Gibbs free energy,[17] under the appropriate mechanical boundary conditions,[16] the relation between the out-of plane lattice constant c and the displacement field D reads,

$$D^2 = \frac{1}{Q_{11} - \frac{2s_{12}}{s_{11}+s_{12}}Q_{12}} \left[\frac{c}{a_0} - \left(1 + \frac{2s_{12}}{s_{11}+s_{12}}u_0\right)\right], \quad (12)$$

where a_0 is the cubic lattice constant, u_0 is the in-plane strain imposed by the epitaxial growth on the $SrTiO_3$ substrate, s_{11} and s_{22} are the elastic compliance coefficients, and Q_{11} and Q_{12} are the electrostrictive constants. The displacement field calculated from Eq. (12) with the measured lattice constant c,[13] using values for the electrostrictive coefficients and the cubic lattice constant as given by Haun *et al.*,[17] and elastic compliance coefficients taken from Ref. 27, is shown as open squares in Fig. 4. The calculated displacement field from the measured lattice constant is in good agreement with the predictions from the model and increases more rapidly than the pyroelectric response, again indicating the effect of domain formation for very thin films.

The observed change in stable polarization direction is not predicted by the present model for an intrinsic semiconductor, for which negative polarization is stable for all film thicknesses. We note, that if the chemical poten-

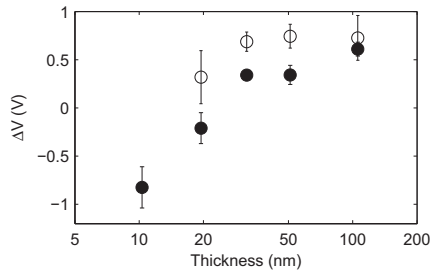

FIG. 5. The measured offset voltage of the pyroelectric (filled circles) and ferroelectric (open circles) hysteresis loops. The voltage offset is negative in thin films, going positive and increasing with film thickness to saturate at ~ 0.5 V.

tial changes as a result of doping, this will have two potentially opposing effects: (i) The contact potential will change. A net donor doping reduces V_n and makes the contact potential less negative, or even positive, potentially stabilizing the positive polarization direction. Whereas a net acceptor doping may help stabilize the negative polarization direction. (ii) The amount of surface band bending required to induce a sufficient screening charge is changed. A net donor doping decreases the screening energy at the surface for the negative polarization direction, while a net acceptor doping decreases the energy for a positive polarization direction. Calculations with net acceptor dopant densities from 10^{-1} to 10^{9} cm^{-3} gave lowest energy for positive polarization in thin films and for negative polarization in thick films, with a crossover thickness in the range of 20–30 nm.

The above analysis does not include the influence of defects. Internal fields can result from charged defects and defect dipoles.[28–33] In Fig. 5, the voltage offset, defined as half the sum of the coercive switching voltages for positive and negative polarization, are shown for pyroelectric (filled circles) and polarization (open circles) hysteresis measurements. The offset voltage for thick films (> 30 nm) corresponds to the built-in offset expected from the difference in work function for the Pt and $SrRuO_3$ electrodes. For thinner films the offset voltage decreases and reaches -0.8 V for the 10 nm thick film. Polarization hysteresis loops from 20 nm thick films grown at different temperatures[13] showed an increasing negative voltage offset for films grown at the highest temperatures. Combined with the spontaneous switching to positive polarization, this suggests an increased influence from defects in the thinnest films. The preferred positive polarization and negative offset voltage in thin films are compatible with positively charged oxygen vacancies at the surface. Additional mechanisms are needed to explain the change in preferred polarization direction with increasing film thickness. A realistic model of the interaction and the dynamics between defects and the polarization during film growth would be valuable in order to understand the real thin film behavior.

IV. CONCLUSION

In summary, calculations on an idealized model indicate that the as-grown state of the $PbTiO_3$ films will have a preference for one of the two opposite polarization directions, depending on the contact potential between the ferroelectric thin film and the metal bottom electrode. Very thin films show voltage offsets and retention behavior compatible with a layer of positive charge near the top electrode.

ACKNOWLEDGMENTS

The authors acknowledges support from the Research Council of Norway under grant No. 162874/V00. Professor Asle Sudbø is acknowledged for scientific discussions.

[1] I. I. Ivanchik, Sov. Phys. Solid State **3**, 2705 (1962).
[2] G. M. Guro, I. I. Ivanchik, and N. F. Kovtonyuk, Sov. Phys. Solid State **11**, 1574 (1970).
[3] E. V. Chenskii, Sov. Phys. Solid State **12**, 446 (1970).
[4] C. Lichtensteiger, J.-M. Triscone, J. Junquera, and P. Ghosez, Phys. Rev. Lett. **94**, 047603 (2005).
[5] D. D. Fong, A. M. Kolpak, J. A. Eastman, S. K. Streiffer, P. H. Fuoss, G. B. Stephenson, C. Thompson, D. M. Kim, K. J. Choi, C. B. Eom, I. Grinberg, and A. M. Rappe, Phys. Rev. Lett. **96**, 127601 (2006).
[6] C. Thompson, C. M. Foster, J. A. Eastman, and G. B. Stephenson, Appl. Phys. Lett. **71**, 3516 (1997).
[7] S. K. Streiffer, J. A. Eastman, D. D. Fong, C. Thompson, A. Munkholm, M. V. Ramana Murty, O. Auciello, G. R. Bai, and G. B. Stephenson, Phys. Rev. Lett. **89**, 067601 (2002).
[8] R. Takahashi, J. K. Grepstad, T. Tybell, and Y. Matsumoto, Appl. Phys. Lett. **92**, 112901 (2008).

[9] S. H. Ahn, W. W. Jung, and S. K. Choi, Appl. Phys. Lett. **86**, 172901 (2005).

[10] C. Lichtensteiger, M. Dawber, N. Stucki, J.-M. Triscone, J. Hoffman, J.-B. Yau, C. H. Ahn, L. Despont, and P. Aebi, Appl. Phys. Lett. **90**, 052907 (2007).

[11] R. V. Wang, D. D. Fong, F. Jiang, M. J. Highland, P. H. Fuoss, C. Thompson, A. M. Kolpak, J. A. Eastman, S. K. Streiffer, A. M. Rappe, and G. B. Stephenson, Phys. Rev. Lett. **102**, 047601 (2009).

[12] Y. Watanabe, Phys. Rev. B **57**, 789 (1998).

[13] Ø. Dahl, J. K. Grepstad, and T. Tybell, J. Appl. Phys. **103**, 114112 (2008).

[14] A. G. Chynoweth, J. Appl. Phys. **27**, 78 (1956).

[15] V. A. Zhirnov, Sov. Phys. JETP **8**, 822 (1959).

[16] N. A. Pertsev, A. G. Zembilgotov, and A. K. Tagantsev, Phys. Rev. Lett. **80**, 1988 (1998).

[17] M. J. Haun, E. Furman, S. J. Jang, H. A. McKinstry, and L. E. Cross, J. Appl. Phys. **62**, 3331 (1987).

[18] The calculations were performed assuming a temperature-independent strain, $u_{11} = u_{22} = u = -0.015$, with rescaled values for the thermodynamic constants according to Ref. 16, $A = A_0 - u\frac{2Q12}{s_{11}+s_{12}}$ and $B = B_0 + \frac{Q_{12}^2}{s_{11}+s_{12}}$. The zero stress values were taken from Ref. 17: $A_0 = \alpha(T - T_0)$ with $\alpha = 7.530 \times 10^5$ m/F K and $T_0 = 478.8$ °C, $B_0 = -2.901 \times 10^8$ m^5/C^{2}F, $C = 1.5636 \times 10^9$ m^9/C^{4}F, $Q_{11} = 8.9 \times 10^{-2}$ m^4/C^2, $Q_{12} = -2.6 \times 10^{-2}$ m^4/C^2, and K was estimated at 9.221×10^{-11} m^3/F. $s_{11} = 7.2 \times 10^{-12}$ m^3/C^{2}F and $s_{12} = -2.1 \times 10^{-12}$ m^3/C^{2}F were taken from Ref. 27.

[19] N. W. Ashcroft and N. D. Mermin, *Solid State Physics* (Harcourt College Publishers, Forth Worth, 1976).

[20] The intrinsic equilibrium carrier density was estimated assuming a bandgap of 3.4 eV and effective electron and hole masses of $10m_e$.

[21] W. B. Joyce and R. W. Dixon, Appl. Phys. Lett. **31**, 354 (1977).

[22] For a parabolic band, the first four terms are $A_1 \approx 3.53553 \times 10^{-1}$, $A_2 \approx -4.95009 \times 10^{-3}$, $A_3 \approx 1.48386 \times 10^{-4}$, and $A_4 \approx -4.42563 \times 10^{-6}$. With these four terms, the expansion is accurate up to $\eta \approx 7$ (Ref. 21).

[23] The screening length was set at 0.11 nm and the relative dielectric constant at 8.45 (Ref. 34).

[24] S. M. Sze, *Physics of Semiconductor Devices*, 2nd ed. (John Wiley & Sons, New York, 1981) Chap. 5, p. 271.

[25] A. J. Hartmann, M. Neilson, R. N. Lamb, K. Watanabe, and J. F. Scott, Appl. Phys. A: Mater. Sci. Process. **70**, 239 (2000).

[26] J. Robertson and C. W. Chen, Appl. Phys. Lett. **74**, 1168 (1999).

[27] V. G. Gavrilyachenko and E. G. Fesenko, Sov. Phys. Crystallogr. **16**, 549 (1971).

[28] B. E. Deal, M. Sklar, A. S. Grove, and E. H. Snow, J. Electrochem. Soc. **114**, 266 (1967).

[29] R. R. Mehta, B. D. Silverman, and J. T. Jacobs, J. Appl. Phys. **44**, 3379 (1973).

[30] G. Arlt and H. Neumann, Ferroelectrics **87**, 109 (1988).

[31] G. E. Pike, W. L. Warren, D. Dimos, B. A. Tuttle, R. Ramesh, J. Lee, V. G. Keramidas, and J. T. Evans, Jr., Appl. Phys. Lett. **66**, 484 (1995).

[32] M. Grossmann, O. Lohse, D. Bolten, U. Boettger, T. Schneller, and R. Waser, J. Appl. Phys. **92**, 2680 (2002).

[33] A. K. Tagantsev, I. Stolichnov, N. Setter, and J. S. Cross, J. Appl. Phys. **96**, 6616 (2004).

[34] D. J. Kim, J. Y. Jo, Y. S. Kim, Y. J. Chang, J. S. Lee, J.-G. Yoon, T. K. Song, and T. W. Noh, Phys. Rev. Lett. **95**, 237602 (2005).

Chapter 5
Conclusions and outlook

We have studied the properties of thin $PbTiO_3$ films grown pseudomorphically on $SrTiO_3$ substrates. It was found that the properties are unchanged for film thickness down to 20 nm. For thinner films the interfaces and polarization screening mechanism starts influencing the properties.

The TEM study and XRD measurements showed that the $PbTiO_3$ films were of a good structural quality with a low density of extended defects. The major extrinsic impact on the ferroelectric properties was assumed to come from point defects in the film and from the interfaces and electrodes.

The effect of the point defects can be illustrated with the response of films grown at different temperatures. It was seen from XPS measurements that the Pb to Ti ratio at the surface decreased with increasing growth temperature. Concomitant with this, there was an increase in the leakage current and a larger negative offset voltage in the hysteresis loops. Although XPS is a surface technique, we expect the results to be indicative of the composition of the bulk of the sample as well. Hence the samples grown at optimal temperature are close to stoichiometric, with Pb and O vacancies as the dominating point defects. This is in agreement with the prevailing literature [160–166]. There are indications that the point defects have a stronger influence on the ferroelectric properties in very thin films. For films grown at optimal temperature, it was found that the offset voltage in the polarization hysteresis loops became negative in very thin films, similar to that observed in films grown at high temperatures. The stability of the negative polarization was lost after switching in very thin films.

The TEM study found a strain gradient, parallel with the polarization direction, in a layer near the Nb doped $SrTiO_3$ and pure $SrTiO_3$ substrate. In this layer, the c-axis of the unit cell was gradually reduced compared to the bulk of the film. The strain is not from the epitaxial growth, but can be related to a reduced polarization near the interface. A similar strain gradient has recently been observed for $Pb(Zr,Ti)O_3$ thin film grown on $SrRuO_3$ electrode [103, 104]. Based on the capacitance measurements for different film thickness, we found that the dielectric properties of this layer was not significantly changed from the bulk properties. This is in agreement with others who have found that the interface capacitance is dominated by the electrodes [88, 90, 167, 168]. The polarization can be reduced near the interface as a compromise between the depolarization energy from incompletely screened polarization and the strain and polarization gradient energy for an inhomogeneous polarization.

The XRD measurements showed a decreasing out-of-plane lattice constant with decreasing film thickness below 20 nm. This behaviour has also been observed previously in $PbTiO_3$ thin films [101]. The polarization profile, calculated from a

vacuum/ferroelectric/metal electrode structure, showed a decreasing bulk polarization for films in the same thickness region. The polarization as extracted from the measured lattice constant was in agreement with the model calculations.

The pyroelectric measurements showed that the polarization had the thick-film limit value down to a film thickness of 20 nm. For thinner films there was a reduced response. This is in agreement with the XRD results, and with other studies, which have found a reduction of the polarization for film thickness less than 15 nm [100, 103, 108, 114, 169]. For thick films, the initial polarization was found to be negative, consistent with the model calculations, showing the possibility of controlling the polarization by adjusting the contact potential of the interface between the ferroelectric and the electrodes. The decay of the net polarization after applying switching pulses was found to be faster in thinner films, consistent with an increased depolarization field with decreasing film thickness. The final state in very thin films was not zero net polarization, but a finite positive net polarization, which we interpret as an effect of the presence of interface dipoles and defects that influences the polarization.

Returning to the question of the factors that affect the switchability and stability of the polarization, it is clear that both the interfaces and defects are important. To clarify the relative importance of the interface itself, and interface defects, it would be of interest to investigate surface and interface defects in detail. This can be accomplished by measuring the depth profile and the nature of the defects, using e.g. XPS, Auger electron spectroscopy, and electron energy loss spectroscopy, which all give valuable information. However, these methods have either a low sensitivity, or are very local probes, so this is a challenging task. Utilizing different electrode materials, preferably metallic oxides to keep mechanical conditions unchanged, can verify the role of the interface. The relaxed state could be examined, with for instance scanning probe microscopy or x-ray diffraction methods, to clarify wether the relaxed state consists of randomly nucleated domains or regular stripe domains as found in some thin films [117, 170]. In addition, the temperature dependence of the polarization relaxation could shed light on the relaxation mechanism. Models of the three-dimensional strain at the interface, with particular attention to the effect of step edges on the strain, as well as the interaction between depolarization field, strain field, and point defects, would be of particular interest.

Bibliography

[1] F. Jona and G. Shirane, *Ferroelectric Crystals*. Oxford: Pergamon Press, 1962.

[2] S. B. Lang, "Pyroelectricity: A 2300-year history," *Ferroelectrics*, vol. 7, p. 231, 1974.

[3] J. Valasek, "Piezoelectric and allied phenomena in Rochelle salt," *Proceedings of The American Physical Society*, vol. XV, p. 537, 1920.

[4] J. Valasek, "Piezo-electric and allied phenomena in Rochelle salt," *Proceedings of The American Physical Society*, vol. XVII, p. 475, 1921.

[5] M. E. Lines and A. M. Glass, *Principles and Applications of Ferroelectrics and Related Materials*. Oxford: Oxford University Press, 2001.

[6] A. von Hippel, R. G. Breckenridge, F. G. Chesley, and L. Tisza, "High dielectric constant ceramics," *Industrial and Engineering Chemistry*, vol. 38, p. 1097, 1946.

[7] B. Wul, "Barium titanate: a new ferro-electric," *Nature*, vol. 157, p. 808, 1946.

[8] S. v. Náray-Szabó, "Der Strukturtyp des Perowskits ($CaTiO_3$)," *Naturwissenschaften*, vol. 31, p. 202, 1943.

[9] A. von Hippel, "Ferroelectricity, domain structure, and phase transitions of barium titanate," *Rev. Mod. Phys.*, vol. 22, p. 221, 1950.

[10] J. C. Slater, "The Lorentz correction in barium titanate," *Phys. Rev.*, vol. 78, p. 748, 1950.

[11] W. Cochran, "Crystal stability and the theory of ferroelectricity," *Advances in Physics*, vol. 9, p. 387, 1960.

[12] D. Vanderbilt and R. D. King-Smith, "Electric polarization as a bulk quantity and its relation to surface charge," *Phys. Rev. B*, vol. 48, p. 4442, 1993.

[13] R. D. King-Smith and D. Vanderbilt, "Theory of polarization of crystalline solids," *Phys. Rev. B*, vol. 47, p. 1651, 1993.

[14] R. Resta, "Macroscopic polarization in crystalline dielectrics: the geometric phase approach," *Rev. Mod. Phys.*, vol. 66, p. 899, 1994.

[15] R. Resta, M. Posternak, and A. Baldereschi, "Towards a quantum theory of polarization in ferroelectrics: The case of $KNbO_3$," *Phys. Rev. Lett.*, vol. 70, p. 1010, 1993.

[16] R. M. Martin, "Comment on calculations of electric polarization in crystals," *Phys. Rev. B*, vol. 9, p. 1998, 1974.

[17] R. E. Cohen and H. Krakauer, "Lattice dynamics and origin of ferroelectricity in $BaTiO_3$: Linearized-augmented-plane-wave total-energy calculations," *Phys. Rev. B*, vol. 42, p. 6416, 1990.

[18] R. E. Cohen and H. Krakauer, "Electronic structure studies of the differences in ferroelectric behavior of $BaTiO_3$ and $PbTiO_3$," *Ferroelectrics*, vol. 136, p. 65, 1992.

[19] R. E. Cohen, "Orirgin of ferroeelctricity in perovskite oxides," *Nature*, vol. 358, p. 136, 1992.

[20] R. E. Cohen, "Surface effects in ferroelectrics: Periodic slab computations for $BaTiO_3$," *Ferroelectrics*, vol. 194, p. 323, 1997.

[21] J. Padilla and D. Vanderbilt, "Ab initio study of $BaTiO_3$ surfaces," *Phys. Rev. B*, vol. 56, p. 1625, 1997.

[22] B. Meyer, J. Padilla, and D. Vanderbilt, "Theory of $PbTiO_3$, $BaTiO_3$, and $SrTiO_3$ surfaces," *Faraday Discuss.*, vol. 114, p. 395, 1999.

[23] B. Meyer and D. Vanderbilt, "Ab initio study of $BaTiO_3$ and $PbTiO_3$ surfaces in external fields," *Phys. Rev. B*, vol. 63, p. 205426, 2001.

[24] V. Ravikumar, D. Wolf, and V. P. Dravid, "Ferroelectric-monolayer reconstruction of the $SrTiO_3$ (100) surface," *Phys. Rev. Lett.*, vol. 74, p. 960, 1995.

[25] C. Bungaro and K. M. Rabe, "Coexistence of antiferrodistortive and ferroelectric distortions at the $PbTiO_3$ (001) surface," *Phys. Rev. B*, vol. 71, p. 035420, 2005.

[26] E. Bousquet, M. Dawber, N. Stucki, C. Lichtensteiger, P. Hermet, S. Gariglio, J.-M. Triscone, and P. Ghosez, "Improper ferroelectricity in perovskite oxide artificial superlattices," *Nature*, vol. 452, p. 732, 2008.

[27] J. Junquera and P. Ghosez, "Critical thickness for ferroelectricity in perovskite ultrathin films," *Nature*, vol. 422, p. 506, 2003.

[28] G. Gerra, A. K. Tagantsev, N. Setter, and K. Parlinski, "Ionic polarizability of conductive metal oxides and critical thickness for ferroelectricity in $BaTiO_3$," *Phys. Rev. Lett.*, vol. 96, p. 107603, 2006.

[29] A. M. Kolpak, N. Sai, and A. M. Rappe, "Short-circuit boundary conditions in ferroelectric $PbTiO_3$ thin films," *Phys. Rev. B*, vol. 74, p. 054112, 2006.

[30] Y. Umeno, B. Meyer, C. Elsässer, and P. Gumbsch, "Ab initio study of the critical thickness for ferroelectricity in ultrathin $Pt/PbTiO_3/Pt$ films," *Phys. Rev. B*, vol. 74, p. 060101(R), 2006.

[31] N. Sai, A. M. Kolpak, and A. M. Rappe, "Ferroelectricity in ultrathin perovskite films," *Phys. Rev. B*, vol. 72, p. 020101(R), 2005.

[32] C.-G. Duan, R. F. Sabirianov, W.-N. Mei, S. S. Jaswal, and E. Y. Tsymbal, "Interface effect on ferroelectricity at the nanoscale," *Nano Lett.*, vol. 6, p. 483, 2006.

[33] G. Gerra, A. K. Tagantsev, and N. Setter, "Ferroelectricity in asymmetric metal-ferroelectric-metal heterostructures: A combined first-principles-phenomenological approach," *Phys. Rev. Lett.*, vol. 98, p. 207601, 2007.

[34] V. Ginsburg, "On the dielectric properties of ferroelectric (seignetteelectric) crystals and barium titanate," *Journal of Physics*, vol. X, p. 107, 1946.

[35] A. F. Devonshire, "Theory of barium titanate.-Part I," *Philos. Mag.*, vol. 40, p. 1040, 1949.

[36] A. F. Devonshire, "Theory of barium titanate.-Part II," *Philos. Mag.*, vol. 42, p. 1065, 1951.

[37] A. F. Devonshire, "Theory of ferroelectrics," *Advances in Physics*, vol. 3, p. 85, 1954.

[38] R. R. Mehta, B. D. Silverman, and J. T. Jacobs, "Depolarization fields in thin ferroelectric films," *J. Appl. Phys.*, vol. 44, p. 3379, 1973.

[39] N. A. Pertsev, A. G. Zembilgotov, and A. K. Tagantsev, "Effect of mechanical boundary conditions on phase diagrams of epitaxial ferroelectric thin films," *Phys. Rev. Lett.*, vol. 80, p. 1988, 1998.

[40] H. H. Wieder, "Ferroelectric properties of colemanite," *J. Appl. Phys.*, vol. 30, p. 1010, 1959.

[41] J. Lee, R. Ramesh, V. G. Keramidas, W. L. Warren, G. E. Pike, and J. T. Evans, Jr., "Imprint and oxygen deficiency in $(Pb,La)(Zr,Ti)O_3$ thin-film capacitors with La-Sr-Co-O electrodes," *Appl. Phys. Lett.*, vol. 66, p. 1337, 1995.

[42] H.-S. Lee, K.-H. Auh, M.-S. Jeon, W.-S. Um, I.-S. Lee, G.-P. Choi, and H.-G. Kim, "Imprint of oriented $Pb(Zr,Ti)O_3$ thin films with oxygen atmosphere in cooling process," *Jpn. J. Appl. Phys.*, vol. 37, p. 5630, 1998.

[43] W. Wu, Y. Wang, G. K. H. Pang, K. H. Wong, and C. L. Choy, "Effect of lattice-misfit strain on the process-induced imprint behavior in epitaxial $Pb(Zr_{0.52}Ti_{0.48})O_3$ thin films," *Appl. Phys. Lett.*, vol. 85, p. 1583, 2004.

[44] K. Carl and K. H. Härdtl, "Electrical after-effects in $Pb(Ti,Zr)O_3$ ceramics," *Ferroelectrics*, vol. 17, p. 473, 1978.

[45] P. V. Lambeck and G. H. Jonker, "Ferroelectric domain stabilization in $BaTiO_3$ by bulk ordering of defects," *Ferroelectrics*, vol. 22, p. 729, 1978.

[46] S. Takahashi, "Effects of impurity doping in lead zirconate-titanate ceramics," *Ferroelectrics*, vol. 41, p. 143, 1982.

[47] W. L. Warren, D. Dimos, G. E. Pike, B. A. Tuttle, M. V. Raymond, R. Ramesh, and J. T. Evans, Jr., "Voltage shifts and imprint in ferroelectric capacitors," *Appl. Phys. Lett.*, vol. 67, p. 866, 1995.

[48] W. L. Warren, B. A. Tuttle, D. Dimos, G. E. Pike, H. N. Al-Shareef, R. Ramesh, and J. T. Evans, Jr., "Imprint in ferroelectric capacitors," *Jpn. J. Appl. Phys.*, vol. 35, p. 1521, 1996.

[49] S.-H. Kim, D.-S. Lee, C. S. Hwang, D.-J. Kim, and A. I. Kingon, "Thermally induced voltage offsets in $Pb(Zr,Ti)O_3$ thin films," *Appl. Phys. Lett.*, vol. 77, p. 3036, 2000.

[50] M. Grossmann, O. Lohse, D. Bolten, U. Boettger, T. Schneller, and R. Waser, "The interface screening model as origin of imprint in $PbZr_xTi_{1-x}O_3$ thin films. Dopant, illumination, and bias dependence," *J. Appl. Phys.*, vol. 92, p. 2680, 2002.

[51] G. Arlt and H. Neumann, "Internal bias in ferroelectric ceramics: Origin and time dependence," *Ferroelectrics*, vol. 87, p. 109, 1988.

[52] D. Dimos, W. L. Warren, M. B. Sinclair, B. A. Tuttle, and R. W. Schwartz, "Photoinduced hysteresis changes and optical storage in $(Pb,La)(Zr,Ti)O_3$ thin films and ceramics," *J. Appl. Phys.*, vol. 76, p. 4305, 1994.

[53] G. E. Pike, W. L. Warren, D. Dimos, B. A. Tuttle, R. Ramesh, J. Lee, V. G. Keramidas, and J. T. Evans, Jr., "Voltage offsets in $(Pb,La)(Zr,Ti)O_3$ thin films," *Appl. Phys. Lett.*, vol. 66, p. 484, 1995.

[54] H. N. Al-Shareef, D. Dimos, W. L. Warren, and B. A. Tuttle, "Voltage offsets and imprint mechanism in $SrBi_2Ta_2O_9$ thin films," *J. Appl. Phys.*, vol. 80, p. 4573, 1996.

[55] A. L. Kholkin and N. Setter, "Photoinduced poling of lead titanate zirconate thin films," *Appl. Phys. Lett.*, vol. 71, p. 2854, 1997.

[56] W. Känzig, "Space charge layer near the surface of a ferroelectric," *Phys. Rev.*, vol. 98, p. 549, 1955.

[57] A. G. Chynoweth, "Surface space-charge layers in barium titanate," *Phys. Rev.*, vol. 102, p. 705, 1956.

[58] J. Bardeen, "Surface states and rectification at a metal semi-conductor contact," *Phys. Rev.*, vol. 71, p. 717, 1947.

[59] K. Lehovec, "Space-charge layer and distribution of lattice defects at the surface of ionic crystals," *J. Chem. Phys.*, vol. 21, p. 1123, 1953.

[60] J. G. Simmons, "Intrinsic fields in thin insulating films between dissimilar electrodes," *Phys. Rev. Lett.*, vol. 10, p. 10, 1963.

[61] J. Lee, L. Johnson, A. Safari, R. Ramesh, T. Sands, H. Gilchrist, and V. G. Keramidas, "Effects of crystalline quality and electrode material on fatigue in Pb(Zr,Ti)O_3 thin film capacitors," *Appl. Phys. Lett.*, vol. 63, p. 27, 1993.

[62] P. W. M. Blom, R. M. Wolf, J. F. M. Cillessen, and M. P. C. M. Krijn, "Ferroelectric Schottky diode," *Phys. Rev. Lett.*, vol. 73, p. 2107, 1994.

[63] J. Lee, C. H. Choi, B. H. Park, T. W. Noh, and J. K. Lee, "Built-in voltages and asymmetric polarization switching in Pb(Zr,Ti)O_3 thin film capacitors," *Appl. Phys. Lett.*, vol. 72, p. 3380, 1998.

[64] P. Wurfel, I. P. Batra, and J. T. Jacobs, "Polarization instability in thin ferroelectric films," *Phys. Rev. Lett.*, vol. 30, p. 1218, 1973.

[65] W. W. Jung, H. C. Lee, W. S. Ahn, S. H. Ahn, and S. K. Choi, "Switchable single *c*-domain formation in a heteroepitaxial $PbTiO_3$ thin film on a (001) Nb-$SrTiO_3$ substrate fabricated by means of hydrothermal epitaxy," *Appl. Phys. Lett.*, vol. 86, p. 252901, 2005.

[66] J. M. Benedetto, R. A. Moore, and F. B. McLean, "Effects of operation conditions on the fast-decay component of the retained polarization in lead zirconate titanate thin films," *J. Appl. Phys.*, vol. 75, p. 460, 1994.

[67] I. G. Jenkins, T. K. Song, S. Madhukar, A. S. Prakash, S. Aggarwal, and R. Ramesh, "Dynamics of polarization loss in (Pb, La)(Zr, Ti)O_3 thin film capacitors," *Appl. Phys. Lett.*, vol. 72, p. 3300, 1998.

[68] J. W. Hong, W. Jo, D. C. Kim, S. M. Cho, H. J. Nam, H. M. Lee, and J. U. Bu, "Nanoscale investigation of domain retention in preferentially oriented $PbZr_{0.53}Ti_{0.47}O_3$ thin films on Pt and on $LaNiO_3$," *Appl. Phys. Lett.*, vol. 75, p. 3183, 1999.

[69] B. S. Kang, J.-G. Yoon, T. K. Song, S. Seo, Y. W. So, and T. W. Noh, "Retention characteristics of $Bi_{3.25}La_{0.75}Ti_3O_{12}$ thin films," *Jpn. J. Appl. Phys.*, vol. 41, p. 5281, 2002.

[70] B. H. Hoerman, B. M. Nichols, and B. W. Wessels, "Dynamic response of the dielectric and electro-optic properties of epitaxial ferroelectric thin films," *Phys. Rev. B*, vol. 65, p. 224110, 2002.

[71] D. J. Kim, J. Y. Jo, Y. S. Kim, Y. J. Chang, J. S. Lee, J.-G. Yoon, T. K. Song, and T. W. Noh, "Polarization relaxation induced by a depolarization field in ultrathin ferroelectric $BaTiO_3$ capacitors," *Phys. Rev. Lett.*, vol. 95, p. 237602, 2005.

[72] B. S. Kang, D. J. Kim, J. Y. Jo, T. W. Noh, J.-G. Yoon, T. K. Song, Y. K. Lee, J. K. Lee, S. Shin, and Y. S. Park, "Polarization retention in $Pb(Zr_{0.4}Ti_{0.6})O_3$ capacitors with IrO_2 top electrode," *Appl. Phys. Lett.*, vol. 84, p. 3127, 2004.

[73] A. Q. Jiang, Y. Y. Lin, and T. A. Tang, "Evaluation of interfacial-layer capacitance from fast polarization retention in ferroelectric thin films," *J. Appl. Phys.*, vol. 101, p. 056103, 2007.

[74] C.-C. Lee and J.-M. Wu, "Thickness-dependent retention behaviors and ferroelectric properties of $BiFeO_3$ thin films on $BaPbO_3$ electrodes," *Appl. Phys. Lett.*, vol. 91, p. 102906, 2007.

[75] Y. Shimada, K. Nakao, A. Inoue, M. Azuma, Y. Uemoto, E. Fujii, and T. Otsuki, "Temperature effects on charge retention characteristics of integrated $SrBi_2(Ta,Nb)_2O_9$ capacitors," *Appl. Phys. Lett.*, vol. 71, p. 2538, 1997.

[76] Y. Shimada, M. Azuma, K. Nakao, S. Chaya, N. Moriwaki, and T. Otsuki, "Retention characteristics of a ferroelectric memory based on $SrBi_2(Ta,Nb)_2O_9$," *Jpn. J. Appl. Phys.*, vol. 36, p. 5912, 1997.

[77] B. S. Kang, J.-G. Yoon, T. W. Noh, T. K. Song, S. Seo, Y. K. Lee, and J. K. Lee, "Polarization dynamics and retention loss in fatigued $PbZr_{0.4}Ti_{0.6}O_3$ ferroelectric capacitors," *Appl. Phys. Lett.*, vol. 82, p. 248, 2003.

[78] A. Gruverman, H. Tokumoto, A. S. Prakash, S. Aggarwal, B. Yang, M. Wuttig, R. Ramesh, O. Auciello, and T. Venkatesan, "Nanoscale imaging of domain dynamics and retention in ferroelectric thin films," *Appl. Phys. Lett.*, vol. 71, p. 3492, 1997.

[79] J. Y. Jo, D. J. Kim, Y. S. Kim, S.-B. Choe, T. K. Song, J.-G. Yoon, and T. W. Noh, "Polarization switching dynamics goverened by the thermodynamic nucleation process in ultrathin ferroelectric films," *Phys. Rev. Lett.*, vol. 97, p. 247602, 2006.

[80] A. L. Kholkin, E. L. Colla, A. K. Tagantsev, D. V. Taylor, and N. Setter, "Fatigue of piezoelectric properties in Pb(Zr,Ti)O_3 films," *Appl. Phys. Lett.*, vol. 68, p. 2577, 1996.

[81] L. M. Blinov, V. M. Fridkin, S. P. Palto, A. V. Sorokin, and S. G. Yudin, "Thickness dependence of switching for ferroelectric Langmuir films," *Thin Solid Films*, vol. 284–285, p. 474, 1996.

[82] A. V. Bune, V. M. Fridkin, S. Ducharme, L. M. Blinov, S. P. Palto, A. V. Sorokin, S. G. Yudin, and A. Zlatkin, "Two-dimensional ferroelectric films," *Nature*, vol. 391, p. 874, 1998.

[83] S. Ducharme, V. M. Fridkin, A. V. Bune, S. P. Palto, L. M. Blinov, N. N. Petukhova, and S. G. Yudin, "Intrinsic ferroelectric coercive field," *Phys. Rev. Lett.*, vol. 84, p. 175, 2000.

[84] C. Noguera, "Polar oxide surfaces," *J. Phys.: Condens. Matter*, vol. 12, p. R367, 2000.

[85] O. K. Rice, "Application of the Fermi statistics to the distribution of electrons under fields in metals and the theory of electrocapillarity," *Phys. Rev.*, vol. 31, p. 1051, 1928.

[86] H. Y. Ku and F. G. Ullman, "Capacitance of thin dielectric structures," *J. Appl. Phys.*, vol. 35, p. 265, 1964.

[87] P. K. Larsen, G. J. M. Dormans, D. J. Taylor, and P. J. van Veldhoven, "Ferroelectric properties and fatigue of $PbZr_{0.51}Ti_{0.49}O_3$ thin films of varying thickness: Blocking layer model," *J. Appl. Phys.*, vol. 76, p. 2405, 1994.

[88] C. Basceri, S. K. Streiffer, A. I. Kingon, and R. Waser, "The dielectric response as a function of temperature and film thickness of fiber-textured (Ba,Sr)TiO_3 thin films grown by chemical vapor deposition," *J. Appl. Phys.*, vol. 82, p. 2497, 1997.

[89] M. Grossmann, O. Lohse, D. Bolten, U. Boettger, T. Schneller, and R. Waser, "Interface-related decrease of the permittivity in $PbZr_xTi_{1-x}O_3$ thin films," *Appl. Phys. Lett.*, vol. 80, p. 1427, 2002.

[90] W. Y. Park and C. S. Hwang, "Film-thickness-dependent Curie-Weiss behaviour of (Ba,Sr)TiO_3 thin-film capacitors having Pt electrodes," *Appl. Phys. Lett.*, vol. 85, p. 5313, 2004.

[91] Y. Yano, K. Iijima, Y. Daitoh, T. Terashima, Y. Bando, Y. Watanabe, H. Kasatani, and H. Terauchi, "Epitaxial growth and dielectric properties of $BaTiO_3$ films on Pt electrodes by reactive evaporation," *J. Appl. Phys.*, vol. 76, p. 7833, 1994.

[92] L. Pintilie, I. Vrejoiu, D. Hesse, G. LeRhun, and M. Alexe, "Ferroelectric polarization-leakage current relation in high quality epitaxial Pb(Zr,Ti)O_3 films," *Phys. Rev. B*, vol. 75, p. 104103, 2007.

[93] E. G. Fesenko, V. S. Filip'ev, and M. F. Kupriyanov, "Homogeneous parameters characterizing the deformation of a perovskite lattice," *Sov. Phys. Solid State*, p. 366, 1969.

[94] H. Morioka, S. Yokoyama, T. Oikawa, H. Funakubo, and K. Saito, "Spontaneous polarization change with Zr/(Zr+Ti) ratios in perfectly polar-axis-orientated epitaxial tetragonal Pb(Zr,Ti)O_3 films," *Appl. Phys. Lett.*, vol. 85, p. 3516, 2004.

[95] S. Chattopadhyay, P. Ayyub, V. R. Palkar, and M. Multani, "Size-induced diffuse phase transition in the nanocrystalline ferroelectric $PbTiO_3$," *Phys. Rev. B*, vol. 52, p. 13177, 1995.

[96] K. Ishikawa, T. Nomura, N. Okada, and K. Takada, "Size effect on the phase transition in $PbTiO_3$ fine particles," *Jpn. J. Appl. Phys.*, vol. 35, p. 5196, 1996.

[97] B. Jiang, J. L. Peng, L. A. Bursill, and W. L. Zhong, "Size effects on ferroelectricity of ultrafine particles of $PbTiO_3$," *J. Appl. Phys.*, vol. 87, p. 3462, 2000.

[98] E. K. Akdogan, C. J. Rawn, W. D. Porter, E. A. Payzant, and A. Safari, "Size effects in $PbTiO_3$ nanocrystals: Effect of particle size on spontaneous polarization and strains," *J. Appl. Phys.*, vol. 97, p. 084305, 2005.

[99] K. Ishikawa, K. Yoshikawa, and N. Okada, "Size effect on the ferroelectric phase transition in $PbTiO_3$ ultrafine particles," *Phys. Rev. B*, vol. 37, p. 5852, 1988.

[100] Y. S. Kim, D. H. Kim, J. D. Kim, Y. J. Chang, T. W. Noh, J. H. Kong, K. Char, Y. D. Park, S. D. Bu, J.-G. Yoon, and J.-S. Chung, "Critical thickness of ulttrathin ferroelectric $BaTiO_3$ films," *Appl. Phys. Lett.*, vol. 86, p. 102907, 2005.

[101] C. Lichtensteiger, J.-M. Triscone, J. Junquera, and P. Ghosez, "Ferroelectricity and tetragonality in ultrathin $PbTiO_3$ films," *Phys. Rev. Lett.*, vol. 94, p. 047603, 2005.

[102] D. D. Fong, A. M. Kolpak, J. A. Eastman, S. K. Streiffer, P. H. Fuoss, G. B. Stephenson, C. Thompson, D. M. Kim, K. J. Choi, C. B. Eom, I. Grinberg, and A. M. Rappe, "Stabilization of monodomain polarization in ultrathin $PbTiO_3$ films," *Phys. Rev. Lett.*, vol. 96, p. 127601, 2006.

[103] V. Nagarajan, J. Junquera, J. Q. He, C. L. Jia, R. Waser, K. Lee, Y. K. Kim, S. Baik, T. Zhao, R. Ramesh, P. Ghosez, and K. M. Rabe, "Scaling of structure and electrical properies in ultrathin epitaxial ferroelectric heterostructures," *J. Appl. Phys.*, vol. 100, p. 051609, 2006.

[104] C.-L. Jia, V. Nagarajan, J.-Q. He, L. Houben, T. Zhao, R. Ramesh, K. Urban, and R. Waser, "Unit-cell scale mapping of ferroelectricity and tetragonality in epitaxial ultrathin ferroelectric films," *Nat. Mater.*, vol. 6, p. 64, 2007.

[105] K. J. Choi, M. Biegalski, Y. L. Li, A. Sharan, J. Schubert, R. Uecker, P. Reiche, Y. B. Chen, X. Q. Pan, V. Gopalan, L.-Q. Chen, D. G. Schlom, and C. B. Eom, "Enhancement of ferroelectricity in strained $BaTiO_3$ thin films," *Science*, vol. 306, p. 1005, 2004.

[106] G. Catalan, A. Janssens, G. Rispens, S. Csiszar, O. Seeck, G. Rijnders, D. H. A. Blank, and B. Noheda, "Polar domains in lead titanate films under tensile strain," *Phys. Rev. Lett.*, vol. 96, p. 127602, 2006.

[107] V. Nagarajan, I. G. Jenkins, S. P. Alpay, H. Li, S. Aggarwal, L. Salamanca-Riba, A. L. Roytburd, and R. Ramesh, "Thickness dependence of structural and electrical properties in epitaxial lead zirconate titanate films," *J. Appl. Phys.*, vol. 86, p. 595, 1999.

[108] N. Yanase, K. Abe, N. Fukushima, and T. Kawakubo, "Thickness dependence of ferroelectricity in heteroepitaxial $BaTiO_3$ thin film capacitors," *Jpn. J. Appl. Phys.*, vol. 38, p. 5305, 1999.

[109] H. N. Lee, S. M. Nakhmanson, M. F. Chisholm, H. M. Christen, K. M. Rabe, and D. Vanderbilt, "Suppressed dependence of polarization on epitaxial strain in highly polar ferroelectrics," *Phys. Rev. Lett.*, vol. 98, p. 217602, 2007.

[110] A. Petraru, H. Kohlstedt, U. Poppe, R. Waser, A. Solbach, U. Klemradt, J. Schubert, W. Zander, and N. A. Pertsev, "Wedgelike ultrathin epitaxial $BaTiO_3$ films for studies of scaling effects in ferroelectrics," *Appl. Phys. Lett.*, vol. 93, p. 072902, 2008.

[111] H. Fujisawa, S. Nakashima, K. Kaibara, M. Shimizu, and H. Niu, "Size effects of epitaxial and polycrystalline Pb(Zr,Ti)O_3 thin films grown by metalorganic chemical vapor depostion," *Jpn. J. Appl. Phys.*, vol. 38, p. 5392, 1999.

[112] H. Nonomura, H. Fujisawa, M. Shimizu, and H. Niu, "Epitaxial growth and ferroelectric properties of the 20-nm-thick Pb(Zr,Ti)O_3 film on $SrTiO_3$ (100) with an atomically flat surface by metalorganic chemical vapor deposition," *Jpn. J. Appl. Phys.*, vol. 41, p. 6682, 2002.

[113] J. R. Contreras, H. Kohlstedt, U. Poppe, R. Waser, and C. Buchal, "Surface treatment effects on the thickness dependence of the remanent polarization of $PbZr_{0.52}Ti_{0.48}O_3$ capacitors," *Appl. Phys. Lett.*, vol. 83, p. 126, 2003.

[114] V. Nagarajan, S. Prasertchoung, T. Zhao, H. Zheng, J. Ouyang, R. Ramesh, W. Tian, X. Q. Pan, D. M. Kim, C. B. Eom, H. Kohlstedt, and R. Waser, "Size effects in ultrathin epitaxial ferroelectric heterostructures," *Appl. Phys. Lett.*, vol. 84, p. 5225, 2004.

[115] T. Tybell, C. H. Ahn, and J.-M. Triscone, "Ferroelectricity in thin perovskite films," *Appl. Phys. Lett.*, vol. 75, p. 856, 1999.

[116] H. Béa, S. Fusil, K. Bouzehouane, M. Bibes, M. Sirena, G. Herranz, E. Jacquet, J.-P. Contour, and A. Barthélémy, "Ferroelectricity down to at least 2 nm in multiferroic $BiFeO_3$ epitaxial thin films," *Jpn. J. Appl. Phys.*, vol. 45, p. L187, 2006.

[117] S. K. Streiffer, J. A. Eastman, D. D. Fong, C. Thompson, A. Munkholm, M. V. Ramana Murty, O. Auciello, G. R. Bai, and G. B. Stephenson, "Observation of nanoscale 180° stripe domains in ferroelectric $PbTiO_3$ thin films," *Phys. Rev. Lett.*, vol. 89, p. 067601, 2002.

[118] A. G. Chynoweth, "Dynamic method for measuring the pyroelectric effect with special reference to barium titanate," *J. Appl. Phys.*, vol. 27, p. 78, 1956.

[119] E. Fermi, *Thermodynamics*. New York: Dover Publications, 1956.

[120] J. A. Stratton, *Electromagnetic Theory*. New York and London: McGraw-Hill Book Company, 1941.

[121] J. F. Nye, *Physical Properties of Crystals*. Oxford: Oxford University Press, 1985.

[122] L. D. Landau and E. M. Lifshitz, *Theory of Elasticity*. Oxford: Pergamon Press, second english ed., 1970.

[123] L. D. Landau and E. M. Lifshitz, *Statistical Physics*. London: Pergamon Press, 1963.

[124] V. Volterra, *Theory of Functionals and of Integral and Integro-Differential Equations*. New York: Dover Publications, Inc., Dover ed., 1959.

[125] E. L. Hill, "Hamilton's principle and the conservation theorems of mathematical physics," *Rev. Mod. Phys.*, vol. 23, p. 253, 1951.

[126] L. D. Landau and E. M. Lifshitz, *Electrodynamics of Continuous Media*. Oxford: Pergamon Press, 1960.

[127] J. Grindlay, *An Introduction to the Phenomenological Theory of Ferroelectricity*. Oxford: Pergamon Press, 1970.

[128] S. Roberts, "Dielectric and piezoelectric properties of barium titanate," *Phys. Rev.*, vol. 71, p. 890, 1947.

[129] M. J. Haun, E. Furman, S. J. Jang, H. A. McKinstry, and L. E. Cross, "Thermodynamic theory of $PbTiO_3$," *J. Appl. Phys.*, vol. 62, p. 3331, 1987.

[130] W. Cao and L. E. Cross, "Theory of tetragonal twin structures in ferroelectric perovskites with a first-order transition," *Phys. Rev. B*, vol. 44, p. 5, 1991.

[131] J. S. Speck and W. Pompe, "Domain configurations due to multiple misfit relaxation mechanisms in epitaxial ferroelectric thin films. I. Theory," *J. Appl. Phys.*, vol. 76, p. 466, 1994.

[132] S. T. Liu and J. D. Zook, "Evaluation of Curie constants of ferroelectric crystals from pyroelectric response," *Ferroelectrics*, vol. 7, p. 171, 1974.

[133] M. E. Caspari and W. J. Merz, "The electromechanical behavior of $BaTiO_3$ single-domain crystals," *Phys. Rev.*, vol. 80, p. 1082, 1950.

[134] V. G. Gavrilyachenko, R. I. Spinko, M. A. Martynenko, and E. G. Fesenko, "Spontaneous polarization and coercive field of lead titanate," *Sov. Phys. Solid State*, vol. 12, p. 1203, 1970.

[135] G. Zorn, W. Wersing, and H. Göbel, "Electrostrictive tensor components of PZT-ceramics measured by x-ray diffraction," *Jpn. J. Appl. Phys.*, vol. 24, p. 721, 1985.

[136] N. W. Aschcroft and N. D. Mermin, *Solid State Physics*. Fort Worth: Harcourt College Publishers, 1976.

[137] P. Sigmund, "Theory of sputtering. I. Sputtering yield of amorphous and polycrystalline targets," *Phys. Rev.*, vol. 184, p. 383, 1969.

[138] G. S. Anderson, W. N. Mayer, and G. K. Wehner, "Sputtering of dielectrics by high-frequency fields," *J. Appl. Phys.*, vol. 33, p. 2991, 1962.

[139] R. L. Sandstrom, W. J. Gallagher, T. R. Dinger, R. H. Koch, R. B. Laibowitz, A. W. Kleinsasser, R. J. Gambino, B. Bumble, and M. F. Chisholm, "Reliable single-target sputtering process for high-temperature superconducting films and devices," *Appl. Phys. Lett.*, vol. 53, p. 444, 1988.

[140] C. B. Eom, J. Z. Sun, K. Yamamoto, A. F. Marshall, K. E. Luther, T. H. Geballe, and S. S. Laderman, "In situ grown $YBa_2Cu_3O_{7-d}$ thin films from single-target magnetron sputtering," *Appl. Phys. Lett.*, vol. 55, p. 595, 1989.

[141] J. L. Vossen, "Control of film properties by rf-sputtering techniques," *J. Vac. Sci. Technol.*, vol. 8, p. S12, 1971.

[142] J. F. M. Cillessen, M. W. J. Prins, and R. M. Wolf, "Thickness dependence of the switching voltage in all-oxide ferroelectric thin-film capacitors prepared by pulsed laser deposition," *J. Appl. Phys.*, vol. 81, p. 2777, 1997.

[143] M. Kawasaki, K. Takahashi, T. Maeda, R. Tsuchiya, M. Shinohara, O. Ishiyama, T. Yonezawa, M. Yoshimoto, and H. Koinuma, "Atomic control of the $SrTiO_3$ crystal surface," *Science*, vol. 266, p. 1540, 1994.

[144] G. Koster, B. L. Kropman, G. J. H. M. Rijnders, D. H. A. Blank, and H. Rogalla, "Quasi-ideal strontium titanate crystal surfaces through formation of strontium hydroxide," *Appl. Phys. Lett.*, vol. 73, p. 2920, 1998.

[145] A. Guinier, *X-Ray Diffraction In Crystals, Imperfect Crystals, and Amorphous Bodies*. New York: Dover Publications, Inc., 1994.

[146] S. Hüfner, *Photoelectron Spectroscopy Principles and Applications*. Heidelberg: Springer-Verlag, third ed., 2003.

[147] A. Savitzky and M. J. E. Golay, "Smoothing and differentiation of data by simplified least squares procedures," *Anal. Chem.*, vol. 36, p. 1627, 1964.

[148] D. A. Shirley, "High-resolution x-ray photoemission spectrum of the valence bands of gold," *Phys. Rev. B*, vol. 5, p. 4709, 1972.

[149] C. B. Sawyer and C. H. Tower, "Rochelle salt as a dielectric," *Phys. Rev.*, vol. 35, p. 269, 1930.

[150] H. S. Carslaw and J. C. Jaeger, *Conduction of Heat in Solids*. Oxford: Clarendon Press, second ed., 1992.

[151] W. Martienssen, "The elements," in *Springer Handbook of Condensed Matter and Materials Data* (W. Martienssen and H. Warlimont, eds.), Berlin Heidelberg: Springer, 2005.

[152] T. Mitsui, S. Nomura, M. Adachi, J. Harada, T. Ikeda, E. Nakamura, E. Sawaguchi, T. Shigenari, Y. Shiozaki, I. Tatsuzaki, K. Toyoda, T. Yamada, K. Gesi, Y. Makita, M. Marutake, T. Shiosaki, and K. Wakino, "Ferroelectrics and related substances," in *Landolt-Börnstein Numerical Data and Functional Relationships in Science and Technology* (K.-H. Hellwege and A. M. Hellwege, eds.), vol. 16, Berlin Heidelberg: Springer-Verlag, 1981.

[153] S. Yamanaka, T. Maekawa, H. Muta, T. Matsuda, S.-i. Kobayashi, and K. Kurosaki, "Thermophysical properties of $SrHfO_3$ and $SrRuO_3$," *J. Solid State Chem.*, vol. 177, p. 3484, 2004.

[154] P. B. Johnson and R. W. Christy, "Optical constants of the noble metals," *Phys. Rev. B*, vol. 6, p. 4370, 1972.

[155] G. A. Rossetti, Jr., L. E. Cross, and K. Kushida, "Stress induced shift of the curie point in epitaxial $PbTiO_3$ thin films," *Appl. Phys. Lett.*, vol. 59, p. 2524, 1991.

[156] A. Amin, M. J. Haun, B. Badger, H. McKinstry, and L. E. Cross, "A phenomenological Gibbs function for the single cell region of the $PbZrO_3$:$PbTiO_3$ solid solution system," *Ferroelectrics*, vol. 65, p. 107, 1985.

[157] S. Ikegami, I. Ueda, and T. Nagata, "Electromechanical properties of $PbTiO_3$ ceramics containing La and Mn," *The Journal of the Acoustical Society of America*, vol. 50, p. 1060, 1971.

[158] V. G. Gavrilyachenko and E. G. Fesenko, "Piezoelectric effect in lead titanate single crystals," *Sov. Phys. Crystallogr.*, vol. 16, p. 549, 1971.

[159] D. de Ligny and P. Richet, "High-temperature heat capacity and thermal expansion of $SrTiO_3$ and $SrZrO_3$ perovskites," *Phys. Rev. B*, vol. 53, p. 3013, 1996.

[160] R. Gerson and H. Jaffe, "Electrical conductivity in lead titanate zirconate ceramics," *J. Phys. Chem. Solids*, vol. 24, p. 979, 1963.

[161] S.-i. Shirasaki, "Defect lead titanates with diverse Curie temperatures," *Solid State Commun.*, vol. 9, p. 1217, 1971.

[162] R. L. Holman and R. M. Fulrath, "Intrinsic nonstoichiometry in the lead zirconate-lead titanate system determined by Knudsen effusion," *J. Appl. Phys.*, vol. 44, p. 5227, 1973.

[163] S. Shirasaki, K. Takahashi, H. Yamamura, K. Kakegawa, and J. Mori, "Defect ferroelectrics of type $Pb_{1-x}TiO_{3-x}$," *J. Solid State Chem.*, vol. 12, p. 84, 1975.

[164] D. M. Smyth, "Charge motion in ferroelectric thin films," *Ferroelectrics*, vol. 116, p. 117, 1991.

[165] M. V. Raymond and D. M. Smyth, "Defects and charge transport in perovskite ferroelectrics," *J. Phys. Chem. Solids*, vol. 57, p. 1507, 1996.

[166] S. Aggarwal and R. Ramesh, "Point defect chemistry of metal oxide heterostructures," *Annu. Rev. Mater. Sci.*, vol. 28, p. 463, 1998.

[167] S. K. Streiffer, C. Basceri, C. B. Parker, S. E. Lash, and A. I. Kingon, "Ferroelectricity in thin films: The dielectric response of fiber-textured $(Ba_xSr_{1-x})Ti_{1+y}O_{3+z}$ thin films grown by chemical vapor deposition," *J. Appl. Phys.*, vol. 86, p. 4565, 1999.

[168] Y. S. Kim, J. Y. Jo, D. J. Kim, Y. J. Chang, J. H. Lee, T. W. Noh, T. K. Song, J.-G. Yoon, J.-S. Chung, S. I. Baik, Y.-W. Kim, and C. U. Jung, "Ferroelectric properties of $SrRuO_3/BaTiO_3/SrRuO_3$ ultrathin film capacitors free from passive layers," *Appl. Phys. Lett.*, vol. 88, p. 072909, 2006.

[169] A. Petraru, N. A. Pertsev, H. Kohlstedt, U. Poppe, R. Waser, A. Solbach, and U. Klemradt, "Polarization and lattice strains in epitaxial $BaTiO_3$ films grown by high-pressure sputtering," *J. Appl. Phys.*, vol. 101, p. 114106, 2007.

[170] R. Takahashi, J. K. Grepstad, T. Tybell, and Y. Matsumoto, "Photochemical switching of ultrathin $PbTiO_3$ films," *Appl. Phys. Lett.*, vol. 92, p. 112901, 2008.